

AN ABSTRACT OF THE THESIS OF

Osvaldo Sánchez Zamora for the degree of Doctor of Philosophy
in Geophysics presented on May 2, 1988

Title: Crustal Structure and Thermal Gradients of the Northern
Gulf of California Determined Using Spectral Analysis of
Magnetic Anomalies.

Abstract approved:

 **Redacted for Privacy**

Geophysical surveys in the Gulf of California provided the data to construct contour maps of bathymetry, free-air anomalies and total field magnetic anomalies for the area north of 27° N. Major faults such as the Ballenas-Salsipuedes, Tiburón, Guaymas, and the South Cerro Prieto are clearly observable on these maps.

Spectral analysis, using 2-D Fast Fourier Transform methods, of the magnetic anomalies north of 29° N, allowed the identification of at least three distinct magnetic source horizons. The shallowest depth magnetic horizon, with an average depth to the top of 3.1 km below sea level, is interpreted as the top of the magnetic basement. The intermediate depth magnetic horizon, with an average depth to the top of 5.3 km below sea level, may represent either a lithological discontinuity in continental crust, or a transition zone characterized by the intrusion of

igneous rocks, faulting, and fracturing associated with rifting processes. Some lineaments observed in the contour map on this horizon are oriented about 15° counterclockwise from the expected orientation of faults. Other lineaments are almost perpendicular to those faults. The deepest magnetic horizon is not apparent at all locations.

Computed depths to the bottom of the magnetized crust average 11.5 km below sea level. The depth to the bottom of the magnetic crust is interpreted as the depth of the Curie-point isotherm. Assuming a Curie-point temperature of 580°C and a thermal conductivity of $2.2 \text{ W/m } ^{\circ}\text{C}$, the calculated heat flow averages 114 mW/m^2 .

Using a two-dimensional Maximum Entropy Method (2DMEM) to obtain the power spectrum of the magnetic anomalies increased the horizontal spatial resolution of the depth determinations by a factor of 4. This method when used to compute the depth to the top of the intermediate horizon, shows an improvement in the delineation of structures. However, the other magnetic horizons and the depth to the bottom of the magnetic crust were not clearly observable using this technique.

Crustal Structure and Thermal Gradients
of the Northern Gulf of California Determined Using
Spectral Analysis of Magnetic Anomalies

by

Osvaldo Sánchez Zamora

A THESIS
submitted to
Oregon State University

in partial fulfillment of
the requirements for the
degree of

Doctor of Philosophy

Completed on May 2, 1988
Commencement June 1988

APPROVED:

Redacted for Privacy

Associate Professor of Geophysics in charge of major

Redacted for Privacy

Dean of College of Oceanography

Redacted for Privacy

Dean of Graduate School

Date thesis is presented May 2, 1988

Typed by the author Osvaldo Sánchez Zamora

ACKNOWLEDGEMENTS

I would like to give special thanks, and recognition to Dr. Richard Couch, my major professor, for all that he has taught me. I have greatly enjoyed working with him. I appreciate his advice and criticism, patience and encouragement, and most of all his interest in and personal concern for students.

Dr. Gordon Ness, as with my master's thesis, had the hard task of reading my "incredibly well written" first draft. He also gave me the last push when I most needed it, for which I am very thankful. He is indeed such a good friend.

Dr. Paul Dauphin taught me, among other things, some of the politics inherent in the practice of science. He gave me moral support whenever I needed it.

I very much appreciate the detailed review provided by Gerry Connard, and the many discussions we have had concerning spectral analysis in particular and magnetics in general.

Admiral Gilberto López Lira, General Director of DGON, and Dr. Gustavo Calderón Riveroll, Director of IOM, deserve my gratitude for the personal and financial support they gave me and for stimulating me to pursue graduate degrees.

Steve Troseth and Ann Yeaple, helped me with all the drafting. Michael Kelsay, Bob O'Malley, Linda Dillon and Tim Holt, provided computer assistance and software. Jeb Bowers, our chief engineer, (Mr. S-42) and his team: Steve Azevedo, "Dutch" Waldvogel, and Pete Kalk, without them we would not have the data. Gloria Walker,

with her professionalism, helped me in every imaginable way.
Thanks to all of you.

My fellow students: Pierre Doguin, with new hints every day about the Macintosh; Juan García, for the long discussions about my thesis; Rainer Ludwig, Ana Macario, and Luis Braga, thank you.

The support of my lovely wife Carmen and our two wonderful children Daniel and Diana throughout this effort made it worthwhile and possible to endure. I love you.

This work was partially supported by NASA contract NAG 5-788 and by ONR contract N00014-84-C-0673.

TABLE OF CONTENTS

| | Page |
|--|------|
| INTRODUCTION | 1 |
| GENERAL GEOLOGY, PHYSIOGRAPHY, AND TECTONICS OF THE GULF OF CALIFORNIA AND ADJACENT AREAS | 4 |
| Baja California | 4 |
| The Salton Trough | 6 |
| The Sonora Desert and Sierra Madre Occidental | 7 |
| POTENTIAL FIELD ANOMALIES AND BATHYMETRY | 8 |
| Data Location | 8 |
| Navigation Data | 8 |
| Gravity Data | 9 |
| Magnetics Data | 10 |
| Bathymetry Data | 11 |
| Contour Maps | 11 |
| Bathymetry of the Northern Gulf | 11 |
| Free-Air Gravity Anomalies of the Northern Gulf | 15 |
| Total Field Magnetic Anomalies of the Northern Gulf | 20 |
| DEPTH TO MAGNETIC SOURCES | |
| THE FFT APPROACH | 26 |
| Depth to the Top of the Magnetic Sources. | 28 |
| Data Processing | 28 |
| Interpretation of Results | 35 |
| Depth to the Bottom of the Magnetic Source. | 42 |
| Curie-point Isotherm Depths | 46 |
| DEPTH TO MAGNETIC SOURCES | |
| THE MAXIMUM ENTROPY APPROACH | 54 |
| 1-D Maximum Entropy Spectral Estimation | 55 |
| Extension of the Theory to 2-D | 56 |
| Experimental Results Using 2-D Maximum Entropy | 58 |
| Detrend and Taper | 64 |
| Prediction Error Filter Size | 64 |
| Application of the 2D MEM to the Northern Gulf of California Magnetic Data | 65 |

| | Page |
|---|------|
| CONCLUSIONS | 72 |
| BIBLIOGRAPHY | 74 |
| APPENDICES | |
| A. Radially Averaged Spectral Plots Using 2DFFT | 81 |
| B. Radially Averaged Spectral Plots Using 2DMEM | 105 |

LIST OF FIGURES

| <u>Figure</u> | | <u>Page</u> |
|---------------|---|-------------|
| 1 | Generalized tectonic map of the Gulf of California and surroundings. After Ness et al. (1988). | 2 |
| 2 | Bathymetric map of the northern Gulf of California. | 13 |
| 3 | Bathymetric trackline map. | 14 |
| 4 | Free-air gravity anomaly map of the northern Gulf of California. | 18 |
| 5 | Gravity trackline map. | 19 |
| 6 | Total field magnetic anomaly map of the northern Gulf of California. | 24 |
| 7 | Magnetics trackline map. | 25 |
| 8 | Location of grids in the northern Gulf of California. | 30 |
| 9 | Relative location of 64 by 64 km grids. | 31 |
| 10 | Radially averaged power spectrum of grid N1, using the 2DFFT. | 34 |
| 11 | Contour map of the depth to the top of the shallow magnetic source in the northern Gulf of California. | 38 |
| 12 | Location of the seismic refraction lines of Phillips (1964), and the geophysical cross section of Doguin (1988) in the northern Gulf of California. | 40 |
| 13 | Contour map of the depth to the top of the intermediate magnetic source in the northern Gulf of California. | 41 |
| 14 | Contour map of the depth to the top of the deep magnetic source in the northern Gulf of California. | 43 |

| | | |
|-----|--|-----|
| 1 5 | Contour map of the depth to the Curie-point isotherm in the northern Gulf of California. | 4 8 |
| 1 6 | Computed and observed heat flow in the northern Gulf of California. | 5 1 |
| 1 7 | Radially averaged power spectrum of grid N1, using the 2DFFT. The grid was previously detrended and tapered. | 6 0 |
| 1 8 | Radially averaged power spectrum of grid N1, using the 2DMEM. The grid was previously detrended and tapered. | 6 1 |
| 1 9 | Radially averaged power spectrum of grid N1, using the 2DMEM. The grid was previously detrended but not tapered. | 6 2 |
| 2 0 | Location of centers of the 32 km by 32 km grids. | 6 6 |
| 2 1 | Names of the 32 km by 32 km grids. | 6 7 |
| 2 2 | Depth to the top of the magnetic source using 2DMEM. | 7 0 |

Appendices

Figure

| | | |
|-----|--|-----|
| A 1 | Radially averaged power spectrum of grid N1, using the 2DFFT. | 8 2 |
| A 2 | Radially averaged power spectrum of grid N2, using the 2DFFT. | 8 3 |
| A 3 | Radially averaged power spectrum of grid N3, using the 2DFFT. | 8 4 |
| A 4 | Radially averaged power spectrum of grid N4, using the 2DFFT. | 8 5 |
| A 5 | Radially averaged power spectrum of grid N5, using the 2DFFT. | 8 6 |

| | | |
|------|--|-----|
| A 6 | Radially averaged power spectrum of grid N6, using the 2DFFT. | 8 7 |
| A 7 | Radially averaged power spectrum of grid N7, using the 2DFFT. | 8 8 |
| A 8 | Radially averaged power spectrum of grid N8, using the 2DFFT. | 8 9 |
| A 9 | Radially averaged power spectrum of grid N9, using the 2DFFT. | 9 0 |
| A 10 | Radially averaged power spectrum of grid NE, using the 2DFFT. | 9 1 |
| A 11 | Radially averaged power spectrum of grid C1, using the 2DFFT. | 9 2 |
| A 12 | Radially averaged power spectrum of grid C2, using the 2DFFT. | 9 3 |
| A 13 | Radially averaged power spectrum of grid C3, using the 2DFFT. | 9 4 |
| A 14 | Radially averaged power spectrum of grid C4, using the 2DFFT. | 9 5 |
| A 15 | Radially averaged power spectrum of grid C5, using the 2DFFT. | 9 6 |
| A 16 | Radially averaged power spectrum of grid C6, using the 2DFFT. | 9 7 |
| A 17 | Radially averaged power spectrum of grid C7, using the 2DFFT. | 9 8 |
| A 18 | Radially averaged power spectrum of grid C8, using the 2DFFT. | 9 9 |
| A 19 | Radially averaged power spectrum of grid C9, using the 2DFFT. | 100 |

| | | |
|-----|--|-----|
| A20 | Radially averaged power spectrum of grid SC, using the 2DFFT. | 101 |
| A21 | Radially averaged power spectrum of grid SE, using the 2DFFT. | 102 |
| A22 | Plots of the radially averaged theoretical power spectrum. | 103 |
| A23 | Plot of the radially averaged power spectrum for a grid appended with zeroes. | 104 |
| B1 | Radially averaged power spectrum of grids N11, N12, N13 and N14 using 2DMEM. | 109 |
| B2 | Radially averaged power spectrum of grids N15, N16, N17 and N18 using 2DMEM. | 110 |
| B3 | Radially averaged power spectrum of grids N19, N22, N25 and N28 using 2DMEM. | 111 |
| B4 | Radially averaged power spectrum of grids N31, N32, N33 and N35 using 2DMEM. | 112 |
| B5 | Radially averaged power spectrum of grids N36, N37, N38 and N39 using 2DMEM. | 113 |
| B6 | Radially averaged power spectrum of grids N44, N45, N46 and N55 using 2DMEM. | 114 |
| B7 | Radially averaged power spectrum of grids N64, N65, N66 and N71 using 2DMEM. | 115 |
| B8 | Radially averaged power spectrum of grids N74, N76, N77 and N78 using 2DMEM. | 116 |
| B9 | Radially averaged power spectrum of grids N79, N85, N91 and N92 using 2DMEM. | 117 |
| B10 | Radially averaged power spectrum of grids N94, N95, N96 and N97 using 2DMEM. | 118 |

| | | |
|-----|--|-----|
| B11 | Radially averaged power spectrum of grids N98, NE2, NE5 and NE6 using 2DMEM. | 119 |
| B12 | Radially averaged power spectrum of grids C31, C32, C34 and C36 using 2DMEM. | 120 |
| B13 | Radially averaged power spectrum of grids C37, C44, C45 and C46 using 2DMEM. | 121 |
| B14 | Radially averaged power spectrum of grids C55, C65, C66 and C71 using 2DMEM. | 122 |
| B15 | Radially averaged power spectrum of grids C73, C82, C85 and C91 using 2DMEM. | 123 |
| B16 | Radially averaged power spectrum of grids C92, C94, C95 and C96 using 2DMEM. | 124 |
| B17 | Radially averaged power spectrum of grids C97, C98, C99 and SC2 using 2DMEM. | 125 |
| B18 | Radially averaged power spectrum of grids SC3, SC6, SE1 and SE2 using 2DMEM. | 126 |
| B19 | Radially averaged power spectrum of grids SE3, SE4, SE5 and SE6 using 2DMEM. | 127 |

LIST OF TABLES

| <u>Table</u> | | <u>Page</u> |
|--------------|---|-------------|
| 1 | Gravity base stations used during GOLFO-81 and GOLFO-84. | 1 0 |
| 2 | Depths to the top of the magnetic sources and heat flow using 2DFFT. | 3 7 |
| 3 | Depth to the bottom d, vs depth to the top h, for several frequencies. | 4 7 |
| 4 | Depths to the top of the magnetic source using 2DMEM. | 6 9 |

CRUSTAL STRUCTURE AND THERMAL GRADIENTS OF THE NORTHERN GULF OF CALIFORNIA DETERMINED USING SPECTRAL ANALYSIS OF MAGNETIC ANOMALIES

INTRODUCTION

The Gulf of California constitutes part of the North American-Pacific tectonic plate boundary and represents a transition between typical sea-floor spreading at the Rivera Rise (Ness et al., 1981) and strike-slip motion along the San Andreas fault system (Wilson, 1965) (Figure 1). The Gulf of California itself can be divided into at least two different tectonic regions: The southern Gulf of California which is characterized by a series of "en echelon" transform faults connected by short spreading centers (Vine, 1966; Moore and Buffington 1968)- an oceanic appearing regime, and the northern Gulf of California where the crust is thicker. To better understand the tectonics of the northern region it would be helpful to know more about the structure and composition of the crust as well as the thermal conditions in the northern Gulf of California.

In 1975, researchers from the Geophysics Group at Oregon State University, and from the Instituto Oceanográfico de Manzanillo (IOM), a research agency of the Mexican Dirección General de Oceanografía Naval (DGON), began a study program of the Pacific continental margin of México. This program included a comprehensive survey of the variations in the earth's gravity and

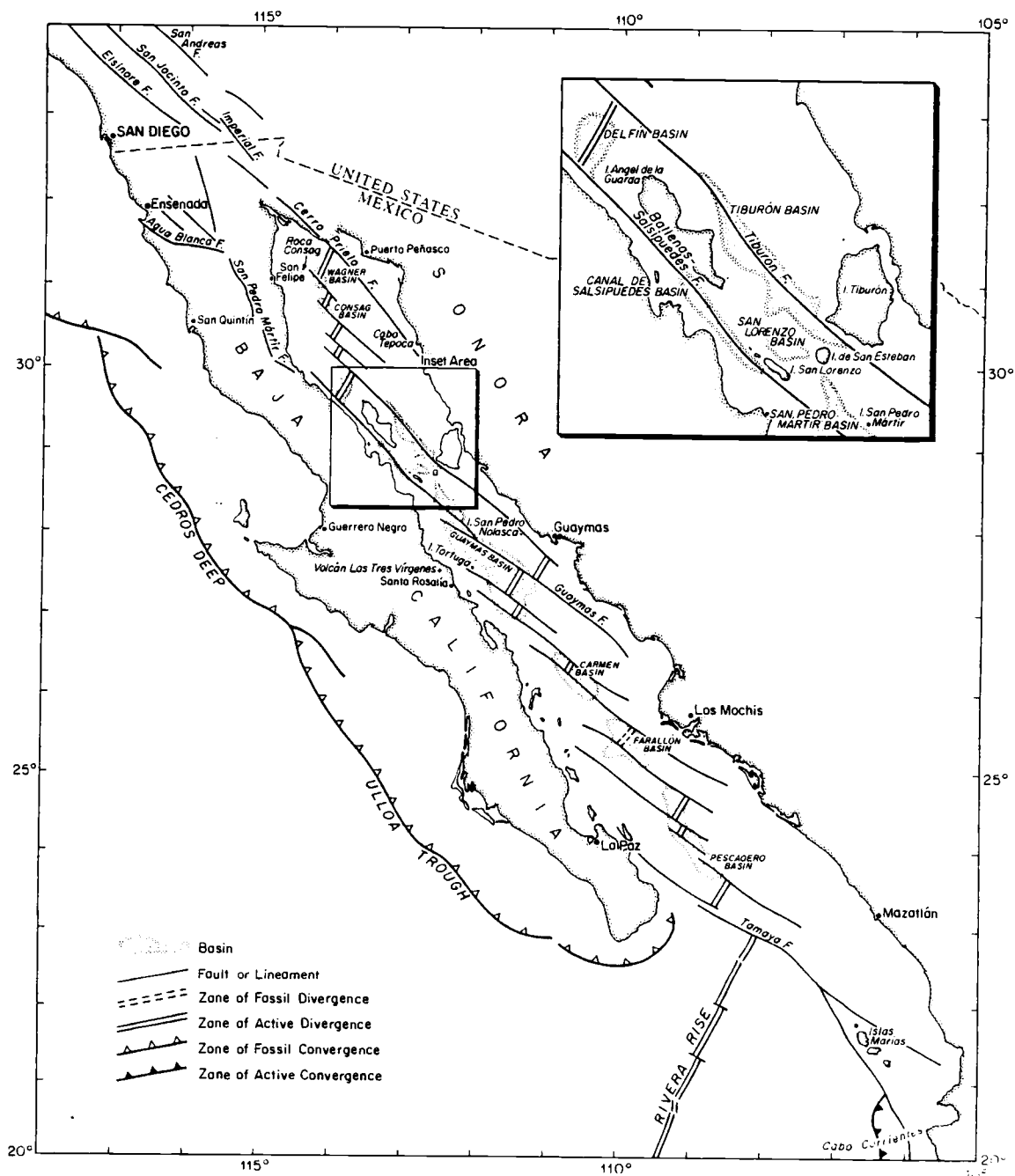


Figure 1. Generalized tectonic map of the Gulf of California and surroundings.
After Ness et al. (1988).

magnetic fields and water depths within the Pacific Exclusive Economic Zone of México.

In the northern Gulf of California, north of Guaymas, marine geophysical measurements made during 1981 and 1984 cruises provided data of sufficient spatial density to merit compiling new contour maps of free-air gravity anomalies, total field magnetic anomalies and bathymetry.

In this study I used the very precisely navigated data north of 29° N to investigate the crustal structure and to compute the depth of the Curie-point isotherm in the northern Gulf of California.

The analysis of the magnetic data includes the calculation of the power spectrum of the magnetic anomalies using the Fourier Transform in two dimensions to estimate the depth to the tops of the magnetic sources and the depth to the Curie-point isotherm. A second objective of this study was to improve the spatial resolution of the analysis by using the Maximum Entropy Method (MEM) in two dimensions.

GENERAL GEOLOGY, PHYSIOGRAPHY, AND TECTONICS OF THE GULF OF CALIFORNIA AND ADJACENT AREAS

The Gulf of California extends approximately 1500 km southeast from the mouth of the Colorado River to Cabo Corrientes. It reaches oceanic depths at its southernmost part and continental shelf depths in the northernmost part. The gulf is bounded by the peninsula of Baja California to the west, the Salton Trough to the north, and mainland Mexico to the east. Its average width is about 100 km.

The Gulf, north of 27° N, hereafter referred to as the northern Gulf of California, includes part of the central and all of the northern morphological regions outlined by Rusnak et al., (1964).

Baja California

The peninsula of Baja California can be roughly divided into three geologically different regions. The northern part is largely dominated by the Peninsular Ranges Batholith, the central and southern part by the Peninsular Volcanic Ranges, and the southernmost tip also dominated by the Peninsular Range Batholithic rocks. The study area includes parts of the northern and central subdivisions.

Most of the following discussion about the geology of Baja California is based on the work of Gastil et al. (1975), except where noted. In the northern part of Baja California, the exposed basement

rocks belong to three main groups: prebatholithic, Mesozoic batholithic, and postbatholithic.

The prebatholithic rocks can also be subdivided in at least three groups roughly aligned north-south as linear belts: the westernmost belt is composed of rocks of the Franciscan type whose range of ages reported vary from 95 to 145 my B. P.; to the east there is a belt of Mesozoic metavolcanics and volcanoclastic rocks (represented by the Alisitos formation). Paleozoic metasediments comprise the easternmost belt.

The batholithic rocks of the Peninsular Ranges Batholith are granitic intrusives of Mesozoic age. Krummenacher et al. (1975) dated these rocks in the range from 107 my on the west side of the peninsula to 62 my on the east side.

The postbatholithic basement rocks range in age from Late Cretaceous to Eocene time. These are represented by Cretaceous sediments and Tertiary sediments and volcanics.

The central-southern part of Baja California in the study area is dominated by Tertiary volcanics (represented by what has been loosely called the Comondu formation) which overlay the Peninsular Ranges Batholith.

Prominent faults in the northern part of Baja California include the Agua Blanca Fault, oriented almost east-west, and the San Pedro Martir Fault on the east side of the Peninsular Ranges.

The Salton Trough

The Salton Trough and the Laguna Salada are parts of a broad structural trough that extends from the southern end of the San Andreas Fault beneath the Salton Sea to the northern end of the Gulf of California. It includes the Mexicali and Imperial valleys, and is considered to be a northern structural continuation of the Gulf of California fault system (Kovach et al., 1962; Biehler et al., 1964; Elders, et al., 1972). The Salton Trough, the Laguna Salada and the northern Gulf are filled with sediments from the Colorado River that include lacustrine and deltaic silts, sands and gravels of late Tertiary age and onshore Quaternary alluvium (Elders et al., 1972). Geophysical models for the origin of the Salton Trough suggest the presence of an upper crust composed of low-density sediments and a lower crust composed of dense gabbroic material from the mantle. Several marine incursions are recorded in the sediments in the Salton Sea area (Kovach et al., 1962).

The Salton Trough is flanked on the west by the Peninsular Ranges Province and on the east by the Basin and Range and Sonora Desert Provinces. The most prominent faults in this area are the Elsinore, San Jacinto, San Andreas, Imperial, and Cerro Prieto.

According to several investigators (e.g. Lomnitz et al., 1970; Elders et al. 1972), local spreading centers, filled with sediments, are located beneath this area, and models have been proposed for the growth of the Imperial Valley. Elders et al. presented a model in which heating at the base of the crust takes place accompanied by rifting and upward expansion of the crust. The high sedimentation

rate from the Colorado River rapidly fills the rifting area and, as extension continues, basaltic intrusions are emplaced at the base of the trough, coincident with ductile thinning of the crust. Hot rising brines metamorphose the base of the sedimentary fill. If the temperature rises sufficiently, the granitic rocks start to melt causing rhyolitic volcanism at the surface.

The Sonora Desert and Sierra Madre Occidental

The Sonora Desert, located east of the Salton Trough and the northern Gulf of California, is a continuation into Mexico of the southern Basin and Range Province. It is a broad flat area covered with alluvial sediments of Quaternary age. Deeply eroded mountains of diverse composition and age, crop out from beneath this blanket of sediments. These range in age and composition from Precambrian and Paleozoic metamorphics to Tertiary sediments. Elevations range from 100 to 1500 meters. The general grain of these structures is in a northwest direction.

The Sierra Madre Occidental province is located east of the Sonora Desert province. This mountain range is about 320 km wide, its average elevation is approximately 2100 meters, and it extends southeast to about 14° N. The mountains are composed mostly of volcanics that overly intrusive rocks of Mesozoic age, although some sedimentary ranges occur near the northern end of the province.

POTENTIAL FIELD ANOMALIES AND BATHYMETRY

Data Location

OSU/IOM geophysical surveys were conducted in the Northern Gulf of California, north of 27° N, in the spring of 1981 (GOLFO-81), and again in the spring of 1984 (GOLFO-84). The trackline maps of figures 3, 5, and 7 show the data distribution for bathymetry, gravity, and magnetics respectively. Some land gravity data were collected during GOLFO-84, and some were obtained from the archives of the Defense Mapping Agency (DMA). The trackline separation in the survey area ranges to approximately 10 km, and the orientations of the tracklines were planned to be largely perpendicular to the dominant expected structures of the Gulf.

Navigation Data

The principal navigation system used on GOLFO-81 was a Magnavox 1107RS dual-frequency TRANSIT satellite receiver which yielded fixes approximately every 90 minutes. Gyro information was recorded to be used for dead reckoning between satellite fixes. Visual and Radar fixes were used to constrain course change points near shore. The navigation data were later adjusted to minimize differences in the gravity data at course changes and trackline-crossings, by comparing calculated versus observed Eötvös correction changes.

The principal navigation system used on the 1984 cruise was ARGO, a pseudo-range-range transponder system manufactured by the Cubic Western Corporation. Three shore-based transponders were established as shown on figures 3, 5, and 7. ARGO is a phase comparison, lane counting system operating at approximately 1.8 MHz. The estimated uncertainty in individual fixes is 5 meters within a lane. Lane ambiguity is about 80 meters. Lane identification was maintained using TRANSIT fixes. The shore-based transponders were located using Magnavox 1502 Satellite Navigators. ARGO propagates in a ground wave mode, providing positions at over-the-horizon distances of about 400 nautical miles during day light and about 100 nautical miles at night.

Gravity Data

In 1981, gravity measurements were made using LaCoste and Romberg Surface Ship Gravity Meter S-42 mounted on a 2-axes, gyro-stabilized platform. Digital data were recorded every 30 seconds. These measurements were tied to the International Gravity Base Stations at San Diego and Guaymas (see table 1), using L&R land meter G-126. For the 1984 cruise, the S-42 meter software was modified to correct for cross-coupling by cross-correlation in real time. On this cruise digital data were recorded every 10 seconds. L&R land meters G-706 and G-707 were used for the base ties, and also to obtain land gravity measurements in several places along the coast. During the processing of the marine gravity data, the Eötvös correction was calculated from the

navigation files. The free-air anomaly was obtained by subtracting the theoretical gravity values given by the International Gravity Field of 1967 (International Association of Geodesy, 1971), from the observed, Eötvös-corrected gravity values. The 1981 survey yielded an RMS crossing discrepancy of 4.4 mGal whereas for the 1984 survey the RMS crossing discrepancy was 1.5 mGal.

Table 1. Gravity base stations used during GOLFO-81 and GOLFO-84

| Location | Gravity (mGal) | Source | Station Designation in Source |
|-----------|-------------------|---------------|----------------------------------|
| San Diego | 979517.7 | Worzel (1965) | f |
| Guaymas | 979164.80 | LAGSN77 (*) | 9695-62 |

(*) The Latin American Gravity Standardization Net 1977, (Pan American Institute of Geography and History, 1977).

Magnetics Data

Total field magnetic measurements were made using a Geometrics G-803 Marine/Airborne Proton Precession Magnetometer. On the 1981 cruise data were recorded digitally every 30 seconds. In 1984, they were recorded every 10 seconds. The total magnetic field anomaly was obtained by subtracting the 1980 International Geomagnetic Reference Field (International Association of Geomagnetism and Aeronomy, Division I, Working Group I) values from the measured total magnetic field. No correction for diurnal variation was applied.

Bathymetry Data

Single channel bathymetric data were recorded continuously on an EDO graphic recorder, and later hand digitized at five minute intervals and at inflection points. Using the tables for the velocity of sound in sea water (Matthews, 1939 for the the 1981 data; and Carter, 1980 for the 1984 data) the depth values were corrected and expressed in meters.

Contour Maps

Bathymetry of the Northern Gulf

The data used to construct the bathymetric map of figure 2 are mainly from the GOLFO-81 and GOLFO-84 cruises. There were a few additional tracklines located south and southwest of Guaymas obtained during the OSU/IOM BAJA-76 and MARSUR-78 cruises. All of these data were superimposed on the bathymetric maps of Bischoff and Niemitz, (1980) and Lonsdale (1985) and then hand contoured. The resulting map is contoured at 200 m intervals with auxiliary 20 m contours for depths shallower than 200 m. Bold contours are shown every 1000 m. The Wagner Basin, located at 31° N, 104° 10' W, reaches a depth of 200 m. It is oval shaped, with its major axis oriented N-S. Just south of the Wagner Basin, the Consag Basin, also 200 m deep, has a more elongate shape and is oriented NW-SE.

A broader feature, reaching depths of more than 800 m at about $29^{\circ} 40' N$, $113^{\circ} 50' W$, is the Delfin Basin. The 400 m contour almost closes in the northern part of the basin near $30^{\circ} 10' N$, $114^{\circ} 00' W$ and it is oriented slightly NE-SW.

Between Isla Angel de la Guarda and the Peninsula of Baja California the Ballenas and Salsipuedes Basins trend southeast and reach depths of up to 800 m. Just west of the San Lorenzo island chain the Salsipuedes Basin reaches a depth of more than 1400 m. This extremely linear feature curves slightly to the east in front of San Lorenzo island and then continues to the southeast.

Between the San Lorenzo island chain and Isla San Esteban there is a small but deep feature, the San Lorenzo Basin with a depth of 1000 m.

The elongated Tiburon Basin, with depths of more than 400 m, extends subparallel to the general trend of the gulf from about $29^{\circ} 30' N$, $113^{\circ} 15' W$ to the southwest tip of Isla Tiburon, where it turns slightly eastward and follows the island coastline. Just west of Isla Tiburon the basin reaches its greatest depth of more than 600 m.

The San Pedro Martir Basin is slightly deeper than 800 m, and with an orientation similar to the Tiburon and Salsipuedes Basins. It extends southeast from $28^{\circ} 30' N$, $112^{\circ} 30' W$ to about $28^{\circ} N$, $112^{\circ} 5' W$.

The deepest feature in the area is the Guaymas Basin, which reaches its greatest depth of more than 2000 m at a linear feature oriented NE-SW located at about $27^{\circ} 30' N$, $111^{\circ} 30' W$. A similar

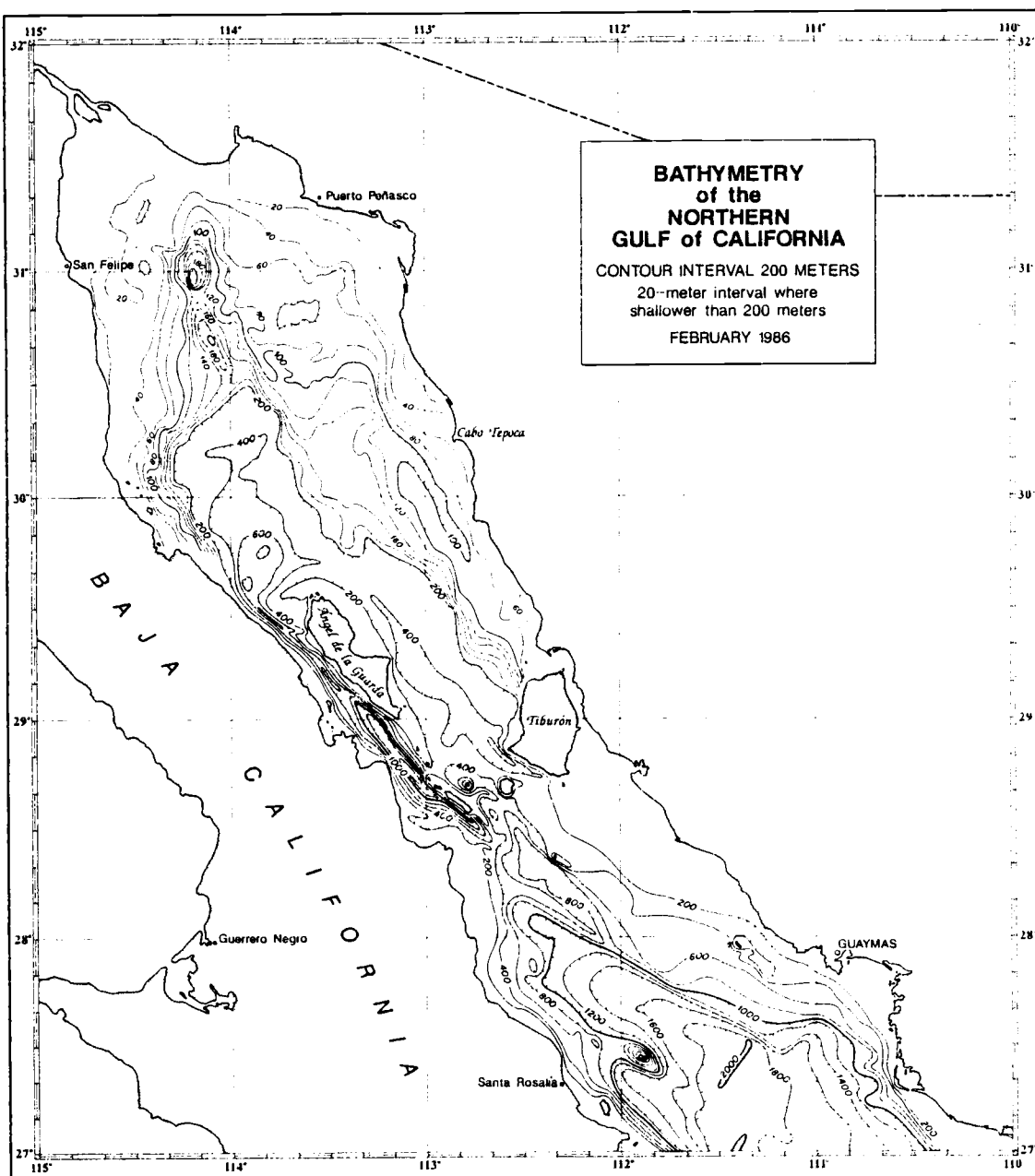


Figure 2. Bathymetric map of the northern Gulf of California.

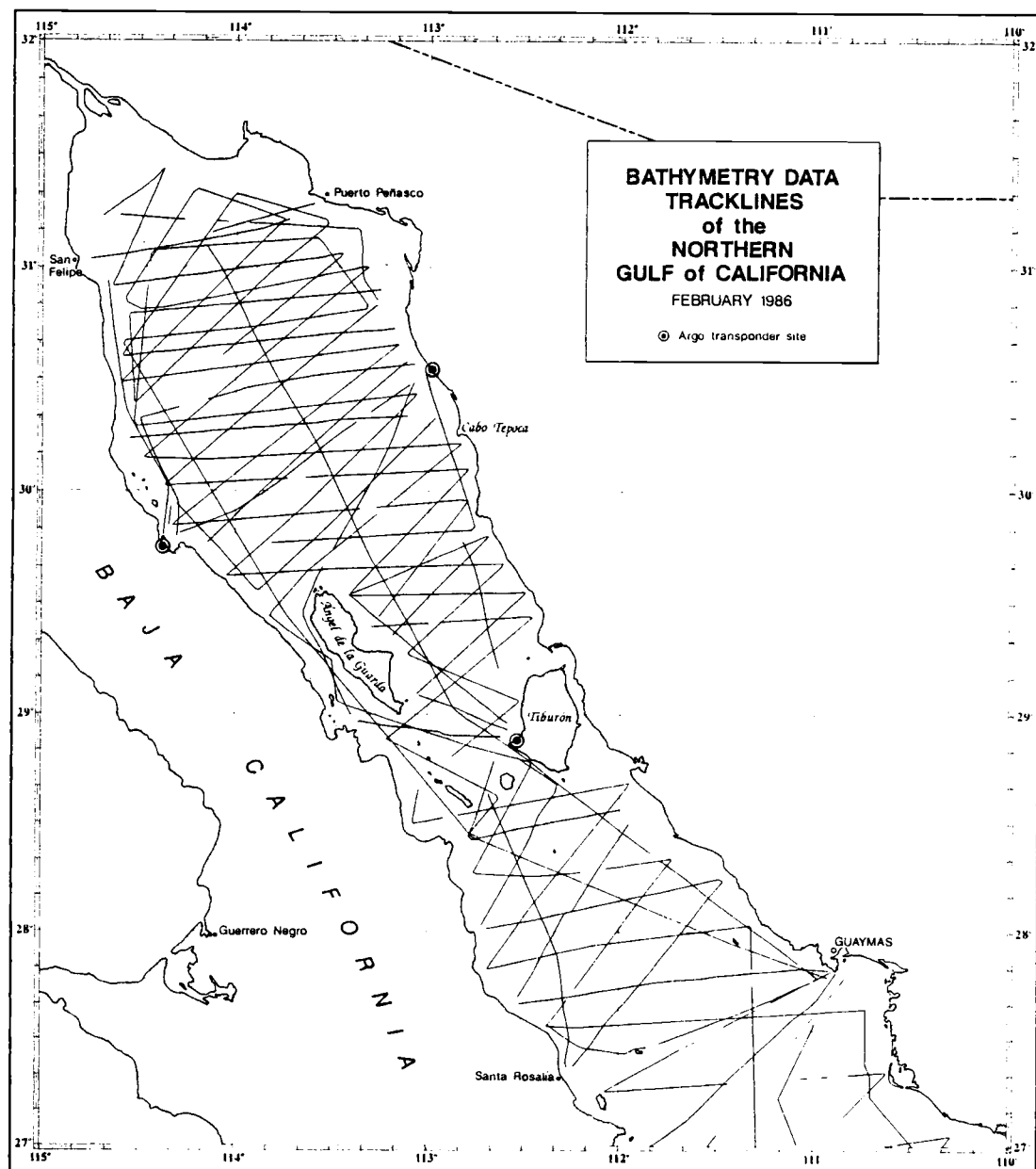


Figure 3. Bathymetric trackline map.

feature with the same depth and orientation is at the southernmost part of the map. A reentrant in the contours extends from the Guaymas Basin towards the city of Guaymas. This reentrant interrupts the otherwise remarkable linearity of the very steep escarpment at the northeast side of the Guaymas Basin.

Free-Air Gravity Anomalies of the Northern Gulf

The free-air gravity anomaly map (figure 4) covers the same area of the Gulf of California as the previously discussed bathymetric map. It too was constructed using the data from cruises GOLFO-81, GOLFO-84, along with some additional trackline data from BAJA-76 and MARSUR-78 cruises. The map is contoured at 5 mGal intervals and it shows bold contours every 20 mGal. The minimum anomaly value in the area is slightly less than -100 mGal and it is associated with the maximum depth of the Salsipuedes Basin. Maximum positive anomalies with values above 20 mGal occur near San Pedro Nolasco, Tortuga, and San Esteban islands.

In the center of the northern Gulf is a broad anomaly with values higher than -20 mGal, oriented subparallel to the general trend of the Gulf. It terminates at the northern end of Isla Angel de la Guarda. The western edge of the anomaly approximately coincides with the eastern edge of the Wagner, Consag, and Delfin Basins. Just north of 30° N, this anomaly widens toward the coast of Sonora, roughly coinciding with a bend in the bathymetric contours from 80 to 140 m. Two relative highs in the anomalies, with values of about 0 mGal, are located at 30° 15' N, 113° 45' W and 30° 20' N,

113° 10' W. These do not correspond with any topographic feature. A relative high of -5 mGal at 31° N, 114° 5' W lies east of the Wagner Basin. Another high of -5 mGal, oriented E-W at the north end of Isla Angel de la Guarda is located inside the 200 m depth contour.

The northeastern part of the map shows a linear, negative anomaly which reaches its minimum value of about -50 mGal at about 31° N, 113° 30' W and can be followed as far south as 30° 40' N. It is not related to any significant bathymetric feature, but is a linear extension of the onshore Cerro Prieto Fault.

A -10 mGal relative high southwest of Cabo Tepoca is located where a 100 m bathymetric contour extends south parallel to the coast.

Farther south, at approximately 29° 30' N and between the coast and 113° W, a series of linear highs and lows, oriented N-S range from -40 to -15 mGal and do not show any relationship with the bathymetry except for the westernmost part of the anomaly. This turns southeast at the southern part of Tiburon Basin.

The northwest part of the map shows several highs and lows ranging from -40 to -20 mGal, some of them associated with bathymetry. The -20 mGal contour around Consag Rock is a relative high. At about 30° 45' N, 114° 10' W, a -30 mGal closed contour is a relative low and is associated with the Consag Basin.

The area northwest of Isla Angel de la Guarda, is dominated by the gravimetric low produced by the Delfin Basin. This low extends to the southeast and merges with the very linear gravity minimum associated with the Ballenas and Salsipuedes Basins.

The gravity low of -45 mGal west of Isla San Esteban is associated with a deep, circular bathymetric depression, the San Lorenzo Basin. South of San Esteban, the very distinctive gravimetric expression of San Pedro Martir Basin, with a N-S trending anomaly of -50 mGal, turns to the southeast reaching a value of -55 mGal. It ends near 28° N, 112° W.

To the west, and trending N-S, a long, narrow anomaly which reaches a value of 0 mGal is almost parallel to the coastline and shows no relationship with bathymetry.

The larger negative anomaly between 27° N and 28° N is associated with the Guaymas Basin. Near 28° N it reaches -70 mGal and trends about 5° clockwise to the orientation of the gulf. It follows the shape of the northwestern part of the basin. The anomaly then turns to a direction of about 20° counterclockwise to the trend of the gulf and narrows, contrary to the bathymetric trend of the basin, which gets wider and deeper. This narrowing of the anomaly is caused by the ridge associated with Isla Tortuga. The anomaly reaches a minimum of less than -60 mGal at 112° W, coinciding with depths of 1400 to 1600 m. The anomaly turns towards Guaymas and becomes wider at about 27° 30' N, 111° W. A prominent reentrant in the gravity contours coincides with the bathymetric reentrant southwest of Guaymas. The minimum associated with the Guaymas Basin then continues to the southeast, off the map.

The -55 mGal closed anomaly south of Isla Tortuga seems to be related to the steep escarpment of the southwestern part of the Guaymas Basin. It is closed due to the gravity effect of the island

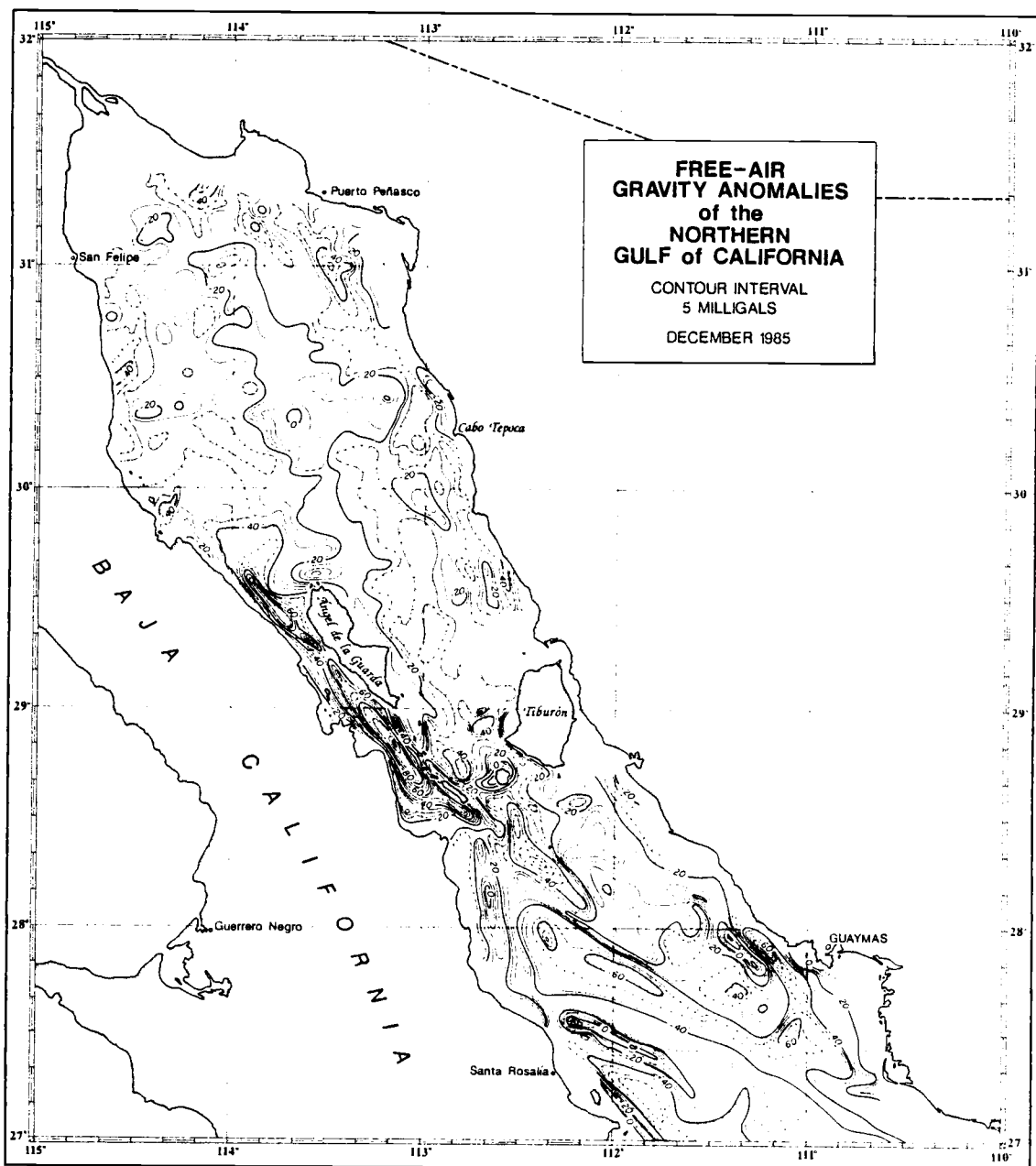


Figure 4. Free-air gravity anomaly map of the northern Gulf of California.

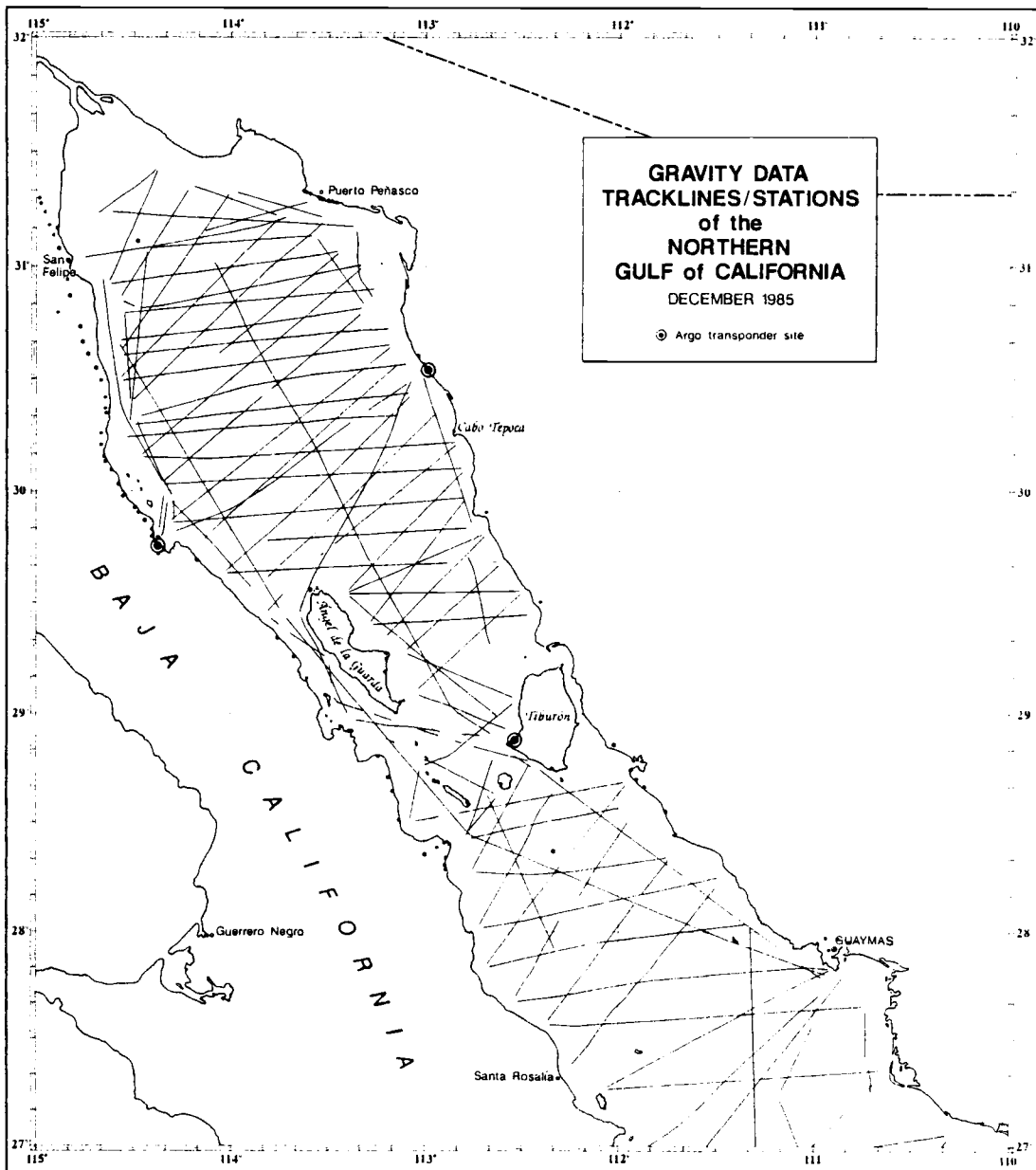


Figure 5. Gravity trackline map.

structure. The northeast extension of the -40 mGal contour is probably a manifestation of the deep linear structure at the southernmost part of the map.

The -70 mGal elongated anomaly east of Isla San Pedro Nolasco has no bathymetric expression, indicating that a linear pattern of mass deficiency is present beneath the sediments.

The area between the coast of Sonora, San Pedro Nolasco, San Pedro Martir, and Tiburon islands shows low amplitude anomalies compared to the surrounding areas.

Total Field Magnetic Anomalies of the Northern Gulf

The total field magnetic anomaly map of figure 6 is contoured at 50 nT intervals with bold contours every 200 nT. The most striking characteristic of this map is the area of relatively low amplitude anomalies north of 29° N, where values range from only -50 to 200 nT. This contrasts with the area to the south where the anomaly values range from -500 to 800 nT. In general, it appears that the amplitudes gradually increase in the northern Gulf as the sediment thickness decreases (Phillips, 1964). The lack of high amplitude anomalies has been observed in several other areas which are characterized by a thick sedimentary layer (Levi and Riddihough, 1986; Sumner, 1972).

North of 29° N, the most prominent feature is the parallel set of linear anomalies trending NW-SE. It reaches a minimum of -50 nT at 31° N, 113° 30' W. A maximum with the same orientation reaches values of up to 200 nT. The negative anomaly coincides with the

minimum free-air gravity anomaly described in the previous section. It is interpreted to be a submarine extension of the onshore Cerro Prieto fault (Ness and Lyle, 1988).

South of San Felipe and parallel to the coast of Baja California, isolated highs and lows, some of them closed, are associated with similar gravity anomalies. A closed contour of zero nT, oriented almost E-W and located at 31° N, 114° 10', is coincident with the Wagner Basin. The -50 nT anomaly located at 30° 40' N, 114° 10' W is coincident with the Consag Basin.

There is a low amplitude magnetic minimum north of 30° N, between 113° and 114° W. This feature occurs in the same area as a local gravity anomaly high and has a similar orientation.

Another anomaly reaches a value of 200 nT in front of Cabo Tepoca and is coincident with a gravity anomaly high, suggesting that high density magnetic materials, perhaps intrusive rocks, are present underneath these features.

A linear anomaly of -50 nT, oriented NW-SE and centered at 30° N, 114° W, seems to be related to that part of the Delfin Basin, and the 50 nT anomaly northwest of Isla Angel de la Guarda is associated with the deepest part of that basin.

West of Isla Angel de la Guarda a -150 nT anomaly corresponds to the northern end of the Ballenas and Salsipuedes Basins, the southern end changes to a 50 nT positive.

The Tiburon Basin magnetic anomaly is wider than the basin itself. It reaches a value of -100 nT just east of the southern tip of Isla Angel de la Guarda. This minimum extends to the southeast where it reaches a value of -200 nT south of Isla Tiburon. This

negative anomaly can be followed farther south, where it reaches values of -150 nT to the north and east of Isla San Pedro Nolasco.

The elongate maximum west of Isla Tiburon, oriented parallel to Tiburon Basin, reaches a value of 100 nT coincident with a -20 mGal gravity anomaly.

The longest anomaly in the area trends NW-SE from about 28° 30' N, 112° 50' W down to the end of the map near 27° 10' N, 110° 40' W. It reaches a negative value of -300 nT coincident with the southwestern edge of the San Pedro Martir Basin. Immediately south of 28° N, it changes to a positive anomaly which coincides with the northeast escarpment of the Guaymas Basin. Three closed anomalies within this general high, with values of 600, 800 and 300 nT, have corresponding negative anomalies of -250, -500, and -200 nT. The presence of a gravity high, located over this steep magnetics gradient, suggests that a high density magnetic body, perhaps an igneous intrusion, may be located beneath. The bathymetric contours between 1000 m and 1600 m in this area also suggest the presence of a body with sharp edges.

The 200 nT magnetic anomaly associated with Isla San Pedro Nolasco, and its parallel negative anomaly of -150 nT to the east, also correspond to similar gravimetric features.

An N-S oriented positive magnetic anomaly with values of up to 100 nT located at about 112° 35' W, between 27° 50' N and 28° 20' N, coincides with the eastern gradient of a similarly oriented gravity anomaly. These anomalies have no bathymetric expression. It is possible that an eroded, northern extension of the Sierra de las Virgenes in Baja California is manifested here.

Continuing to the south, two circular magnetic anomalies with values of 450 and -400 nT could represent the dipole of a small, circular magnetic body. Only a slight bending in the gravity and bathymetric contour lines suggests the presence of such a body beneath.

A positive anomaly is associated with Isla Tortuga. Several features above 200 nT, including one above 400 nT, are located south of the island. Surrounding these maxima, a negative anomaly reaches a value of -400 nT to the southwest of the island.

Two closed contours of 100 nT occur in the south and southwest parts of the Guaymas Basin.

A -200 nT minimum extends south and off the map. It appears to be related to the southern through of the basin.

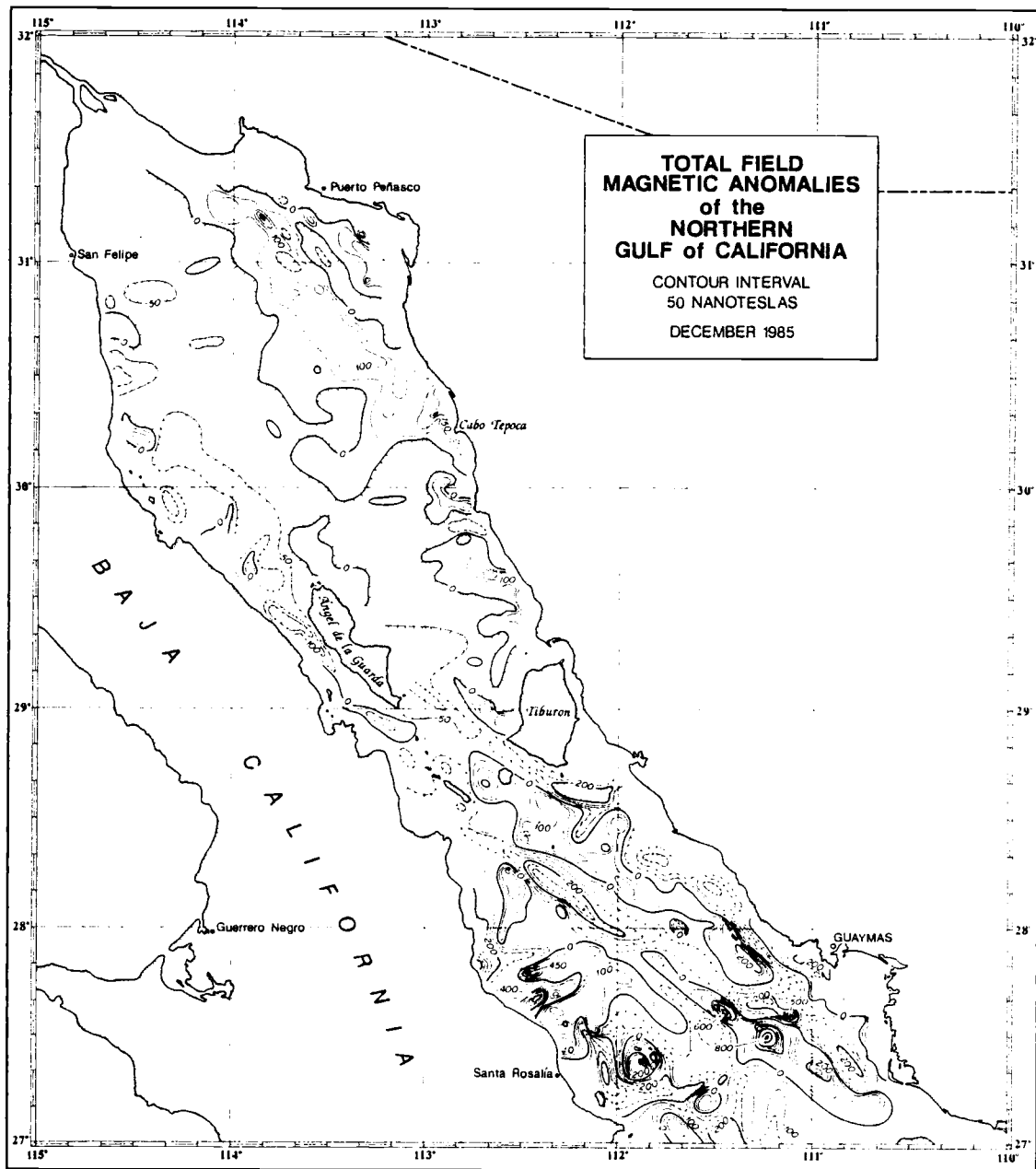


Figure 6. Total field magnetic anomaly map of the northern Gulf of California.

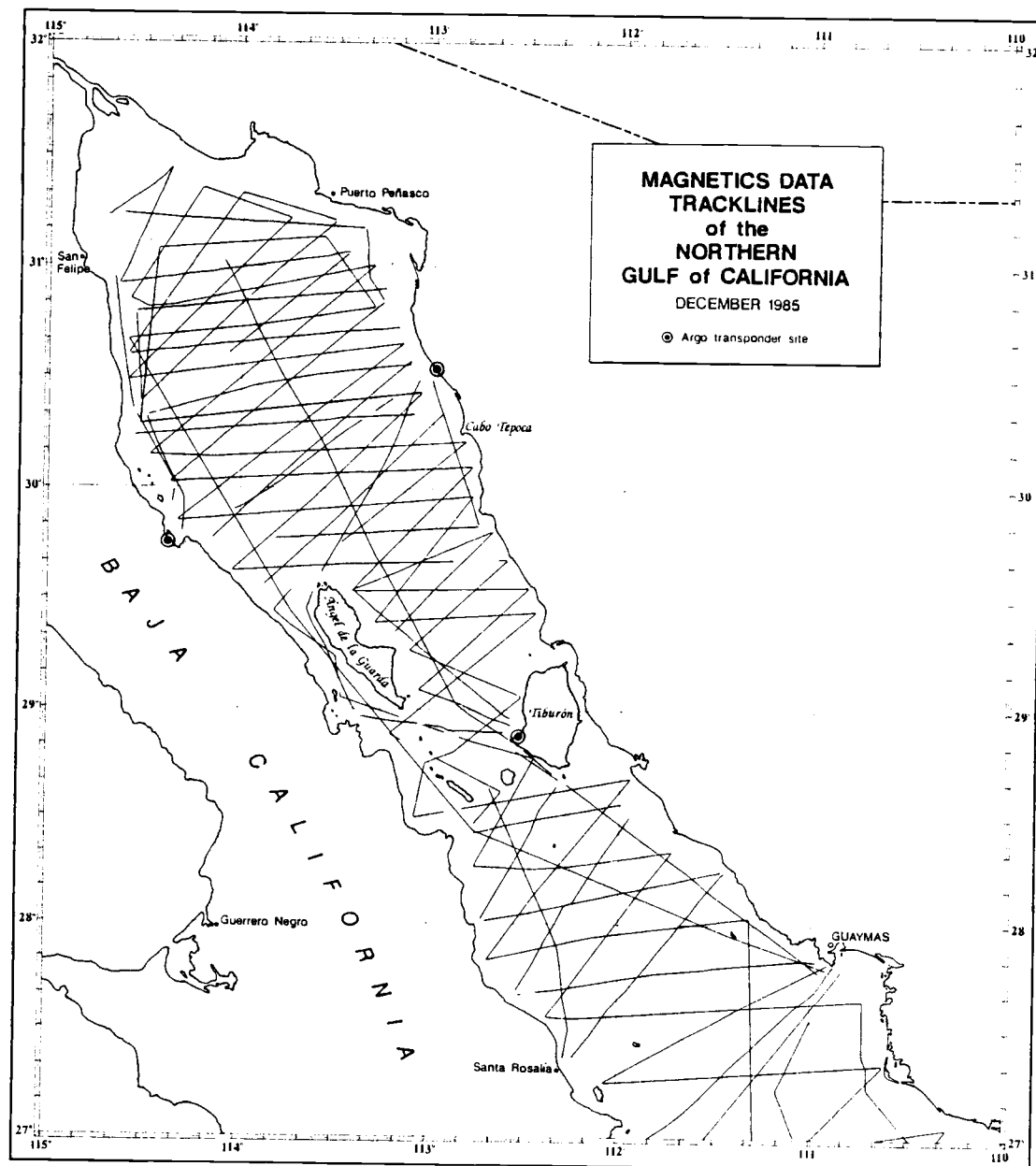


Figure 7. Magnetism trackline map.

DEPTH TO MAGNETIC SOURCES THE FFT APPROACH

The total field magnetic anomaly map of the Northern Gulf of California does not show the typical lineations of magnetic anomalies observed across sea-floor spreading centers (Klitgord et al., 1974; Larson et al., 1972), even though other evidence supports the idea that the area should be a zone of extension (e. g. Vine, 1966; Sykes, 1968; Moore and Buffington, 1968; Sykes, 1970; Lomnitz et al., 1970; Thatcher and Brune, 1971; among others). I use the OSU/IOM data to try to find where the spreading centers, and the faults that connect them, are located. I also wish to calculate the depths to magnetic sources in the northern Gulf.

Spector and Grant (1970), Mishra and Naidu (1974), Battacharyya and Leu (1975), Shuey et al. (1977), have described spectral analysis techniques to interpret aeromagnetic data. Through these techniques it is possible to estimate depths to the tops and bottoms of magnetic sources. McLain (1981), Connard et al. (1983), Foote (1985), and Huppunen (1983) used these techniques to obtain the Curie-point isotherm depths in the Oregon and northern California Cascades from aeromagnetic data. More recently, Blakely (1988) used the same technique with a slight modification to obtain Curie-point depths in the state of Nevada.

Most of those techniques were developed for the interpretation of aeromagnetic maps. However, without violating the assumptions made, it is possible to apply the techniques in this study and to use

the results to infer structures and temperature gradients, as well as the location of shallow high temperature areas.

In this work I follow Spector and Grant (1970), who developed the mathematical basis to interpret aeromagnetic maps using power spectrum analysis. Their technique is based on the assumption that the sources consist of several independent ensembles of vertical-sided prisms. Each ensemble is characterized by a joint frequency distribution for the depth h , width a , length b , thickness t , and direction cosines of magnetization L , M , N . Further assumptions are that the parameters a , b , h , t , etc., vary independently from one another and that the frequency distribution for each parameter is rectangular. The average inclination and declination of the magnetization vector (magnetic moment vector) is also assumed to be not very different from the inclination and declination of the magnetic field.

Using the expression for the energy spectrum of the total field magnetic anomaly produced by a single parallelepiped, and applying principles of statistical mechanics, Spector and Grant derived an expression for the energy spectrum of the magnetic anomaly caused by an ensemble of blocks. This allows the separation of parameters such as the depth, horizontal size, and thickness of the magnetic sources.

The final form of the energy spectrum in polar coordinates and after taking the average with respect to θ , is given by:

$$\langle E(r) \rangle = 4\pi^2 M^2 R_g^2 \langle R_p^2 \rangle \langle e^{-2h r} \rangle \langle (1-e^{-tr})^2 \rangle \langle S^2(r) \rangle \quad (1)$$

where:

$\langle \rangle$ represents the mathematical expectation,

$$r = \sqrt{u^2 + v^2}, \quad \theta = \tan^{-1} \left(\frac{u}{v} \right),$$

u and v are the spatial frequencies in the x and y directions respectively,

M = magnetic moment/unit depth,

R_g = geomagnetic field direction factor,

R_p = prism magnetization direction factor,

h = depth to the top of the prism,

t = thickness of the prism,

S = factor for the horizontal size of the prism.

Depth to the Top of the Magnetic Sources.

Data Processing

Gridding.- Using the minimum curvature algorithm of Briggs (1974), which consists of minimizing the curvature of a surface through the value at each grid point, the trackline data from the northern Gulf of California were used to make a grid from 29° N to 32° N, and from 115° W to 112° W.

Two different magnetic data sets were available, one from the 1981 season and one from 1984. Each data set covered approximately the same area. The 1981 cruise was planned to cover the area completely in a zig-zag manner with trackline separation ranging up to about 20 km. The tracklines for the 1984 cruise were run between the 1981 lines, so the total trackline separation was

reduced to about half. I attempted to combine both data sets but the resulting map was noisy, probably due to the difference in navigational quality between the two cruises. So, I made grids of each data set separately. The 1984 data set had a lower average trackline crossing discrepancy than the 1981 set, I decided to use only the 1984 data, rather than try to network adjust the two sets.

Due to the geographic orientation of the Gulf of California, the distribution of the data is generally NW-SE. The grids, however, were to be made N-S, E-W. In order to include as much data as possible in the gridding process. I made a single grid of the total area (256 by 256 km) including the parts with no data at the NE and SW corners. Afterward I selected smaller windows which contained as much data as possible.

I tried several different grid point spacings and analyzed the power spectrum of each. The best representation of the spectrum, without oversampling occurred at $\Delta x = \Delta y = 1.0$ km, but I decided to use 0.5 km for reasons which will be explained later.

The big grid was then subdivided (see figure 8) into two partially overlapping subgrids 128 km by 128 km in size, called N and C, and also into three partially overlapping subgrids 64 km by 64 km, called NE, SC, and SE. The upward and downward pointing triangles in figure 8 represent the centers of 50% overlapping subgrids, 64 km by 64 km, extracted from subgrids N and C respectively, and the centers of NE, SC, and SE are represented by circles. The nomenclature used for the 64 km by 64 km subgrids extracted from subgrids N and C is shown in figure 9. I will refer to

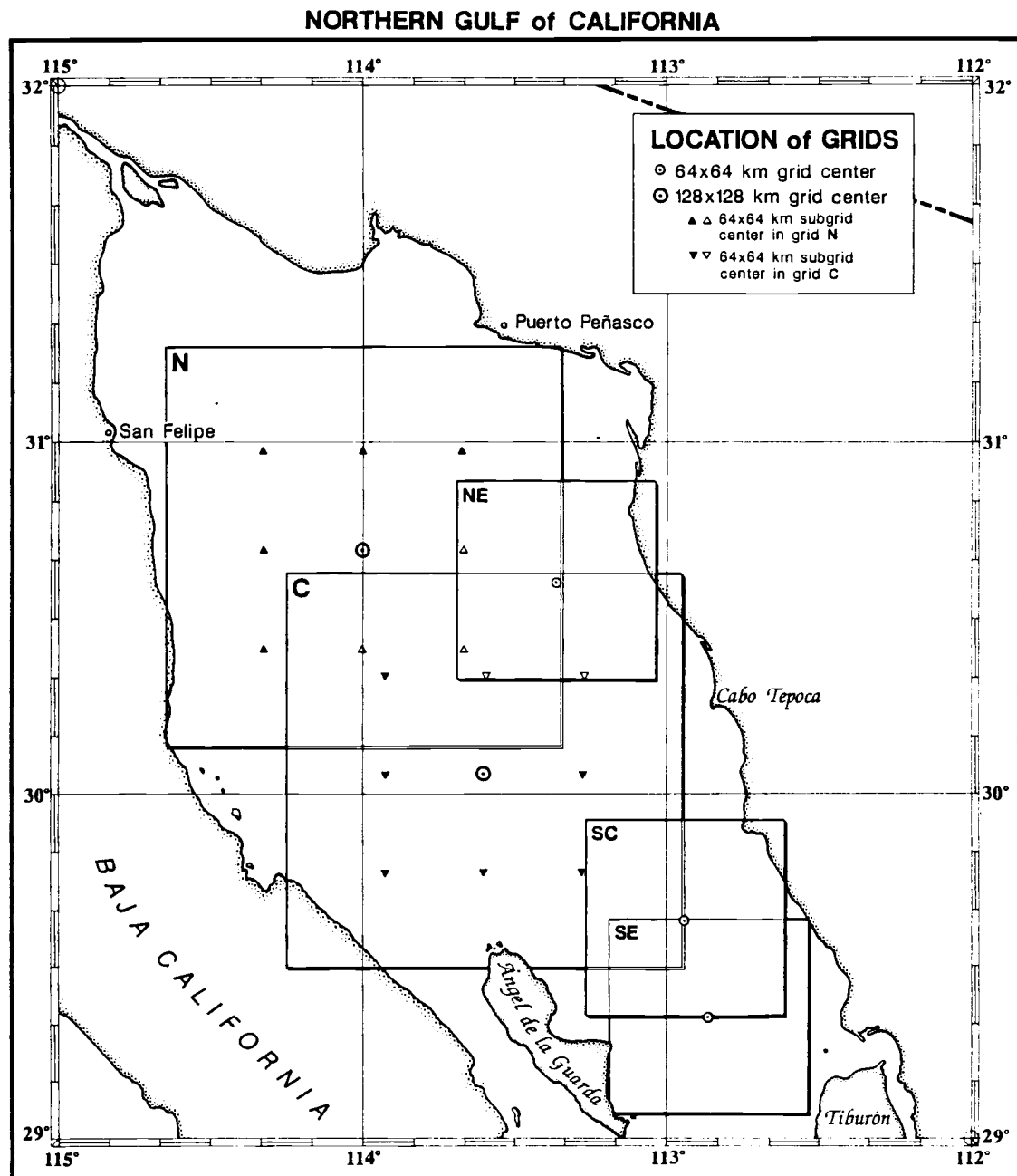


Figure 8. Location of grids in the northern Gulf of California.

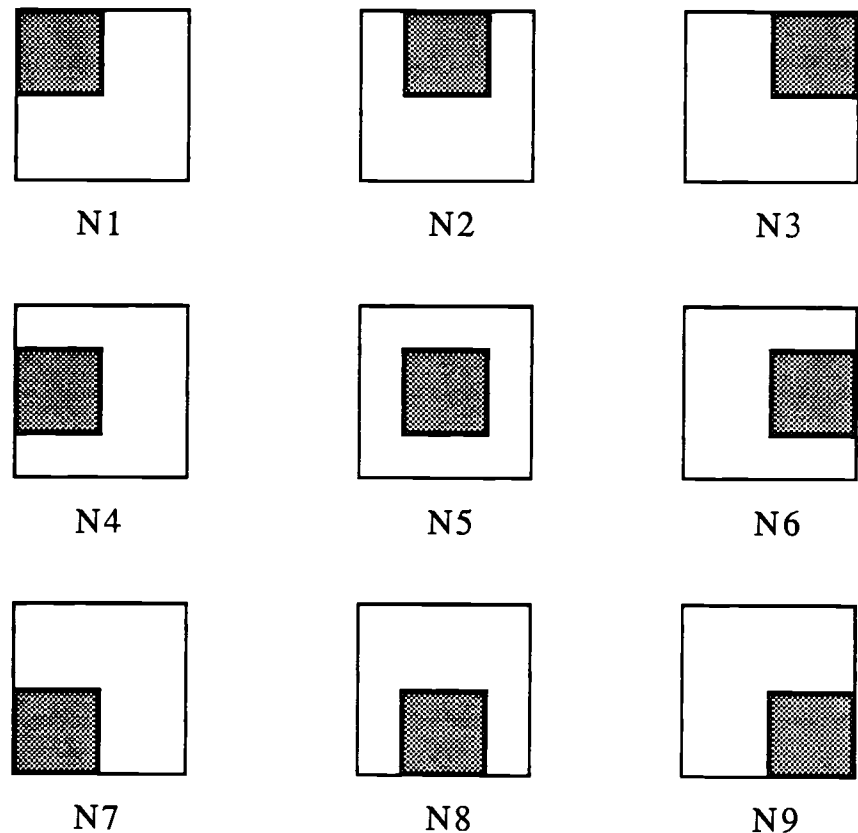


Figure 9. Relative location of the 64 km by 64 km subgrids inside a 128 km by 128 km subgrid.

the centers of the grids as points representative of the grid with the same names.

There are two reasons for choosing this particular size for the smaller windows. First, in order to resolve the depth to the bottom of the magnetic source, the size of the window must be at least $2\pi d$, where d is the depth to be resolved (Shuey et al., 1977). I expected source depths of approximately 10 km. Second, the algorithm for the two-dimensional Fast Fourier Transform I used requires the number of data samples to be some power of two.

The subgrids were used to compute depths to the magnetic sources. First, each subgrid was detrended and tapered independently, then the two-dimensional Fourier Transform was obtained. Finally the natural logarithm of the radially averaged two-dimensional power spectrum was calculated and plotted.

Detrending.- Detrending removes the mean along with any linear trend in the data so that the zero frequency component of the power spectrum is eliminated, and the estimate of the power spectrum is less distorted at all frequencies (Kanasewich, 1981, p. 126). The operation consists of a least-squares fitting of a first degree surface to the data and then subtracting it from the data.

Tapering.- Tapering the data is necessary to avoid the undesirable introduction into the power spectrum of high frequencies, caused by the large discontinuities that would otherwise occur at the edges of the data window. This was accomplished by applying a cosine bell, the Hanning window

(Kanasewich, 1981, p. 120 and 456), to 10 points around the edge of the data window. Using less than 10 points introduced high frequency components observable as a rise in the amplitudes of the intermediate and high frequencies. At the edges, the data is modified by the taper. In a way, data is lost. The problem becomes more severe when the data window is small. I found that, using the 10 point taper which is approximately 15 % of the data, the smallest size of a window should be 128 by 128 points in order to keep enough actual data in the set to estimate the spectrum. This is why I sampled at 0.5 km rather than 1.0 km. Fortran code and documentation for the detrending and tapering operations can be found in Connard (1979).

Two-Dimensional Fourier Transform.- Fortran code and documentation for the two-dimensional FFT algorithm used in this study can be found in McLain (1981).

Plotting the Radial Average.- I next obtained, for each window, the average of the two-dimensional power spectrum over rings of constant width (approximately the frequency spacing). These averages were normalized with respect to the zero frequency value. I then obtained the average of the radius of all the points inside the ring. This is the radial frequency. I then plotted the logarithm of the averaged values as a function of the average radius. These plots are shown in figures A1 to A21 in Appendix A (Figure A1 is reproduced as figure 10 for easy reference). Fortran

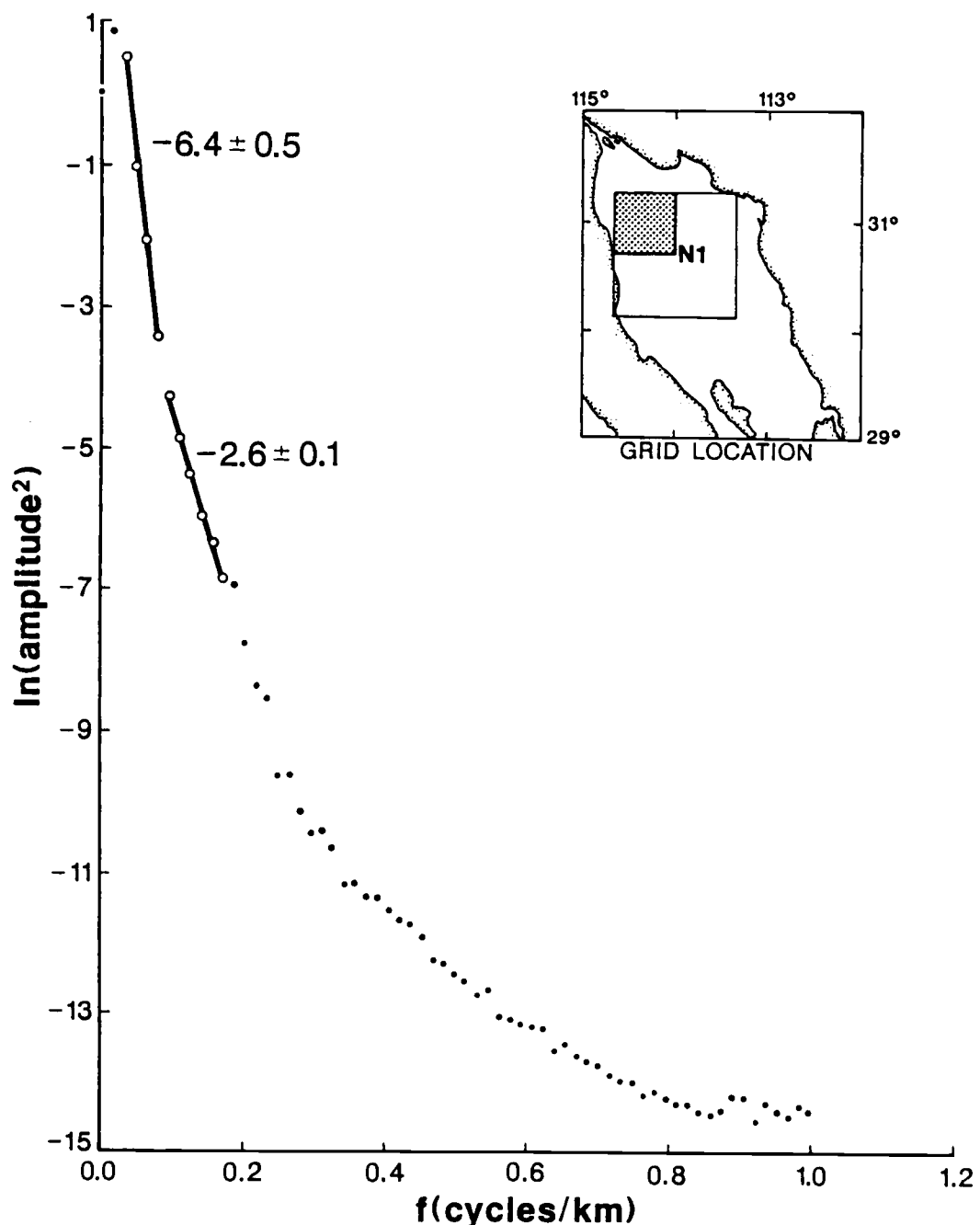


Figure 10. Radially averaged power spectrum of grid N1, using the 2DFFT. Straight lines are fitted by least squares. Numbers besides lines are depths in km below sea level. The \pm numbers are the errors in the least squares fitting. The map in the upper right corner indicates the geographic location of grid N1.

code and documentation for this program can be found in Boler (1978).

Each of these plots is equivalent to the graph that one would obtain by plotting the natural log of equation (1) vs the radial frequency f , ($f = r/2\pi$) (see figure A22). From these plots one can extract information about the various parameters of the ensemble.

Calculating Depth to the Top of Sources.- The slopes of the straight lines shown in figures A1 to A21, provide the average depth h to the top of the magnetic source according to the relationship $\langle e^{-2hr} \rangle \approx e^{-2hr}$, for variations of h that are not large, $\Delta h = \pm 0.5 h$ (Spector and Grant, 1970). The radial average plots are examined to look for straight line segments that could be fit by least-squares. This part of the process is subjective in the sense that the end points for the straight line are picked visually so as to minimize the standard deviation. A least-squares fitting is then applied through all points including the ends. The numbers besides the straight lines in figures A1 to A21 represent depths to the source tops in km below sea level, the \pm numbers represent standard deviations of the least squares fitting, and not standard deviations of the depths. Fortran code and documentation for this program can be found in Boler (1978).

Interpretation of Results

I analyzed the radial plots of figures A1 to A21 to obtain the depths to the magnetic sources by identifying linear segments on

the low frequency part of the spectral plots- segments which would have a small standard deviation upon least-squares fitting. Some plots showed three clearly distinguishable straight lines, other plots showed two, and one plot showed only one. The depths obtained were then classified into three groups: shallow, intermediate and deep.

Of the 21 grids analyzed, 9 allowed the identification of 3 distinct magnetic source tops: shallow, intermediate and deep. In 9 other grids I identified two source tops: shallow and intermediate. 1 grid showed shallow and deep source tops; 1 grid showed intermediate and deep source tops; and 1 grid showed only an intermediate source top. Table 2 is a compilation of these results.

Shallow Sources- Figure 11 is a contour map of the depths to the top of the shallow magnetic source with contours every 0.5 km. The shallowest depth of 2.3 km below sea level occurs at point N4 and the deepest one of 4.7 km at point N7. I used the depth to the intermediate magnetic horizon at point N7 to constrain the contours of the shallow magnetic horizon. Alternatively, I could have used the intermediate depth at point N8, or both. But the result would not have changed significantly. Using the value at point N7 seemed to be reasonable based upon a 2-d modelled geophysical cross-section recently constructed for the northern Gulf (Couch et al., 1988).

The average depth of the shallow horizon (using 20 values) is 3.1 km. This horizon shows an axial high trending almost N-S at a depth slightly shallower than 3 km. It is approximately parallel to

Table 2. Depths to the top and bottom of the magnetic sources, and computed heat flow.

| Grid | Depth to the top to the | | | Depth to Bottom (km bsl) | Heat Flow (mW/m ²) |
|------|--------------------------------------|--------------|------|-----------------------------|-----------------------------------|
| | Shallow | Intermediate | Deep | | |
| | Magnetic Source (km below sea level) | | | | |
| N1 | 2.6 | 6.4 | | 11.8 | 108 |
| N2 | 3.2 | 5.5 | | 10.1 | 126 |
| N3 | 3.2 | 6.2 | | 10.0 | 128 |
| N4 | 2.3 | 6.3 | | 7.0 | 182 |
| N5 | 2.4 | 6.2 | | 15.0 | 85 |
| N6 | 3.8 | 4.8 | 8.8 | 11.2 | 114 |
| N7 | | 4.7 | 8.9 | 11.5 | 111 |
| N8 | | 4.6 | | 12.6 | 101 |
| N9 | 3.2 | 5.7 | 8.3 | 10.5 | 122 |
| NE | 2.9 | 5.5 | 9.1 | 12.1 | 105 |
| C1 | 2.6 | 5.1 | | 15.5 | 82 |
| C2 | 3.6 | 6.0 | 7.2 | 10.7 | 119 |
| C3 | 3.5 | 4.8 | 7.7 | 11.2 | 114 |
| C4 | 2.9 | 5.8 | | 11.6 | 110 |
| C5 | 4.1 | 6.2 | 7.7 | 11.0 | 116 |
| C6 | 2.6 | 6.0 | 8.5 | 12.4 | 103 |
| C7 | 2.9 | 6.2 | | 12.1 | 105 |
| C8 | 2.9 | 3.6 | 8.2 | 11.9 | 107 |
| C9 | 3.2 | | | 9.5 | 123 |
| SC | 2.4 | 4.7 | | 10.5 | 122 |
| SE | 2.6 | 3.7 | 6.7 | 11.4 | 112 |

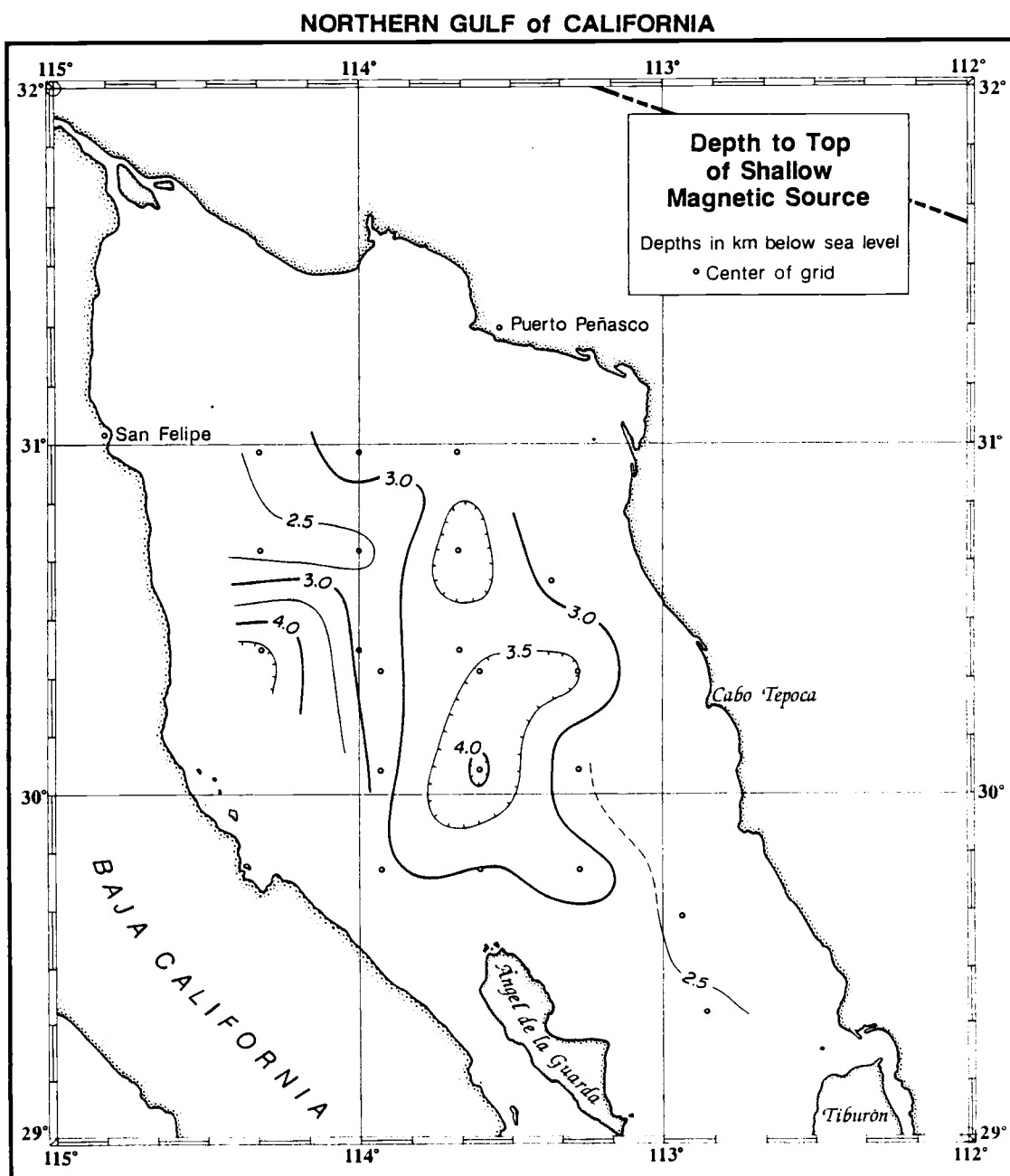


Figure 11. Contour map of the depth to the top of the shallow magnetic source in the northern Gulf of California.

the eastern edge of the Consag and northern Delfin Basins. At about $30^{\circ} 40' N$ the source depth contours bend in a NW direction towards the Wagner Basin. A N-S oriented minimum, with depths as low as 4 km, turns to a NE trend in front of Cabo Tepoca, with a similar orientation and position as a gravimetric high. The eastern and southern parts of this horizon are shallower than 3 km.

The depths obtained for this shallow source top horizon suggest that this is the top of the structural basement. Phillips (1964), using seismic refraction in the Gulf of California obtained an average sediment thickness of 3.5 km for the northern Gulf (Figure 12).

Intermediate Sources- The intermediate depth source top horizon exhibits very pronounced NE lineations (figure 13). This horizon is contoured at 1 km intervals with depths varying from 3.2 to 6.4 km below sea level. It is the most consistent horizon, appearing in almost every subgrid. The upper limit of 3.2 km corresponds to the shallow magnetic horizon. I use it to control the contours at point C9. The average depth for this horizon (using 21 points) is 5.3 km below sea level. A relative high, trending NE with values slightly shallower than 5 km, is flanked by two sub-parallel lows with values deeper than 6 km. The orientation of these intermediate depth lineations is almost parallel to the orientation of the sediment-covered crustal divergence zones shown on the seismo-tectonic map of Ness et al. (1988). The 6.0 km depth minimum near $30^{\circ} N$ approximately coincides in location and orientation with a minimum in the shallow magnetic horizon. The

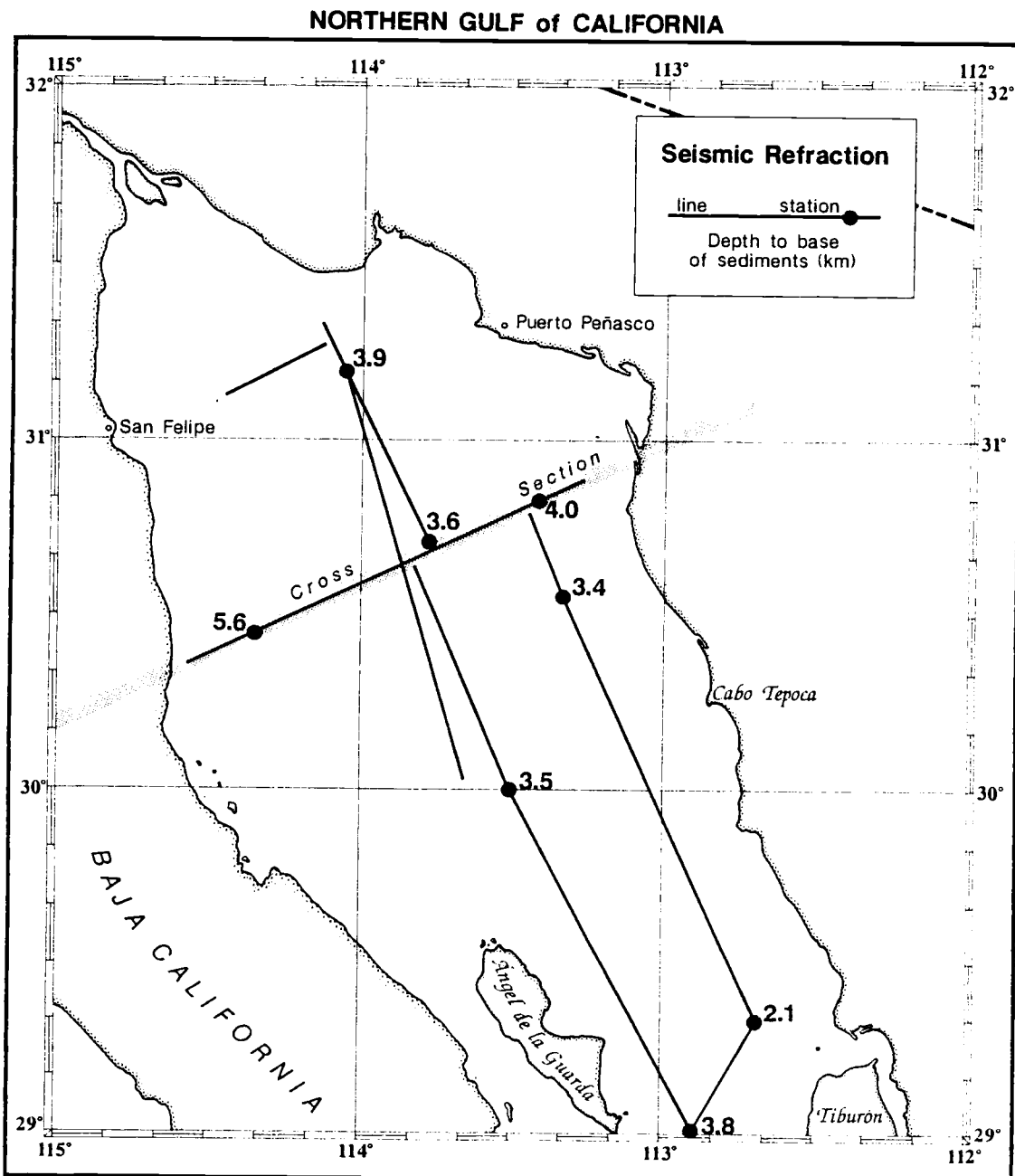


Figure 12. Location of the seismic refraction lines of Phillips (1964) and the geophysical cross section of Doguin (1988) in the northern Gulf of California.

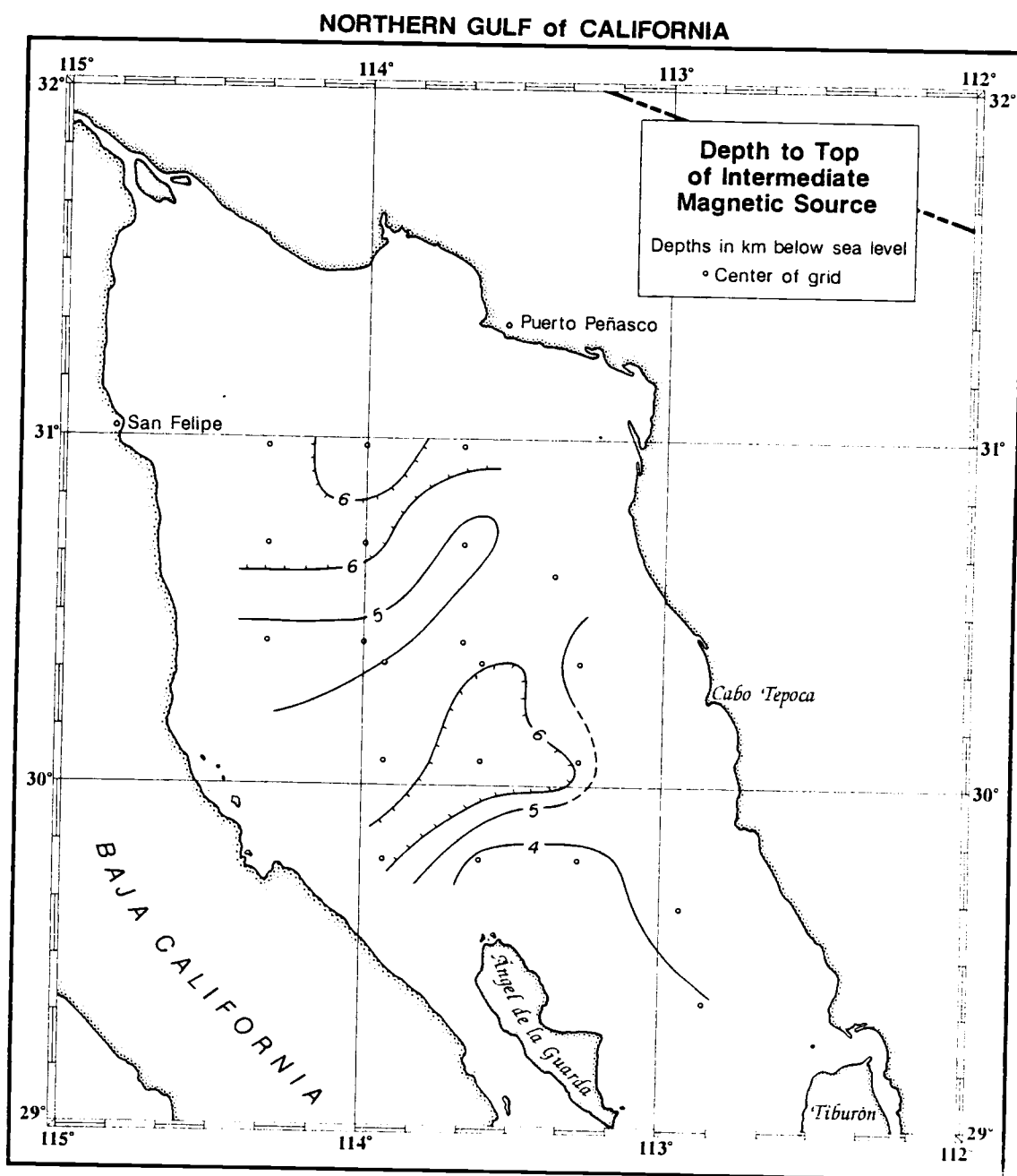


Figure 13. Contour map of the depth to the top of the intermediate magnetic source in the northern Gulf of California.

intermediate depth magnetic horizon shallows towards the south and southeast.

Deep Sources- The contours of the depths to the top of the deep magnetic sources shown in figure 14 are not very well controlled because several grids failed to show this depth, particularly the grids in the northwest part of the area. It is important to note that these contours show lineations which are similar in orientation to those of the intermediate source. The values for the depths here vary from 6.2 (using the intermediate source depths in the northwest) to 9.5 km. The contours shown are at 1 km intervals. A minimum, with a NE orientation in the center of the area and with depth values deeper than 9 km below sea level, is coincident with a relative high in the intermediate horizon. To the south a relative high with depths shallower than 7 km below sea level is coincident with a relative low in the intermediate depth horizon and has a similar orientation.

Depth to the Bottom of the Magnetic Source.

Calculating Depth to the Bottom of the Source-

According to the method first suggested by Spector and Grant (1970), and then elaborated upon by Shuey et al. (1977), Boler (1978) and Connard et al. (1983), the radial plot should have a peak near the lower frequency end of the spectrum if the bottom of the majority of the bodies which compose the magnetic source are shallow enough to be detected by the data window selected. If no

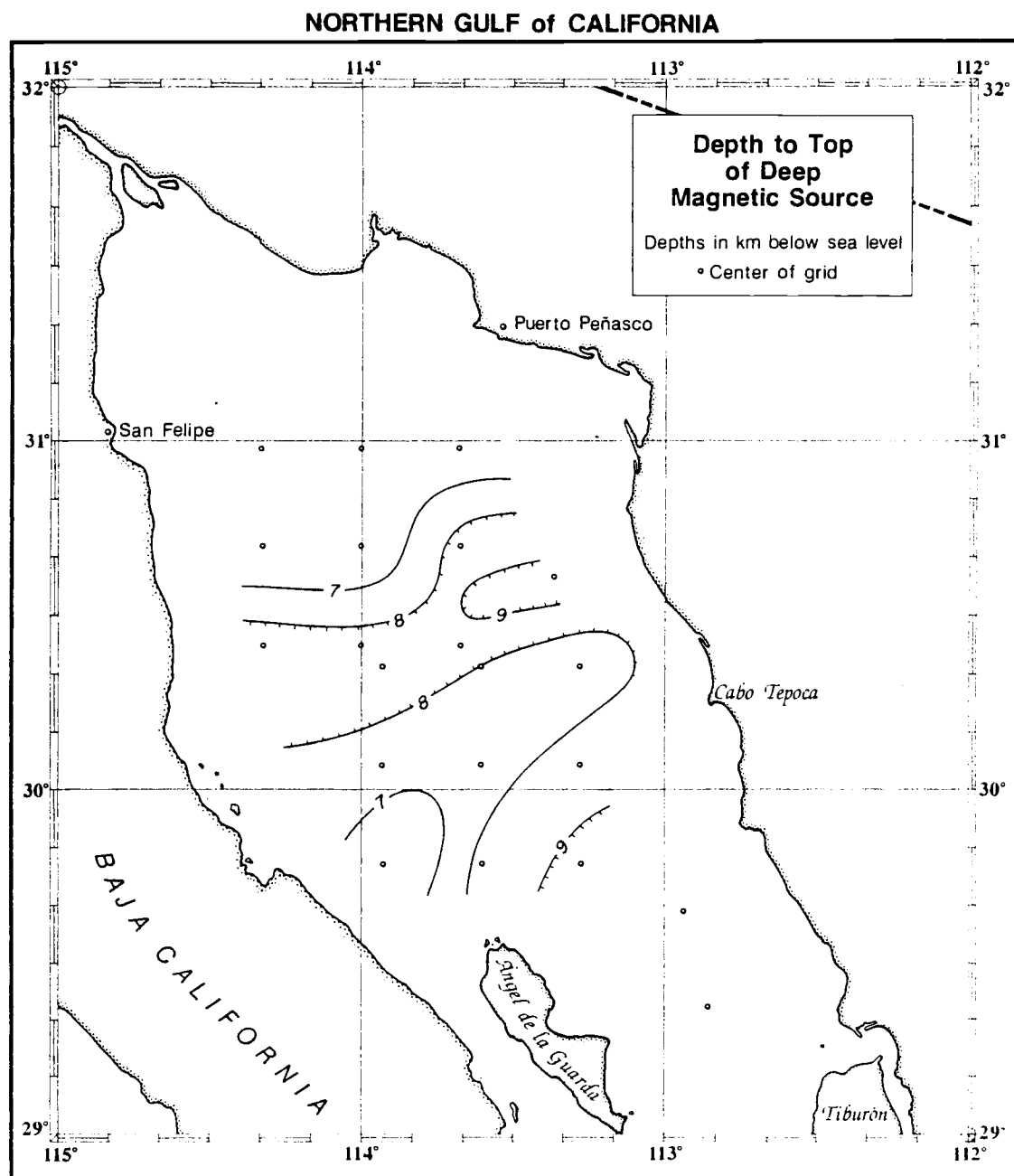


Figure 14. Contour map of the depth to the top of the deep magnetic source in the northern Gulf of California.

such a peak occurs, it means that the size of the data window is not large enough to detect the bottom.

From equation 1, the thickness factor $\langle(1-e^{-tr})^2\rangle$ in combination with the depth factor $\langle e^{-2hr} \rangle$ for small values of r , introduces a peak in the spectrum (Spector and Grant, 1970; see the plots of theoretical spectra in figure A22). The frequency where the peak occurs, combined with the average thickness of the ensemble (McLain, 1981), gives the depth to the bottom of the magnetic source according to the relation:

$$d = \frac{t}{1 - \exp(-2\pi t f_{max})} \quad (2)$$

where:

d = mean depth to the bottom

t = mean thickness

f_{max} = frequency where the maximum occurs.

The size of the data window determines the frequency resolution or frequency spacing. Because the data have been detrended, the zero frequency component of the energy spectrum should have zero amplitude. In the computations (due to rounding off) there may still be some energy which leaks into the zero frequency component. So the radially averaged energy spectrum is normalized with respect to the zero frequency component and becomes the radially averaged power spectrum. The radial plots, which are the logarithm of the averaged power spectra, will then have zero amplitude at zero frequency, and at least the

fundamental frequency component should have more energy. Even if this is the case, it does not mean that the peak has been located. In order to detect a clear peak, the maximum value has to be at least the third point which occurs at twice the fundamental frequency. In the case where the fundamental frequency component is the one with higher amplitude, the maximum must be between the first and third points, but it is not possible to determine precisely the frequency at which it occurs. In such cases I can only say that the maximum is somewhere between zero and twice the fundamental frequency. The frequency resolution is $1/L$. In order to increase it, the window size L must be increased. When the size of the data window is increased, bigger bodies may contribute more energy to the lower end of the power spectrum, making it more difficult to identify the peak.

In the radial plots shown in figures A1 to A21 maxima occur at the fundamental frequency $1/64 = 0.0156$ cycles/km. This is not the most desirable way of obtaining a peak. However, by synthetically increasing the size of the subgrids by appending zeroes beyond the ends of the tapered subgrids (Foote, 1985), I was able to better locate the frequencies f_{\max} at which the maxima occur. Figure A23 is an example of the radial plots that result when zeroes have been appended. The uncertainty in the determination of f_{\max} using this technique is ± 0.002 cycles/km. Depths to the bottom with this uncertainty in the determination of f_{\max} will in turn have uncertainties of ± 2 km, for the range of frequencies and depths in this study.

Table 3 was constructed using equation (2) by varying the thickness t , for different frequencies f_{\max} . Since $t = d + h$, the depth to the bottom d can be obtained from this table, having as input the depth to the top h and the frequency of the peak f_{\max} .

Curie-Point Isotherm Depths

The depths to the bottom of the magnetized crust (for each of the subgrids used in the previous section) were obtained using a table similar to table 3. These depths were computed to be between 10 and 15.5 km below sea level. The average is 11.5 km. The contours shown in figure 15 reveal a predominantly N-S orientation with local relative highs (shallower than 11 km) occurring in the center, north, northwest, and southeast of the area. The deepest source bottom of the magnetized crust was found at point C1. Together with point N5, this forms a low which is coincident with a rising of the top of the shallow magnetic source discussed in the previous section.

The bottom of the magnetic source can be either a lithological boundary or the Curie-point isotherm depth, the depth at which the temperature rises to a value at which the magnetic rocks lose their ferromagnetic properties. Here, I interpret the bottom of the magnetized crust as the Curie-point isotherm.

Studies of the magnetic mineralogy of the lower continental crust indicate that the predominant magnetic mineral constituent is magnetite (Frost and Shive, 1986). Curie temperatures, obtained by Wasilewski and Fountain (1982) at the Ivrea zone in northern Italy,

Table 3. Depth to the bottom d, vs depth to the top h, for several frequencies.
 (Depths in km below sea level, frequencies in cycles/km).

| f = 0.0156 | | f = 0.017 | | f = 0.018 | | f = 0.019 | | f = 0.020 | |
|------------|-------|-----------|-------|-----------|-------|-----------|-------|-----------|-------|
| h | d | h | d | h | d | h | d | h | d |
| 5.99 | 15.99 | 5.24 | 15.24 | 4.76 | 14.76 | 4.35 | 14.35 | 3.98 | 13.98 |
| 6.06 | 15.86 | 5.30 | 15.10 | 4.83 | 14.63 | 4.41 | 14.21 | 4.04 | 13.84 |
| 6.13 | 15.73 | 5.37 | 14.97 | 4.89 | 14.49 | 4.47 | 14.07 | 4.10 | 13.70 |
| 6.20 | 15.60 | 5.44 | 14.84 | 4.96 | 14.36 | 4.54 | 13.94 | 4.16 | 13.56 |
| 6.27 | 15.47 | 5.50 | 14.70 | 5.03 | 14.23 | 4.60 | 13.80 | 4.22 | 13.43 |
| 6.34 | 15.34 | 5.57 | 14.57 | 5.09 | 14.09 | 4.67 | 13.67 | 4.29 | 13.29 |
| 6.41 | 15.21 | 5.64 | 14.44 | 5.16 | 13.96 | 4.73 | 13.53 | 4.35 | 13.15 |
| 6.48 | 15.08 | 5.71 | 14.31 | 5.23 | 13.83 | 4.80 | 13.40 | 4.42 | 13.02 |
| 6.56 | 14.96 | 5.78 | 14.18 | 5.30 | 13.70 | 4.87 | 13.27 | 4.48 | 12.88 |
| 6.63 | 14.83 | 5.85 | 14.05 | 5.37 | 13.57 | 4.94 | 13.14 | 4.55 | 12.75 |
| 6.70 | 14.70 | 5.92 | 13.92 | 5.44 | 13.44 | 5.00 | 13.00 | 4.62 | 12.62 |
| 6.78 | 14.58 | 6.00 | 13.80 | 5.51 | 13.31 | 5.07 | 12.87 | 4.68 | 12.48 |
| 6.85 | 14.45 | 6.07 | 13.67 | 5.58 | 13.18 | 5.14 | 12.74 | 4.75 | 12.35 |
| 6.93 | 14.33 | 6.14 | 13.54 | 5.65 | 13.05 | 5.21 | 12.61 | 4.82 | 12.22 |
| 7.01 | 14.21 | 6.22 | 13.42 | 5.73 | 12.93 | 5.29 | 12.49 | 4.89 | 12.09 |
| 7.08 | 14.08 | 6.29 | 13.29 | 5.80 | 12.80 | 5.36 | 12.36 | 4.96 | 11.96 |
| 7.16 | 13.96 | 6.37 | 13.17 | 5.87 | 12.67 | 5.43 | 12.23 | 5.04 | 11.84 |
| 7.24 | 13.84 | 6.45 | 13.05 | 5.95 | 12.55 | 5.51 | 12.11 | 5.11 | 11.71 |
| 7.32 | 13.72 | 6.52 | 12.92 | 6.02 | 12.42 | 5.58 | 11.98 | 5.18 | 11.58 |
| 7.40 | 13.60 | 6.60 | 12.80 | 6.10 | 12.30 | 5.66 | 11.86 | 5.26 | 11.46 |
| 7.48 | 13.48 | 6.68 | 12.68 | 6.18 | 12.18 | 5.73 | 11.73 | 5.33 | 11.33 |
| 7.56 | 13.36 | 6.76 | 12.56 | 6.26 | 12.06 | 5.81 | 11.61 | 5.41 | 11.21 |
| 7.64 | 13.24 | 6.84 | 12.44 | 6.34 | 11.94 | 5.89 | 11.49 | 5.48 | 11.08 |
| 7.72 | 13.12 | 6.92 | 12.32 | 6.42 | 11.82 | 5.96 | 11.36 | 5.56 | 10.96 |
| 7.81 | 13.01 | 7.00 | 12.20 | 6.50 | 11.70 | 6.04 | 11.24 | 5.64 | 10.84 |

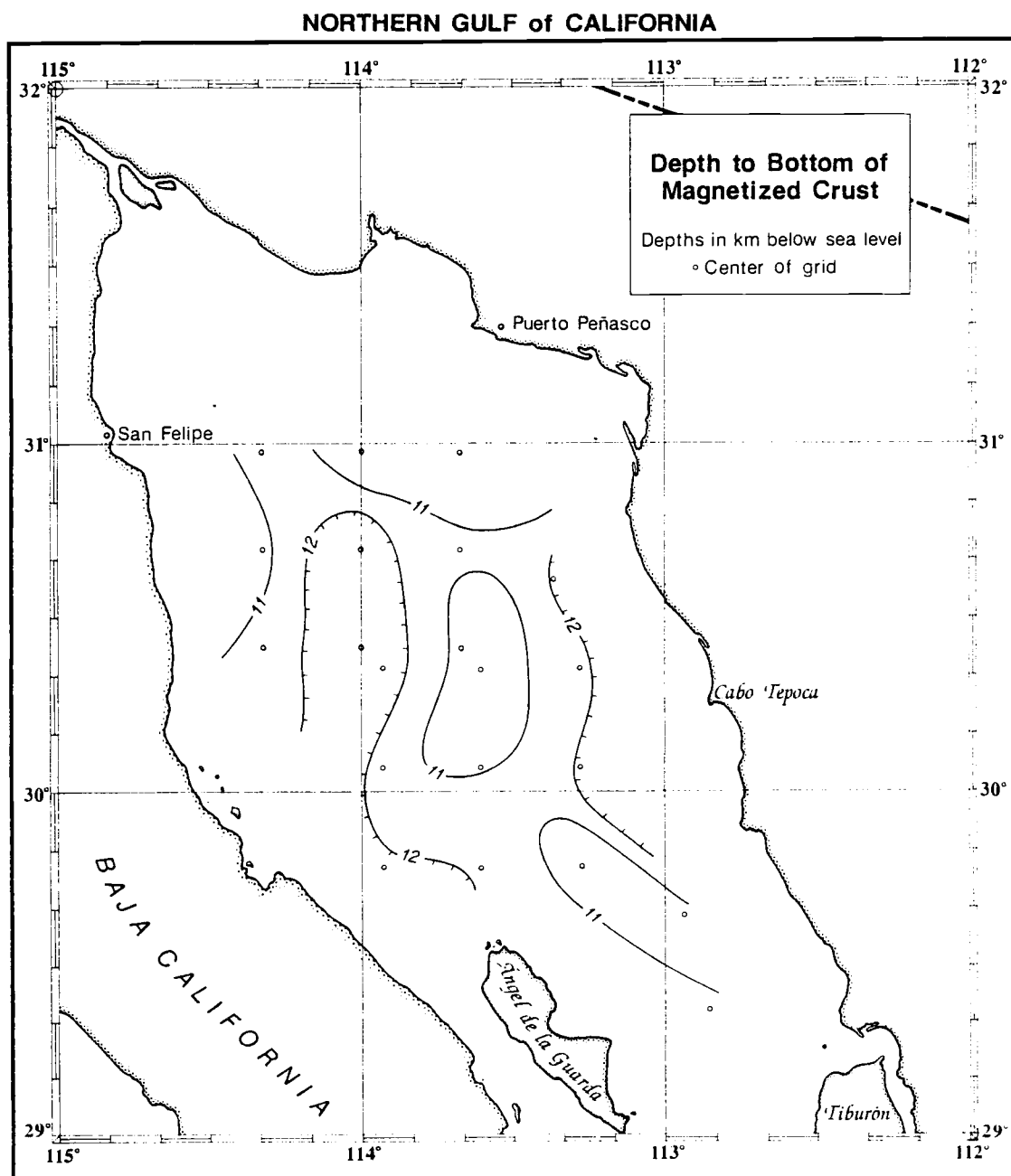


Figure 15. Contour map of the depth to the Curie-point isotherm in the northern Gulf of California.

by Schlinger (1985) from the Lofoten-Vesteralen terrain of Norway, and by Williams et al. (1985) at the Pikwitonei-Cross Lake subprovinces of Manitoba, all are in the range of 550° C to 580° C.

Smith and Banerjee (1986) from a study of the magnetic structure of the upper kilometer of oceanic crust at DSDP hole 504B, found that the Curie temperature for the lower zone (825-1350 m) is approximately 580° C. They divide the magnetic structure at hole 504B into three basic units: Upper units (274.5-845 m) composed of rocks similar to shallow extrusive marine basalts, a transition zone (845-1055 m) composed of a mixture of extrusive and dikes, and a dike complex (1055-1350 m). The upper units and the transition zone show considerable scatter in the Curie temperature with values ranging from 300° C to 500° C.

Seismic refraction studies by Phillips (1964) indicate that the northern Gulf is composed of 4 layers: 1.5 km of unconsolidated sediments, 2 km of semiconsolidated sediments, approximately 3 to 8 km (depending upon location) of highly variable upper basement, and between 10 and 17 km of lower crust. Phillips proposed, based upon the velocities and thicknesses obtained, that this 20 to 25 km thick crust is similar to the continental rocks which make up the mountain ranges which flank the Gulf. Two-dimensional geophysical models generated by Calderón (1978) and Doguin (1988) show, for the western part of the northern Gulf, an anomalous, high density material immediately below the base of the main crustal layer—perhaps representing lower crust modified by dike injection and sill emplacement as a result of rifting.

Based on the previous discussion it seems then reasonable to assume for this area a Curie-point temperature of 580°C. Assuming a thermal conductivity of 2.2 W/m°C, which is an average of appropriate sedimentary (Nobes et al., 1986) and igneous rock (Stacey, 1977) thermal conductivities, I have calculated the heat flow in the northern Gulf using

$$q = K \frac{dT}{dZ}$$

where:

$\frac{dT}{dZ}$ is the vertical temperature gradient,

K is the thermal conductivity of the material where the gradient is measured, and

q is the heat flow.

Figure 16 shows the location of measured and computed heat flow values in the northern Gulf. They are represented by diamonds and open circles respectively. The average of the computed heat flow values is 114 mW/m² (2.7-HFU), and the average of the measured heat flow values is 99.6 mW/m² (2.38-HFU) (Heney and Bischoff, 1973). The locations of the measured heat flow values were apparently selected to be in areas where high heat flow could be expected. They represent local values. However, the average of the computed heat flow, which covers a larger area, is slightly higher than that of the measured heat flow. The computed heat flow then is higher and covers a broader area. This suggests that a pattern of simple, en echelon transform faults and spreading

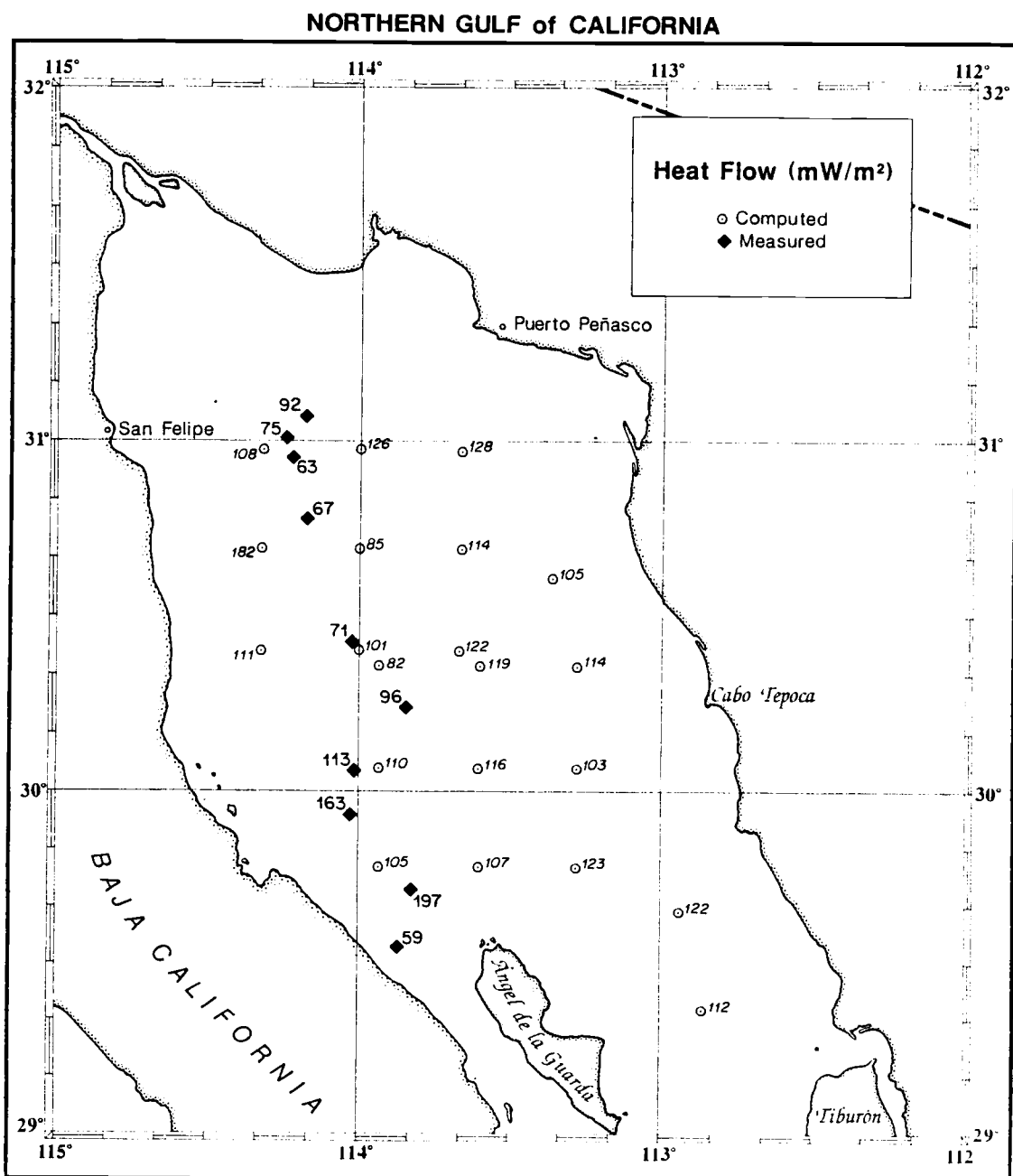


Figure 16. Computed and observed heat flow in the northern Gulf of California.

centers may not be that well developed beneath the sediments of the northern Gulf. Spreading is probably still very unorganized or diffuse.

The base of the crust near the eastern flank of the northern Gulf, according to Phillips (1964) seismic refraction studies, appears to be about 25 km below sea level, and the seismic velocities are similar to those found in the Salton Trough (Kovach et al., 1962). The average heat flow for the Imperial Valley reported by Lachenbruch (1985) is 140 mW/m^2 . The mean heat flow values within the grabens of continental rift zones are in the range of 90-110 mW/m^2 (Morgan, 1982).

Pérez C. (1982) reports that, in the northern Gulf, direct measurements in the well Caborca-1, at 4250 m depth, yielded a temperature of 153°C and a thermal gradient at the bottom of the well of 80°C/km . By extrapolating these values, he calculated a temperature of 550°C at a depth of approximately 9250 m. My Curie-point isotherm depth determination at point N2, which is geographically closest to Caborca-1 well, is 10.2 km. This yields a thermal gradient of 57°C/km . The average thermal gradient from Pérez C. is 59°C/km .

The computed heat flow pattern does not show clearly localized areas of high heat flow. I interpret these results to mean that the northern Gulf is a zone of diffuse crustal extension in an early unorganized stage of rifting. Alternatively, the diffuse heat flow pattern may be due to the regional character of the calculations when using the 2DFFT method for obtaining the power spectrum.

Blakely (1988) states that estimates of Curie-point isotherm depths obtained with this method must be accepted with caution. Since the method is based on an inversion technique, mathematical instabilities and nonuniqueness are unavoidable. Some authors (e.g. Haggerty, 1978; S. Levi, personal communication) caution against assuming a single Curie-point temperature, since values as low as 300° C in continental crust may exist due to the low temperature oxidation of titanomagnetite. However, my calculations using 580° C are in agreement with the heat flow observed, as well as, with the regional tectonics interpreted with other geophysical techniques such as seismic refraction, earthquake seismology, gravity, magnetics, and the observations in the well Caborca-1.

In the following chapter I attempt to increase the horizontal spatial resolution of the depth determinations by using a high resolution method of spectral estimation.

DEPTH TO MAGNETIC SOURCES THE MAXIMUM ENTROPY APPROACH

There is a problem with frequency resolution when estimating the power spectrum of a process with a finite number of observations. The smaller the total number of observations, the less frequency resolution in the estimate of the spectrum (Kanasewich, 1981). In the previous chapter I used the squared amplitude of the two-dimensional FFT (2DFFT) to obtain the power spectra of data windows. The minimum size of those windows was set to obtain a reliable spectrum with adequate frequency resolution, while keeping the size of the windows as small as possible to obtain adequate horizontal spatial resolution.

The smallest windows that I could use, given the restrictions imposed, were 64 by 64 km (128 by 128 points), which allowed me to obtain a depth calculation every 32 km. Here, I am interested in reducing the size of these windows to improve the horizontal spatial resolution of depth estimates. What is needed is a high resolution method for obtaining the power spectrum; one that would allow the use of smaller data samples.

A high resolution method of spectral estimation will not increase the frequency resolution inherent in the window size, but will increase the resolution of the estimate; in other words, it will obtain a "good" spectral estimate with short data samples.

A considerable amount of research has been conducted in the last few years on the subject of high resolution two-dimensional spectral estimation (e.g. Capon, 1973; Newman, 1977; Pendrel, 1977;

Roucos and Childers, 1980; Ulrych and Walker, 1981; Justice, 1981). In particular, Ulrych and Walker have tested several algorithms using synthetic data. I will follow their approach to two-dimensional spectral analysis using maximum entropy.

For the sake of simplicity in this discussion, I will begin with maximum entropy spectral analysis (MESA) in the one-dimensional case.

1-D Maximum Entropy Spectral Estimation.

Entropy, as used in the context of information theory, can be interpreted as a measure of the uncertainty that a system will exhibit in a particular state. From this point of view it is similar to its use in thermodynamics, where it measures the degree of disorder of a physical process (Kanasewich, 1981). Burg (1967) showed that it is possible to obtain the power spectrum of a given data set by generating from it a new data set which shows the most randomness and has the maximum entropy. This is referred to as the Burg algorithm or the maximum entropy method, MEM. Several mathematical reviews of Burg's algorithm for the estimation of power spectra have been offered (e.g. Lacoss, 1971; Edward and Fitelson, 1973; Chen and Stegen, 1974; Newman, 1977). Here, I will summarize the method. A more detailed development is given in Appendix B.

By use of the optimum filter theory of Wiener, a prediction error filter (PEF) may be obtained. A PEF is a filter which, when convolved with input data, produces white noise as an output. The

input power spectrum can then be obtained by correcting the output power spectrum for the response of the PEF.

$$\text{Input Power Spectrum} = \frac{\text{Output Power Spectrum}}{\text{Power response of filter}}$$

Burg's method for generating a PEF consists of obtaining a two-term PEF from the data. Then higher-order terms are obtained recursively. Andersen (1974) gives details on how to implement this technique. By using this technique to obtain the PEF, two very important conditions are satisfied: It uses only the known autocorrelation values, and it ensures that the PEF has an inverse spectrum.

Extension of the Theory to 2-D

It is straight-forward matter to extend the theory from 1-D to 2-D in conventional methods of power spectrum estimation such as the autocorrelation or periodogram estimators. This is not the case in MEM (Justice, 1981; Ulrych and Walker, 1981; Lim and Malik, 1981). However, several attempts have been made to obtain power spectral estimators in two-dimensions within the framework of maximum entropy.

Newman (1977) shows that it is possible to extend the link between MEM and autoregressive modelling to higher dimensions. But other authors point out that the constrained equations are

highly non-linear and no closed solution has yet been given (e.g. Lim and Malik, 1981; Justice, 1981).

Roucos and Childers (1980) derived a 2-D ME spectral estimator from an extrapolation of the 2-D sampled autocorrelation function. They warned that the method could yield a negative power spectral density estimate, although it did not occur in their experiments.

Lim and Malik (1981) developed an iterative technique to obtain ME power spectral estimates for 2-D signals. Their approach can also be used for 1-D signals as well as higher dimensions. The problem is that the algorithm may or may not converge.

In this study I adopted a method to obtain the 2-D power spectrum developed by Ulrych and Walker (1981). This consists of the repeated application of 1-D estimators as explained below:

Let a_{uj} represent the complex Fourier transform of each column of an array s_{ij} , and let b_{uj} represent the scalar quantity obtained by taking the square root of the MEM spectral estimate of each column of s_{ij} .

We can form a partial transformation

$$t_{uj} = b_{uj} \frac{a_{uj}}{|a_{uj}|}$$

which combines the amplitude of the MEM estimate with the phase of the discrete Fourier transform.

We then apply the complex Burg algorithm to each row of t_{uj} to obtain the two-dimensional power spectrum P_{uv} .

Next, we obtain Q_{uv} in the same manner as P_{uv} except that this time we operate first on rows and second on columns.

Then combine P_{uv} and Q_{uv} to cancel their orthogonal biases

$$S(u,v) = \frac{P_{uv}Q_{uv}}{P_{uv} + Q_{uv}}$$

Ulrych and Walker tested the method using synthetic data. A cosine function with two frequencies was used to create a 16 by 16 point grid. The power spectrum was estimated using a 7 by 7 PEF. Their results were very satisfactory when compared with other estimates, including the periodogram or Bartlett estimates.

Experimental Results Using 2-D Maximum Entropy

Synthetic Data.- The Fortran source code for the 2DMEM computer program, provided by Tad Ulrych and Colin Walker (Walker, personal communication), was implemented at Oregon State University. It was tested with the same synthetic data set used by Ulrych and Walker (1981). I tested different PEF sizes, as well as different output sizes. With an input array of 16 by 16 points, a PEF of 7 by 7 or 9 by 9 points, and an output size of 64 by 64 points, the two input frequencies were clearly detected in the power spectra.

One of the first observations from this test case is that the PEF size (NPEF) which best reproduced the spectrum is 1/2 the input size ± 1 . A second observation is that with a larger NPEF, the higher

amplitudes in the power spectrum shift toward low frequency and eventually make the zero frequency component unacceptably large. A smaller NPEF tends to excessively smooth the power spectrum.

Real Data.- One of the magnetic anomaly grids (grid N1, 128 by 128 points at $\Delta x = \Delta y = 0.5$ km) analyzed in the previous chapter was used for the purpose of testing the 2DMEM with real data. I started with the detrended and tapered grid and obtained the two-dimensional maximum entropy power spectrum using a NPEF of 63 points. I then obtained the natural logarithm of the radially averaged power spectrum as described in the previous chapter. I refer to this plot as radial average N1.BTP.

Figures 17 and 18 show the radial average plots which correspond to grid N1 using the 2DFFT (N1.FTP), and 2DMEM (N1.BTP) respectively. These two radial plots are very similar, in fact almost identical in shape. I conclude that the 2DMEM estimate using the 63 points PEF is adequate for the purpose of reproducing the radial plot obtained with the 2DFFT technique. I next obtained the radial plot using the 2DMEM on the same grid, but now without the taper. I refer to this radial plot as N1.BDT.

Figure 19 shows the radial average plot of the 2DMEM (N1.BDT) power spectrum estimate for grid N1 without taper and using a 63 point PEF. A comparison of this plot with N1.FTP or N1.BTP shows that, except for a constant shift, this is also an adequate reproduction. Similar tests were run on several other grids of real data, and the results were consistent with the observations in the previous example.

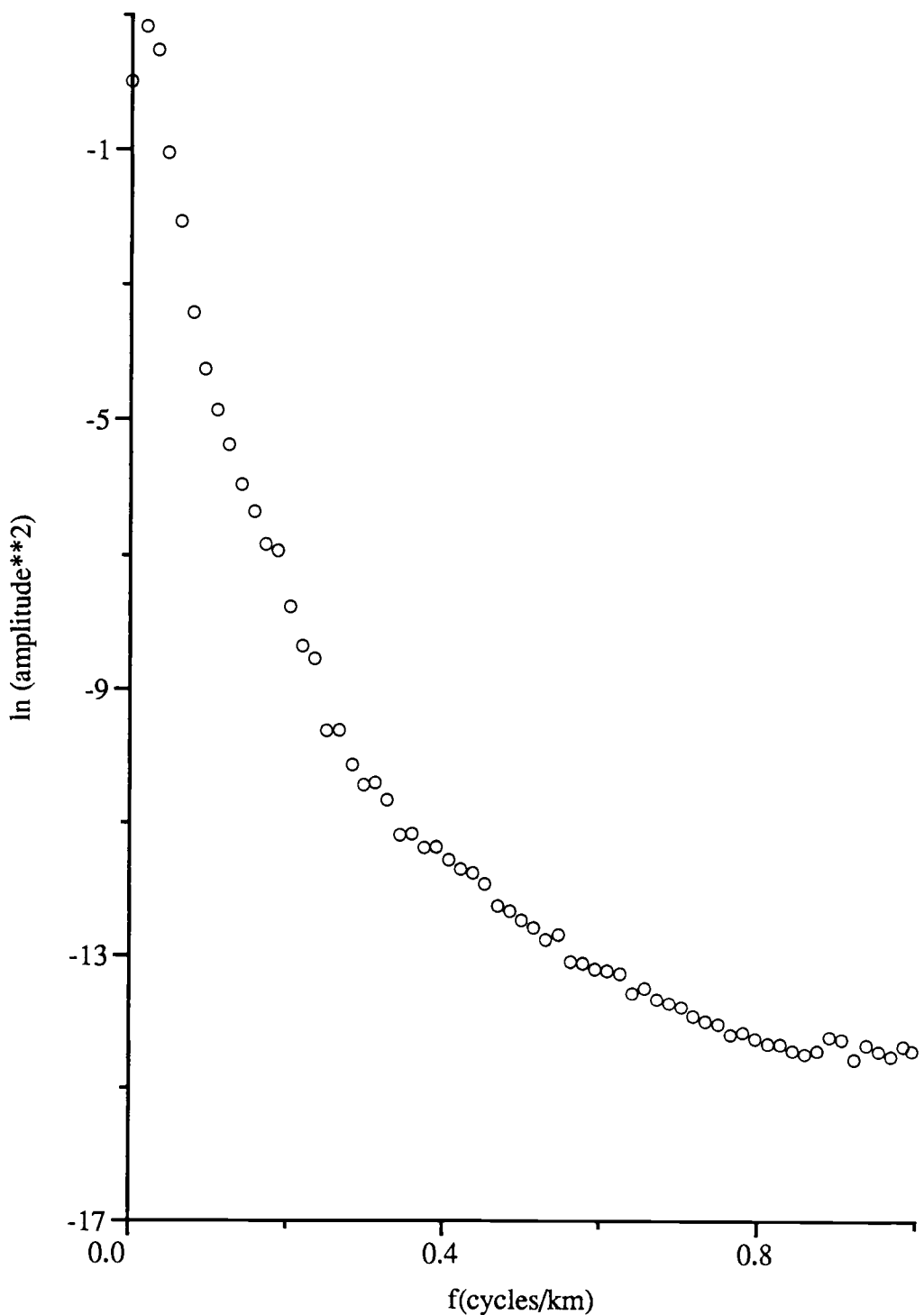
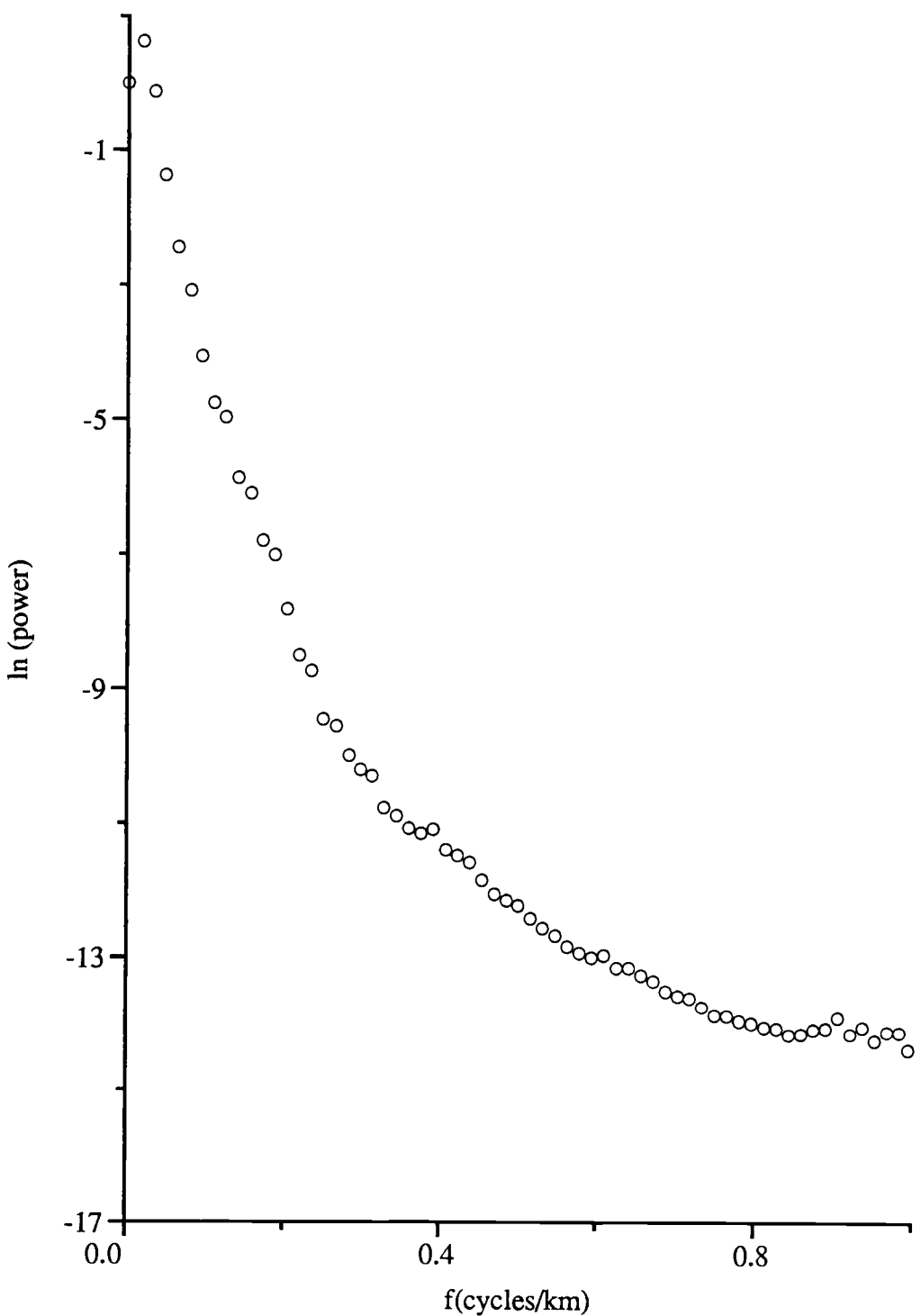


Figure 17. Radially averaged power spectrum of grid N1, using the 2DFFT. The grid was previously detrended and tapered.



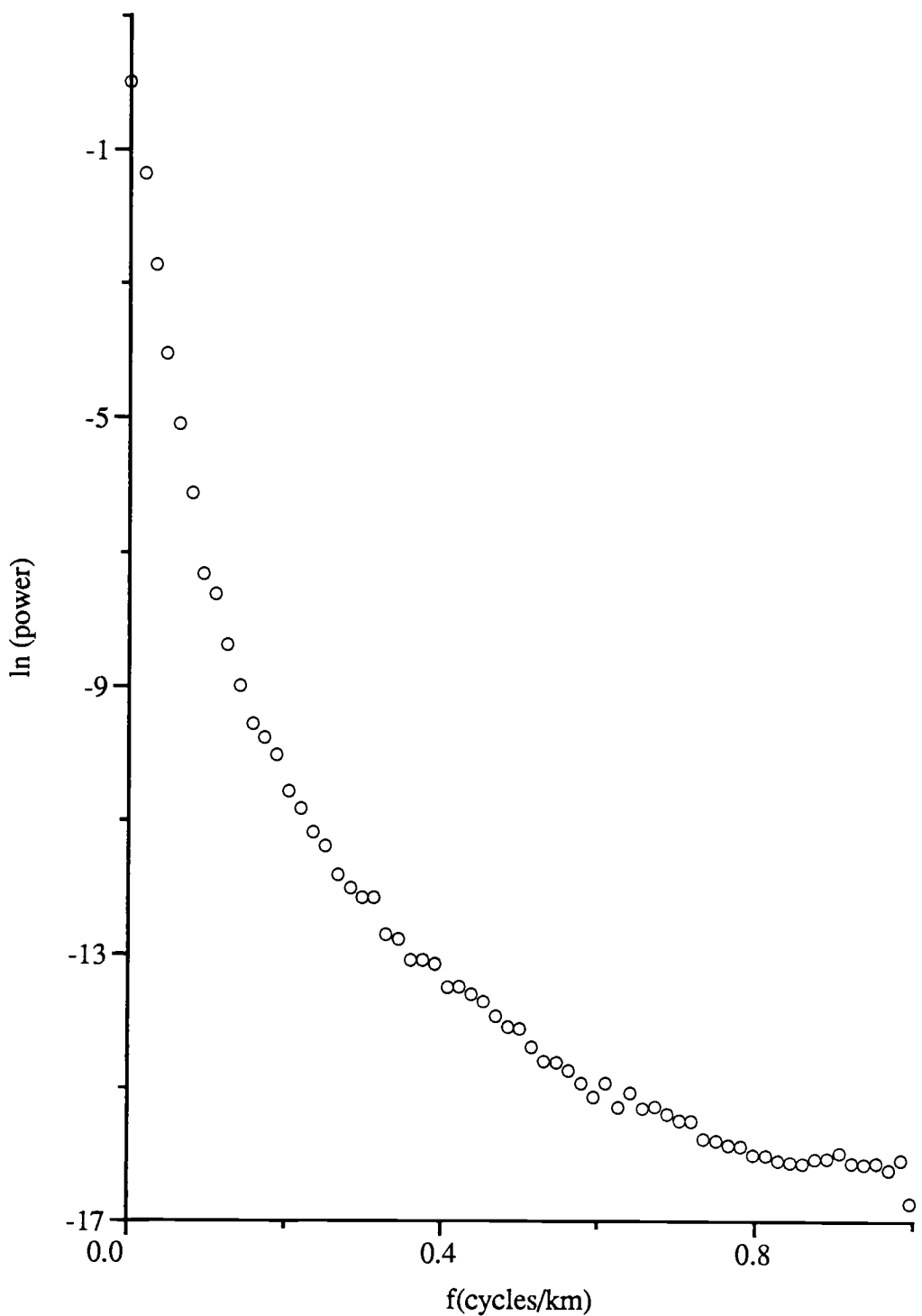


Figure 19. Radially averaged power spectrum of grid N1, using the 2DMEM. The grid was previously detrended but not tapered.

Using the same criteria to interpret the radial plots, that is, selecting straight segments having small standard deviations, I calculated the depth to the top of the magnetic source using radial plot N1.BDT, and compared it with the depth obtained using radial plot N1.FTP. The depth of the 2D MEM approach with the non-tapered grid is only about 5% deeper than the one obtained with the 2DFFT approach with a tapered grid. The first observation then is that depths obtained using 2D MEM on non tapered grids is in good agreement with ones obtained in the conventional way.

A second observation is that, in the 2D MEM approach, only one magnetic source was clearly defined. More than one source could probably be identified, but with higher standard deviations than I thought to be acceptable.

A third observation is that the maximum value necessary for obtaining depth to the source bottom, was not identifiable, since that part of the frequency spectrum is highly influenced by the size of the PEF and, as mentioned before, it can make the zero frequency component very large. This obscures the position of the maximum in the radial plot needed to locate the frequency and determine the depth to the bottom of the magnetic source.

The following two sections discuss some important points to consider when using MEM.

Detrend and Taper

As a standard procedure, when using the 2DFFT method as in the previous chapter, the data are detrended and tapered. The reason for tapering the data in the conventional approach is to avoid sharp discontinuities at the edges of the data. However, the tapering procedure introduces some modification to the original data.

In the MEM, the predictive character implicit in the method requires no such operation. This has the advantage that the original data are not modified and shorter data segments can be used. Detrending though is recommended in most cases.

Prediction Error Filter Size

Another important factor to consider when using MEM is the size of the prediction error filter (NPEF). Based on the Final Prediction Error, Akaike (1969) proposed a method to obtain a NPEF which produces the minimum error. Galbraith (1971) used the prediction error as a criterion for operator length in deconvolution. Blakely and Hassanzadeh (1981), experimenting with synthetic data, concluded that a NPEF between 0.25 and 0.75 the size of the data sample gives reliable spectral estimates. Chen and Stegen (1974), also using synthetic data, found that a good estimate is obtained with a NPEF about 0.3 the size of the sample.

By trying several NPEF's I found that "good" spectra, were obtained using a NPEF of $N/2 - 1$, N being the size of the data sample. This applied in both cases: when I used real data and the 2DMEM was compared with the 2DFFT approach, and when I used synthetic data.

Application of 2DMEM to the Northern Gulf of California Magnetic Data

In order to apply the 2DMEM to the analysis of the northern Gulf of California magnetic data, I again extracted 50 % overlapping windows 32 by 32 km from the grids used in the 2DFFT approach. These subgrids were half the size of the smallest grids used in the 2DFFT method. The location of the center of these grids and their names are shown in figures 20 and 21 respectively. The names of the 32 by 32 km grids are taken from their position with respect to the ones used in the previous chapter; N, C, NE, SC, and SE. Some of these grids were discarded because they did not contain enough trackline data.

The 32 by 32 km subgrids were detrended independently and the power spectra were obtained using the 2DMEM with a NPEF of 31 points (15.5 km). Then the radial plots were obtained as described in the previous chapter.

I used the radial plots shown in Appendix B to calculate depths to the top of the magnetic source, as described in the previous chapter, by first obtaining the slopes of the straight lines fitted by least squares and then using the relationship $\langle e^{-2hr} \rangle \approx e^{-2hr}$. Table

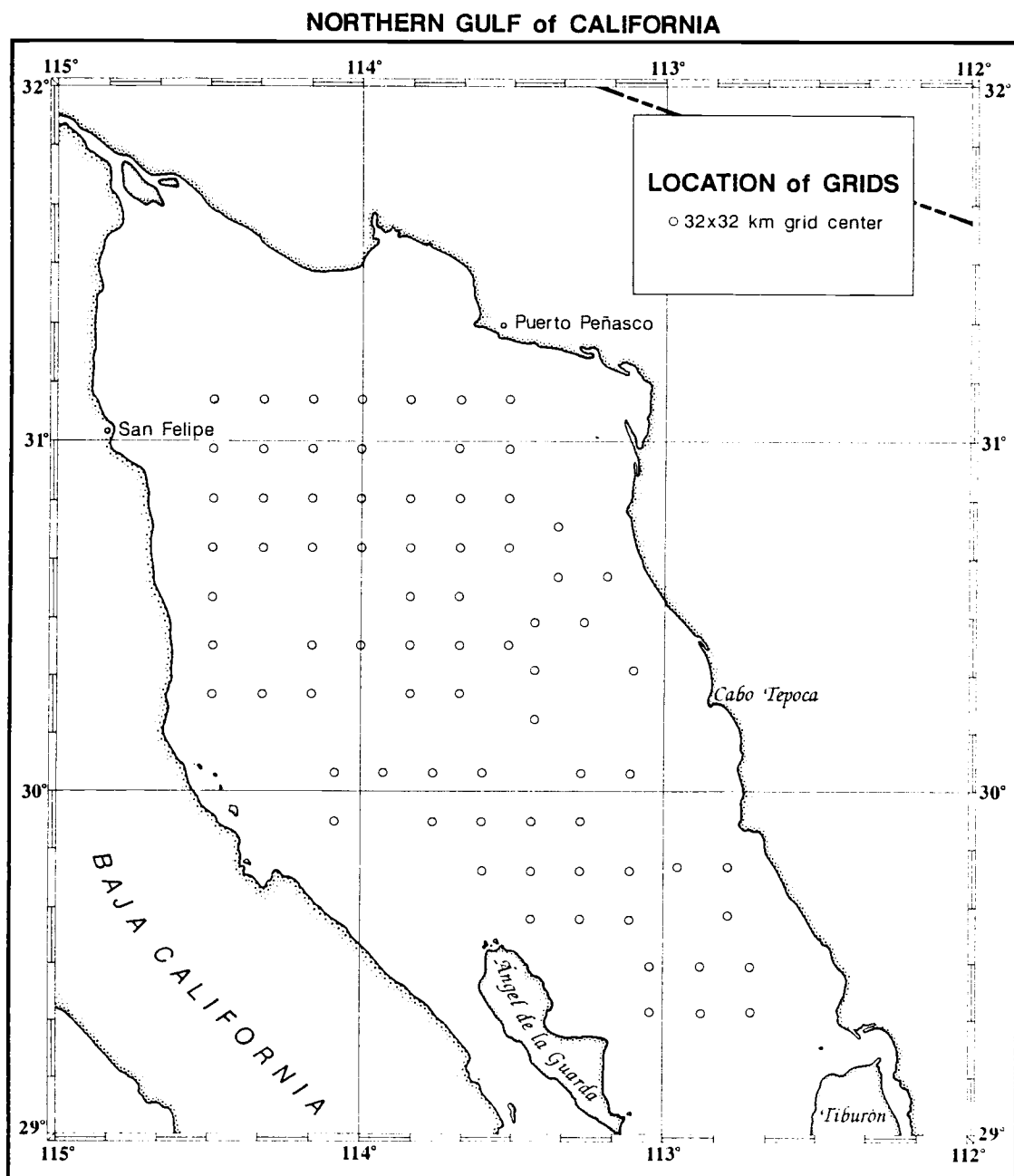


Figure 20. Location of centers of the 32 km by 32 km grids.

| |
|-----------------------------|
| N11 N12 N13 N22 N31 N32 N33 |
| N14 N15 N16 N25 N34 N35 N36 |
| N17 N18 N19 N28 N37 N38 N39 |
| N44 N45 N46 N55 N64 N65 N66 |
| N71 N72 N73 N82 N91 N92 N93 |
| N74 N75 N76 N85 N94 N95 N96 |
| N77 N78 N79 N88 N97 N98 N99 |

Figure 21. Names of subgrids 32 km by 32 km used in the 2DMEM. The names are given according to their relative location in the 64 km by 64 km subgrids.

4 is a compilation of the depths obtained. The average depth to the top of the magnetic source determined with the 2DMEM is 5.0 km below sea level.

Figure 22 is a contour map of the depth to the top of the magnetic source obtained using the 2DMEM. The map is contoured at 1 km intervals. It shows features and depths which are similar to the mapped intermediate depth results of the 2DFFT technique discussed in the previous chapter (figure 13). Using 2DMEM for increased horizontal spatial resolution, the new map covers a bigger area (I can analyze closer to the edges of the data) and it shows more character. In particular, in the area north of Isla Angel de la Guarda, the 6 km deep minimum appears on this map in almost the same fashion as on the previous map, but here it shows a region in the center that reaches depths of up to 8 km below sea level. East of Isla Angel de la Guarda, a new feature which was not noticeable on the previous map shows very strongly as a minimum, 5 km deep, oriented NE. The northern part of the new map is slightly different from the 2DFFT map of the intermediate source. It shows an area of shallow depths, around 4 km, which is not present in the intermediate source map. A possible explanation for why they did not appear on the previous map is that they were averaged over a larger region. In this second map they were better localized. Alternatively, it is possible that the power spectrum estimate did not clearly resolve all frequencies, and that the depths so determined were mixed with the depths of the shallow magnetic horizon.

Table 4. Depths to the magnetic source using the 2DMEM for 32 by 32 km grids. Spacing between points is 16 km.

| Grid | Depth (km below sea level) | Grid | Depth (km below sea level) |
|------|-------------------------------|------|-------------------------------|
| N11 | 4.1 | N96 | 5.8 |
| N12 | 5.2 | N97 | 4.7 |
| N13 | 5.8 | N98 | 5.5 |
| N14 | 6.0 | NE2 | 5.9 |
| N15 | 6.6 | NE5 | 4.2 |
| N16 | 5.3 | NE6 | 4.4 |
| N17 | 5.6 | C31 | 5.1 |
| N18 | 4.1 | C32 | 4.7 |
| N19 | 3.8 | C34 | 5.9 |
| N22 | 3.8 | C36 | 5.5 |
| N25 | 5.9 | C37 | 6.8 |
| N28 | 5.2 | C44 | 6.1 |
| N31 | 5.2 | C45 | 4.7 |
| N32 | 4.5 | C46 | 5.6 |
| N33 | 3.5 | C55 | 5.8 |
| N35 | 4.5 | C65 | 5.3 |
| N36 | 3.9 | C66 | 5.0 |
| N37 | 6.1 | C71 | 3.8 |
| N38 | 5.3 | C73 | 6.0 |
| N39 | 4.1 | C82 | 8.3 |
| N44 | 6.2 | C85 | 6.7 |
| N45 | 4.0 | C91 | 6.2 |
| N46 | 4.1 | C92 | 6.2 |
| N55 | 3.4 | C94 | 5.5 |
| N64 | 4.7 | C95 | 5.5 |
| N65 | 4.9 | C96 | 3.9 |
| N66 | 5.5 | C97 | 4.0 |
| N71 | 5.7 | C98 | 4.4 |
| N74 | 6.1 | C99 | 3.1 |
| N76 | 4.1 | SC2 | 3.9 |
| N77 | 5.0 | SC3 | 5.9 |
| N78 | 5.3 | SC6 | 5.8 |
| N79 | 4.1 | SE1 | 5.1 |
| N85 | 3.8 | SE2 | 4.5 |
| N91 | 3.5 | SE3 | 4.4 |
| N92 | 5.3 | SE4 | 4.5 |
| N94 | 4.3 | SE5 | 3.4 |
| N95 | 4.6 | SE6 | 3.0 |

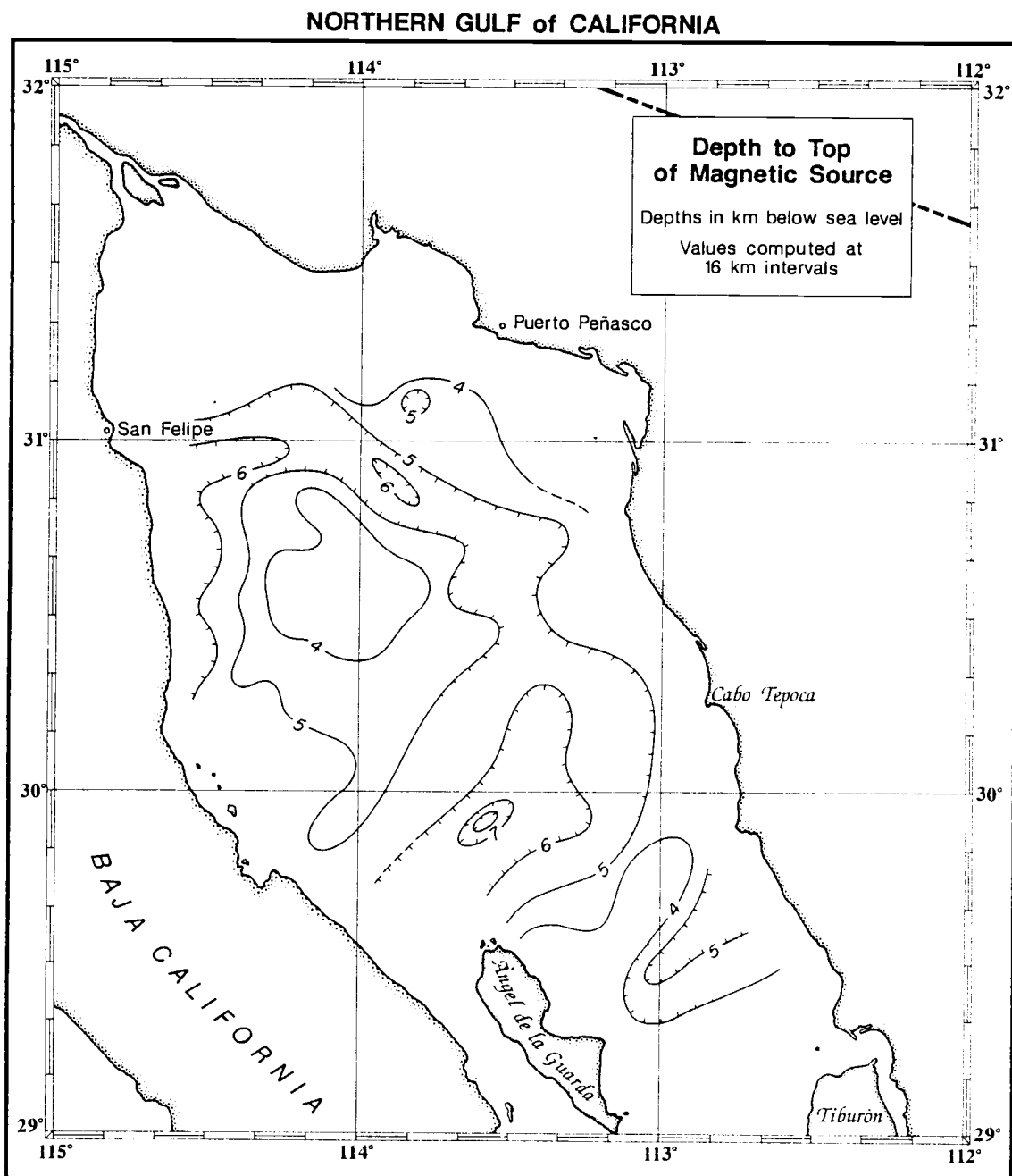


Figure 22. Depth to the top of the magnetic source using 2DMEM.

Using a 0.5 km sample spacing, and with the limitation of a 2^n algorithm, I saw no point in trying to resolve smaller basement structural features by using grids smaller than 32 by 32 km. In this analysis, it is not clear whether a basement pattern of transform faults connected by extension axes is well developed beneath the sediments of the northern Gulf or not. Some of the features I see in this map are consistent with such a tectonic setting, but there are others which seem to complicate the pattern, having slightly different orientations or even orientations completely opposite to expected orientations.

The 8 km depression in the magnetic source is not obvious in the mapped gravity or magnetic anomalies. This could mean that a material with different magnetic properties is present, configured in some way that it has no obvious surface expression. Alternatively, it is possible that what the spectrum is seeing is a lack of data rather than deep sources.

By looking at the radial plots obtained with the 2DMEM, it is obvious that this magnetic horizon is the most distinctive source that the method is capable of identifying. I did not attempt to determine depths to the shallow magnetic horizon using 2DMEM because the variance of the spectra in the frequencies of interest was higher. Depths so obtained would be of doubtful quality.

CONCLUSIONS

This research was intended to help resolve basement depths and structures beneath the sediments of the northern Gulf of California by using spectral analysis methods on marine magnetic anomaly data. I first used a two-dimensional fast fourier transform method (2DFFT) but could obtain depths to the magnetic sources at surface points separated by not less than 32 km. I then tried to obtain a closer spacing using the high resolution method 2DMEM. This method provided depth determinations every 16 km. This provided about a four-fold increase in the surface spatial density of the determinations. But, there is a trade off. I did not obtain clear depths to all of the horizons obtained using the 2DFFT. Nor was it possible to obtain depth to the bottom of the magnetic sources using the 2DMEM.

The results can be summarized as follows:

Using 2DFFT I obtained estimates of the top of magnetic sources at three different depths. The shallow depth magnetic horizon (Figure 11) probably corresponds to the top of the magnetic basement. The lineations observed in the contour map only coincide slightly with the expected structural pattern, but there are some indications of structures with somewhat different characteristics than thought.

The intermediate source (Figure 13) shows lineations which roughly parallel the orientation of proposed spreading centers, although they extend farther northeast to areas not considered

before. Again, some features of this magnetic horizon may correspond to the expected pattern.

The deepest source is not very well controlled. This source may not exist at some locations.

The depth to the bottom of the magnetized crust, interpreted here as the Curie-point isotherm, produces a model of heat flow in the area which agrees very well with observed heat flow data. The calculations show that high heat flow exists in a broad area.

My attempt to improve the 2DFFT results lead to the use of a high resolution method to obtain the power spectra of the magnetic anomalies, the 2DMEM. The results (figure 22) show that I was able to better resolve the depth to the intermediate depth magnetic source. The trends observed in the contour map obtained using the conventional approach were better resolved on the 2DMEM and the area of coverage was more extensive.

BIBLIOGRAPHY

- Andersen, N., 74, On the Calculation of Filter Coefficients for Maximum Entropy Spectral Analysis, Geophysics, 39, 69-72.
- Akaike, H., 69, Fitting Autoregressive Models for Prediction, Ann. Inst. Statist. Math., 21, 243-247.
- Bhattacharyya, B. K., and L. Leu, 75, Analysis of Magnetic Anomalies Over Yellowstone National Park: Mapping of Curie Point Isothermal Surface for Geothermal Reconnaissance, J. Geophys. Res., 80, 4461-4465.
- Biehler, S., R.L. Kovach, and C.R. Allen, 64, Geophysical Framework of the Northern End of the Gulf of California Structural Province, In: Marine Geology of the Gulf of California, T. H. van Andel and George G. Shor (eds), Tulsa, AAPG Memoir, 3, 126-143.
- Bischoff, J. L., and J. W. Niemitz, 80, Bathymetric Maps of The Gulf of California, Miscellaneous Investigations Series, U. S. Geological Survey.
- Blakely, R. J., and S. Hassanzadeh, 81, Estimation of Depth to Magnetic Source Using Maximum Entropy Power Spectra, with Application to the Peru-Chile Trench, G.S.A. Memoir, 154, 667-681.
- Blakely, R. J., 88, Curie-Temperature Isotherm Analysis and Tectonic Implications of Aeromagnetic Data from Nevada, (accepted for publication), J. Geophys. Res.
- Boler, F. M., 78, Aeromagnetic Measurements, Magnetic Source Depths, and the Curie Point Isotherm in the Vale-Owyhee, Oregon, M. S. Thesis, Oregon State University. Corvallis, Oregon.
- Briggs, I. C., 74, Machine Contouring Using Minimum Curvature, Geophysics, 39, 39-48.
- Burg, J. P., 67, Maximum Entropy Spectral Analysis, Presented at the 37th Annual International SEG Meeting, Oklahoma City.

- Calderón-Riveroll, G., 78, A Marine Geophysical Study of Vizcaíno Bay and the Continental Margin of Western México Between 27° and 30° N Latitude, Ph.D. Thesis, Oregon State University. Corvallis, Oregon. 178 p.
- Capon, J., 73, Signal Processing and Frequency-Wavenumber Spectrum Analysis for a Large Aperture Seismic Array, in: Methods in Computational Physics, Bruce A. Bolt (Ed.), 13, 1-59.
- Carter, D. J. T., 80, Echo-Sounding Correction Tables, Third ed., Published by the Hydrographic Department, Ministry of Defense, Taunton, Somerset, England.
- Chen, W. Y., and G. R. Stegen, 74, Experiments with Maximum Entropy Power Spectra Sinusoids, J. Geophys. Res., 79, 3019-3022.
- Connard, G. G., 79, Analysis of Aeromagnetic Measurements from the Central Oregon Cascades, M. S. Thesis, Oregon State University. Corvallis, Oregon. 101 p.
- Connard, G. G. , R. W. Couch, and M. Gemperle, 83, Analysis of Aeromagnetic Measurements from the Cascade Range in Central Oregon, Geophysics, 48, 376-390.
- Couch, R. W., O. Sánchez Z., P. Doguin, T. L. Plawman, G. Calderón R., S. P. Coperude, and B. Huen, 88, Geophysical Sections of the Gulf and Peninsular Province of the Californias, In: The Gulf and Peninsular Province of the Californias, J. P. Dauphin (ed), AAPG Memoir (in preparation), Tulsa.
- Doguin, P., 88, Crustal Structure of the Northern Gulf of California from Geophysical Modeling and Deconvolution of Magnetic Profiles, M. S. Thesis (in preparation), Oregon State University. Corvallis, Oregon.
- Edward, J. A., and M. M. Fitelson, 73, Notes on Maximum-Entropy Processing, IEEE Trans. Inform. Theory, 232-234.
- Elders, W. A., R. W. Rex, T. Meidav, P. T. Robinson, and S. Biehler, 72, Crustal Spreading in Southern California, Science, 178, 15-24.

- Foote, R. W., 85, Curie-Point Isotherm Mapping and Interpretation from Aeromagnetic Measurements in the Northern Oregon Cascades, M. S. Thesis, Oregon State University, Corvallis, Oregon. 115 p.
- Frost, B. R., and P. N. Shive, 86, Magnetic Mineralogy of the Lower Continental Crust, J. Geophys. Res., 91, 6513-6521.
- Galbraith, J. N., 71, Prediction Error As a Criterion for Operator Length, Geophysics, 36, 261-265.
- Gastil, R. G., R. P. Phillips, and E. C. Allison, 75, Reconnaissance Geology of the State of Baja California, GSA Memoir, 140, 170 p.
- Haggerty, S. E., 78, Mineralogical Constraints on Curie Isotherms in Deep Crustal Magnetic Anomalies, Geophys. Res. Lett., 5, 105-108.
- Heney, T. L., and J. L. Bischoff, 73, Tectonic Elements of the Northern Part of the Gulf of California, GSA Bull., 84, 315-330.
- Huppunen, J. L., 83, Analysis and Interpretation of Magnetic Anomalies Observed in North Central California, Ph. D. Thesis, Oregon State University, Corvallis, Oregon. 248 p.
- International Association of Geodesy, 71, Geodetic Reference System 1967, Bulletin of Geodesy Special Publication, No. 3, 116 p.
- International Association of Geomagnetism and Aeronomy, 82, International Geomagnetic Reference Field 1980, Report, Geophysics, 47, 841-842.
- Justice, J. H., 81, The Step From One to Higher Dimensional Signal Processing— Case Histories, in: Applied Time Series Analysis II, 2, 21-70.
- Kanasewich, E. R., 81, Time Sequence Analysis in Geophysics, The University of Alberta Press, Edmonton, Alberta, Canada, 480 p.
- Clitgord, K. D., J. D. Mudie, J. L. Bischoff, and T. L. Heney, 74, Magnetic Anomalies in the Northern and Central Gulf of California, GSA Bull., 85, 815-820.

- Kovach, R. L., C. R. Allen, and F. Press, 62, Geophysical Investigations in the Colorado Delta Region, J. Geophys. Res., 67, 2845-2871.
- Krummenacher, D., R.G. Gastil, J. Bushee, and J. Doumont, 75, K. Ar. Apparent Ages Peninsular Ranges Batholith Southern California and Baja California., GSA Bull., 86:760-768.
- Lachenbruch, A. H., J. H. Sass, and S. P. Galanis Jr., 85, Heat Flow in the Southernmost California and the Origin of the Salton Trough, J. Geophys. Res., 90, 6709-6736.
- Lacoss, R. T., 71, Data Adaptive Spectral Analysis Methods, Geophysics, 36, 661-675.
- Larson, P. A., J. D. Mudie, and R. L. Larson, 72, Magnetic Anomalies and Fracture-Zone Trends in the Gulf of California, GSA Bull., 83, 3361-3368.
- Levi, S., and R. Riddihough, 86, Why are Marine Magnetic Anomalies Suppressed over Sedimented Spreading Centers?, Geology, 14, 651-654.
- Lim, J. S., and N. A. Malik, 81, A New Algorithm for Two-Dimensional Maximum Entropy Power Spectrum Estimation, IEEE Transactions on Acoustics, Speech, and Signal Processing, 29, 401-413.
- Lomnitz, C., F. Mooser, C. R. Allen, J. N. Brune, and W. Thatcher, 70, Seismicity and Tectonics of the Northern Gulf of California Region, México, Geofísica Internacional, 10, 37-48.
- Lonsdale, P., 85, A Transform Continental Margin Rich in Hydrocarbons, Gulf of California, AAPG Bull., 69, 1160-1180.
- Matthews, D. J., 39, Tables of the Velocity of Sound in Pure Water and Sea Water for Use in Echosounding and Sound Ranging, Publ. H.D.282, Admiralty Hydrogr. Dept., London.
- McLain, W. H., 81, Geothermal and Structural Implications of Magnetic Anomalies Observed Over the Southern Oregon Cascade Mountains and Adjoining Basin and Range Province, unpublished M.S. Thesis, Oregon State University. Corvallis, Oregon, 101 p.

- Mishra, D. C., and P. S. Naidu, 74, Two-Dimensional Power Spectral Analysis of Aeromagnetic Fields, Geophysical Prospecting, 22, 345-353.
- Moore, D. G., and E. C. Buffington, 68, Transform Faulting and Growth of the Gulf of California Since the Late Pliocene, Science, 161, 1238-1241.
- Morgan, P., 82, Heat Flow in Rift Zones, in: Continental and Oceanic Rifts, G. Pálmason (Ed.), Geodynamics Series, AGU, GSA, 8, 107-122.
- Ness, G. E., and M. Lyle, 88, Seismo-Tectonics of the Gulf and Peninsular Province of the Californias, In: The Gulf and Peninsular Province of the Californias, J. P. Dauphin (ed), AAPG Memoir (in preparation), Tulsa.
- Ness, G. E., O. Sánchez Z., R. W. Couch, and R. S. Yeats, 81, Bathymetry and Oceanic Crustal Ages in the Vicinity of the Mouth of the Gulf of California, Illustrated Using Deep Sea Drilling Project Leg 63 Underway Geophysical Profiles, Initial Reports of the Deep Sea Drilling Project, 63, 919-923.
- Newman, W. I., 77, A New Method of Multidimensional Power Spectral Analysis, Astronomy and Astrophysics, 54, 369-380.
- Nobes, D. C., H. Villinger, E. E. Davis, and L. K. Law, 86, Estimation of Marine Sediment Bulk Physical Properties at Depth from Seafloor Geophysical Measurements., J. Geophys. Res., 91, 14033-14043.
- Pan American Institute of Geography and History, 77, The Latin American Gravity Standardization Net 1977 (LAGSN77), SILAG Working Group of the Geophysics Commission.
- Pendrel, J. V., 77, The Maximum Entropy Principle in Two-Dimensional Spectral Analysis, Ph. D. Thesis, York University. Toronto, Ontario.
- Pérez C., G. A., 82, Evolución Geológica, Interpretación Geofísica y Perspectivas Petroleras de la Provincia San Felipe-Tiburón, Golfo de California, Ingeniería Petrolera, 22, 20-32.

- Phillips, R. P., 64, Seismic Refraction Studies in Gulf of California, in T. H. van Andel, and G. G. Shor, jr., ed., Marine geology of the Gulf of California: Tulsa, Oklahoma, AAPG Memoir, 3, 408 p.
- Roucos, S. E., and D. G. Childers, 80, A Two-Dimensional Maximum Entropy Spectral Estimator, IEEE Transactions on Information Theory, 26, 554-560.
- Rusnak, G. A. and R. L. Fisher, 64, Structural History and Evolution of the Gulf of California, In: Marine Geology of Gulf of California, T. H. van Andel and George G. Shor (eds). Tulsa, AAPG Memoir, 3, 144-156.
- Rusnak, G. A., R. L. Fisher, and F. P. Shepard, 64, Bathymetry and Faults of the Gulf of California, In: Marine Geology of Gulf of California, T.H. van Andel and George G. Shor (eds), Tulsa, AAPG Memoir, 3, 59-75.
- Schlanger, C. M., 85, Magnetization of the Lower Crust and Interpretation of Regional Magnetic Anomalies: Example from Lofoten and Vesterålen, Norway, J. Geophys. Res., 90, 11484-11504.
- Shuey, R. T. , D. K. Schellinger, A. C. Tripp, and L. B. Alley, 77, Curie Depth Determination from Aeromagnetic Spectra, Geophys. J. R. Astr. Soc., 50, 75-101.
- Smith, G. M., and S. K. Banerjee, 86, Magnetic Structure of the Upper Kilometer of the Marine Crust at Deep Sea Drilling Project Hole 504B, Eastern Pacific Ocean, J. Geophys. Res., 91, 10337-10354.
- Spector, A., and F. S. Grant, 70, Statistical Models for Interpreting Aeromagnetic Data, Geophysics, 35, 293-302.
- Stacey, F. D.,77, Physics of the Earth, John Wiley and Sons, New York, N. Y., 2nd ed., 414 p.
- Sumner, J. R., 72, Tectonic Significance of Gravity and Aeromagnetic Investigations at the Head of the Gulf of California, GSA Bull., 83, 3103-3120.

- Sykes, L. R., 68, Seismological Evidence for Transform Faults, Sea-Floor Spreading, and Continental Drift, Princeton University Press. 120-150.
- Sykes, L. R., 70, Earthquake Swarms and Sea-Floor Spreading, J. Geophys. Res., 75, 6598-6611.
- Thatcher, W., and J. N. Brune, 71, Seismic Study of an Oceanic Ridge Earthquake Swarm in the Gulf of California, Royal Astron. Soc. Geophys. Jour., 22, 473-489.
- Ulrych, T. J., and C. J. Walker, 81, High Resolution 2-Dimensional Power Spectral Estimation, in: Applied Time Series Analysis II, 2, 71-99.
- Vine, F. J., 66, Spreading of the Ocean Floor: New Evidence, Science, 154, 1405-1415.
- Wasilewski, P. J., and D. M. Fountain, 82, The Ivrea Zone as a Model for the Distribution of Magnetization in the Continental Crust, Geophys. Res. Lett., 9, 333-336.
- Williams, M., P. N. Shive, D. M. Fountain, and B. R. Frost, 85, Magnetic Properties of Exposed Deep Crustal Rocks from the Superior Province of Manitoba, Earth Planet. Sci. Lett., 76, 176-184.
- Wilson, J. T., 65, A New Class of Faults and their Bearing on Continental Drift, Nature, v. 207, p. 343-347.
- Worzel, J. L., 65, Pendulum Gravity Measurements at Sea 1936-1959, Wiley, New York, 421 p.

APPENDICES

APPENDIX A

Radially Averaged Spectral Plots Using 2DFFT

Figures A1 to A21 are the radial plots of the 21 grids, 64 km by 64 km, used in the calculations of depths to the magnetic sources using the 2DFFT for the power spectrum.

Plots of Theoretical Spectra.- Figures A22-A and A22-B were obtained from equation (1), in Chapter III. Figure A22-A is a collection of curves with a fixed thickness and varying depth to the top. The obvious feature here is the change in slope for different depths. Note also that the location of the maximum shifts towards the lower frequency end, meaning that the depth to the bottom is also increasing. Figure A22-B is a collection of curves with a fixed depth to the top and varying thickness. Here the important feature is the shifting of the maximum towards the lower frequency end with increasing thickness. The slopes of both curves are similar.

Plot of Radially Averaged Power Spectrum for a Grid Appended with zeroes.- Figure A23 is the radial plot of a grid appended with zeroes for the determination of the frequency where the maximum appears.

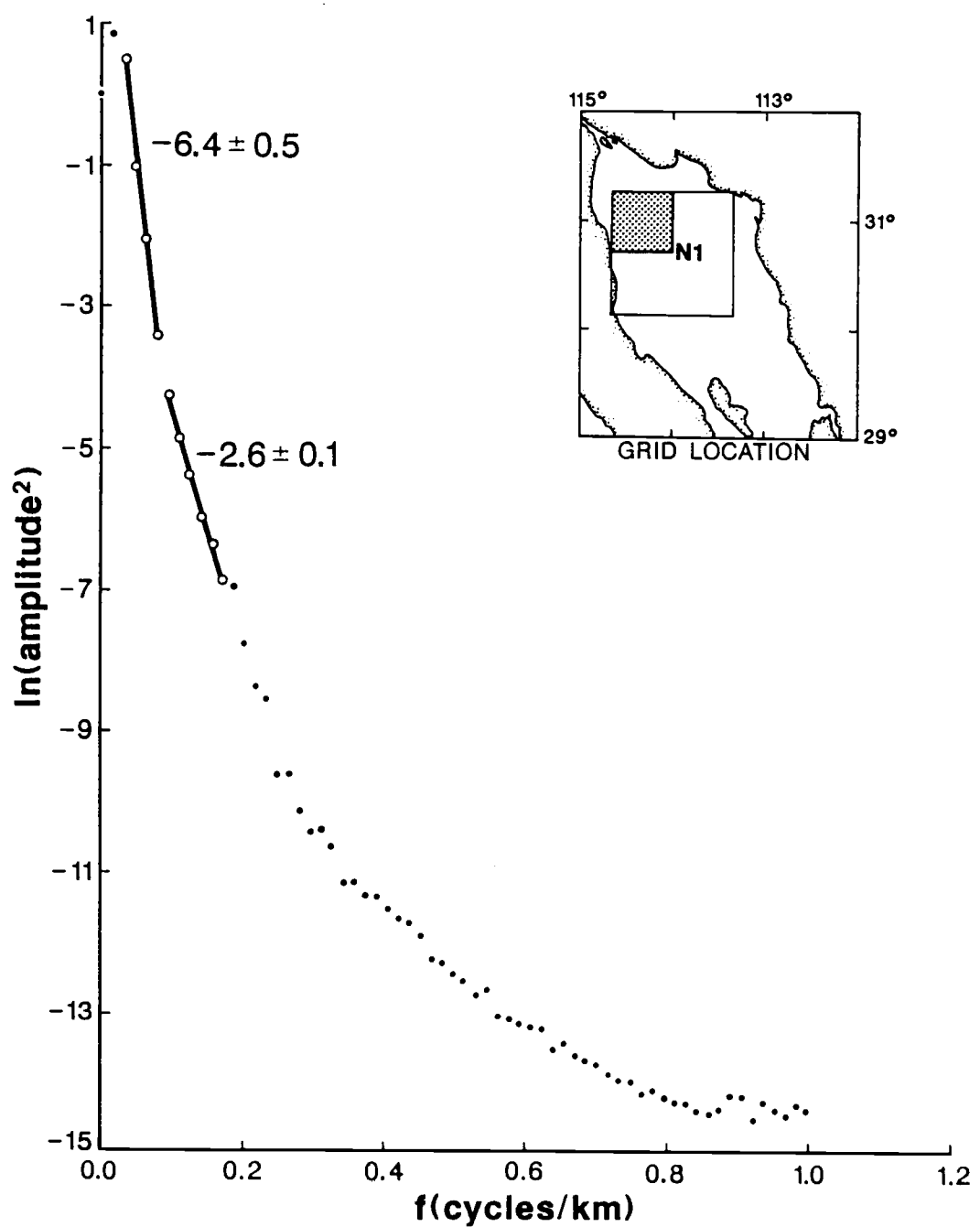


Figure A1. Radially averaged power spectrum of grid N1, using the 2DFFT. See explanation in figure 10.

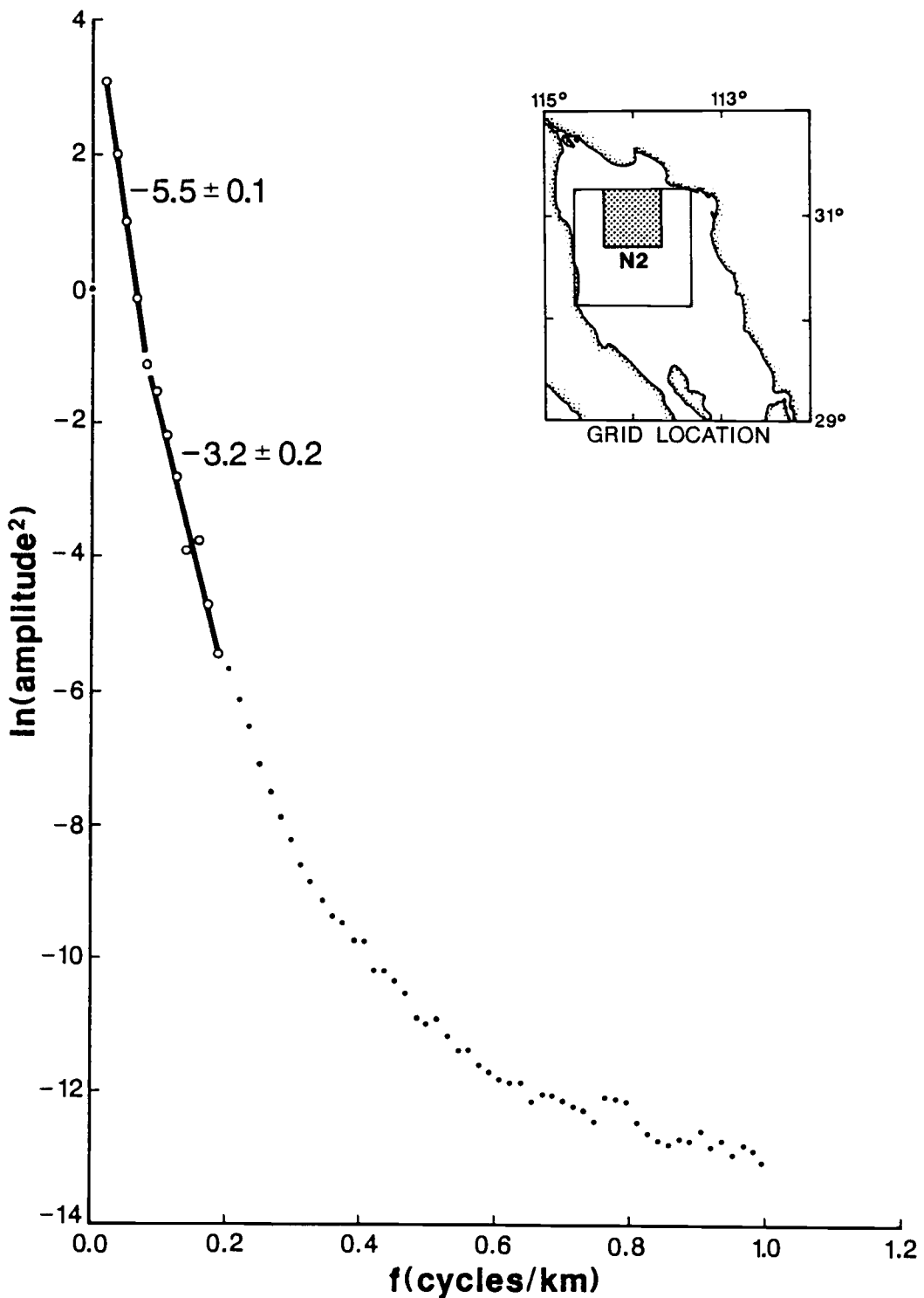


Figure A2. Radially averaged power spectrum of grid N2, using the 2DFFT. See explanation in figure 10.

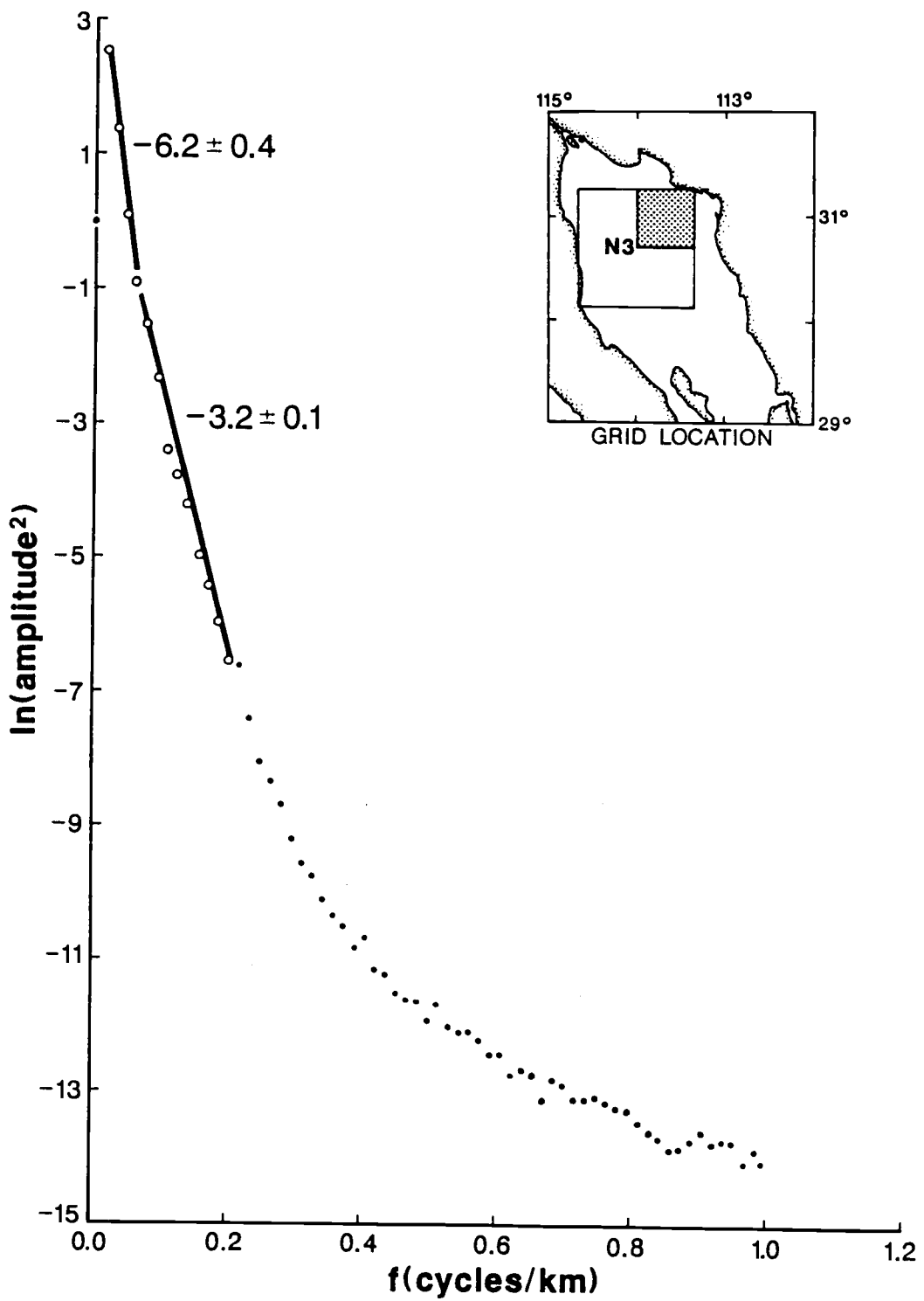


Figure A3. Radially averaged power spectrum of grid N3, using the 2DFFT. See explanation in figure 10.

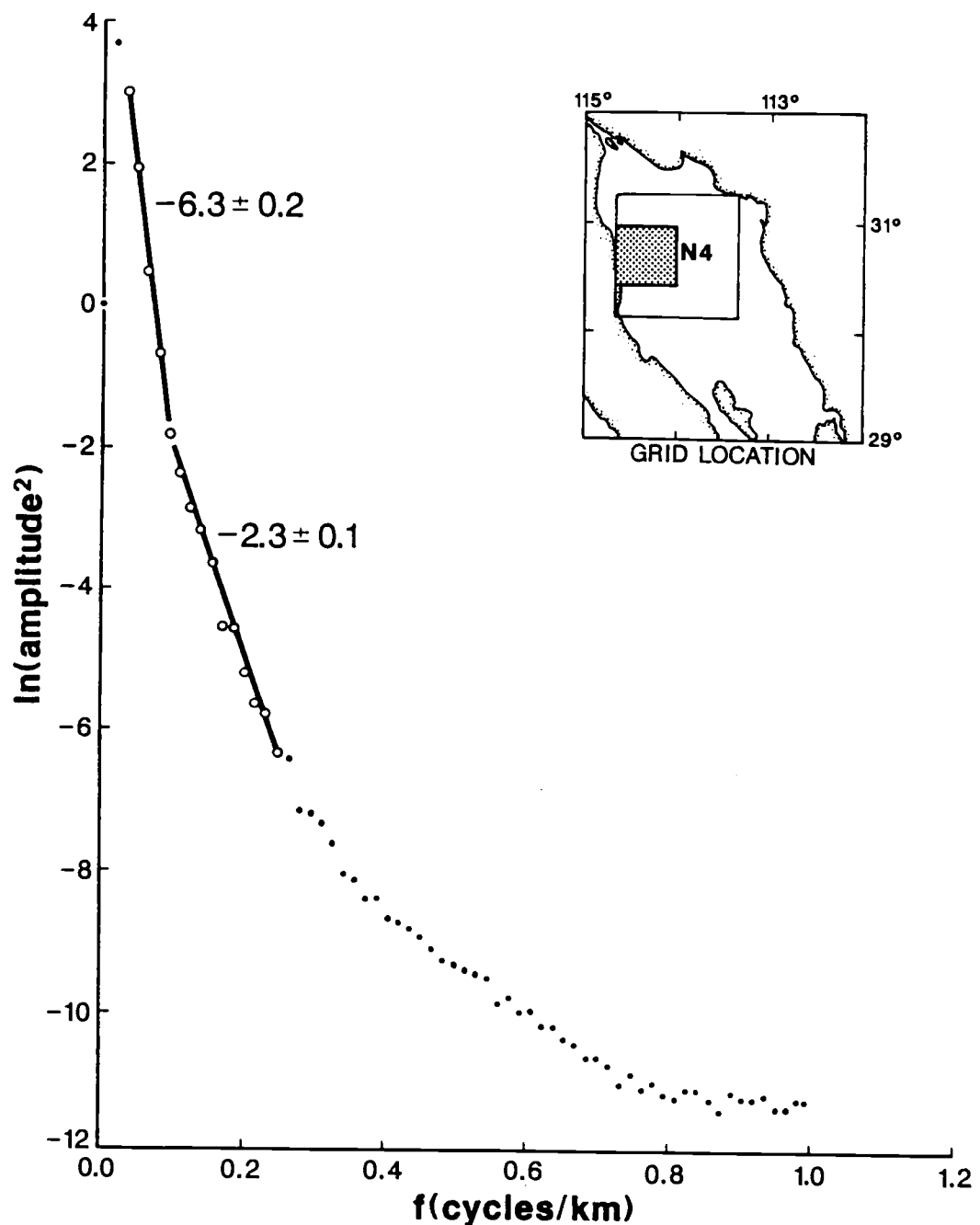


Figure A4. Radially averaged power spectrum of grid N4, using the 2DFFT. See explanation in figure 10.

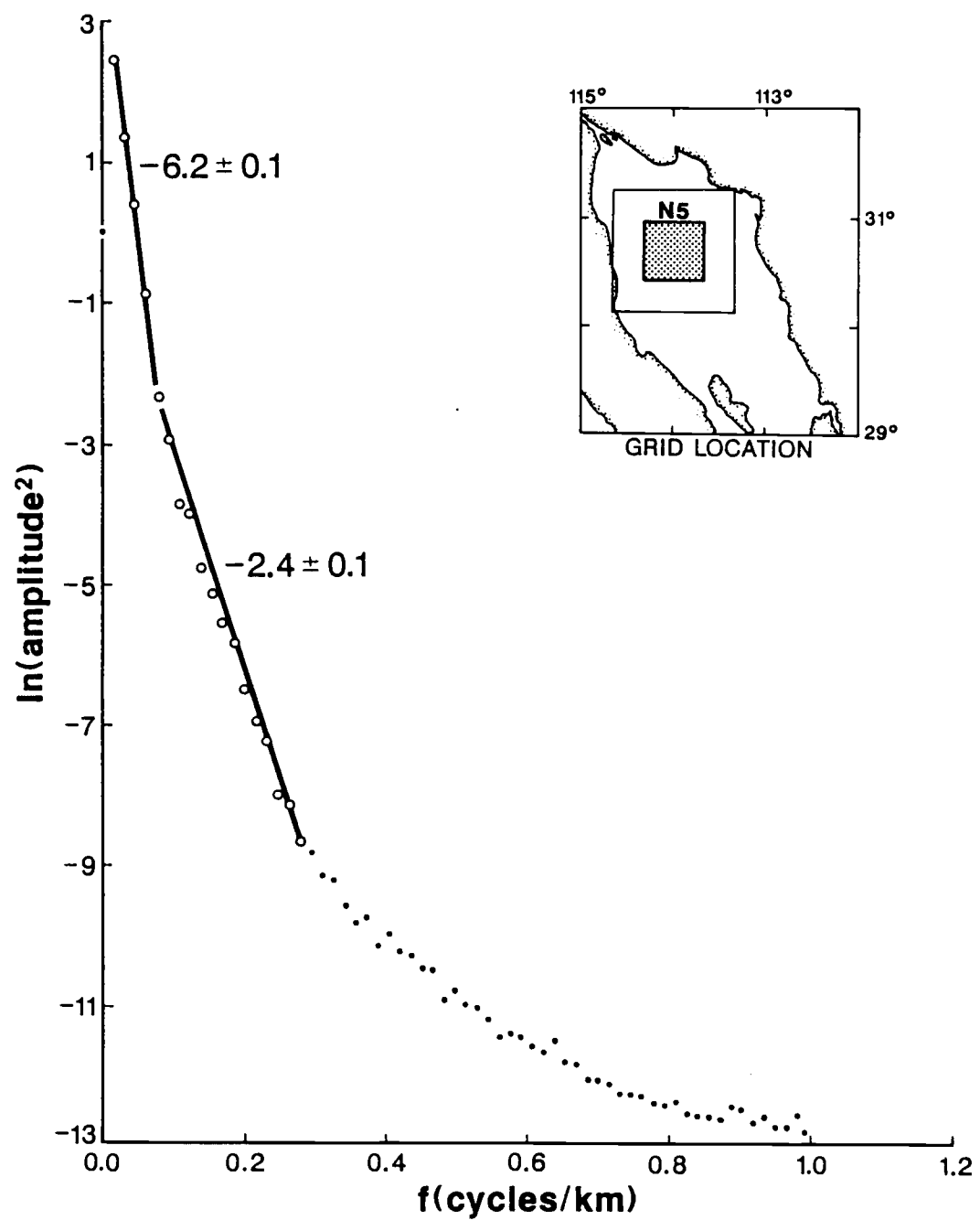


Figure A5. Radially averaged power spectrum of grid N5, using the 2DFFT. See explanation in figure 10.

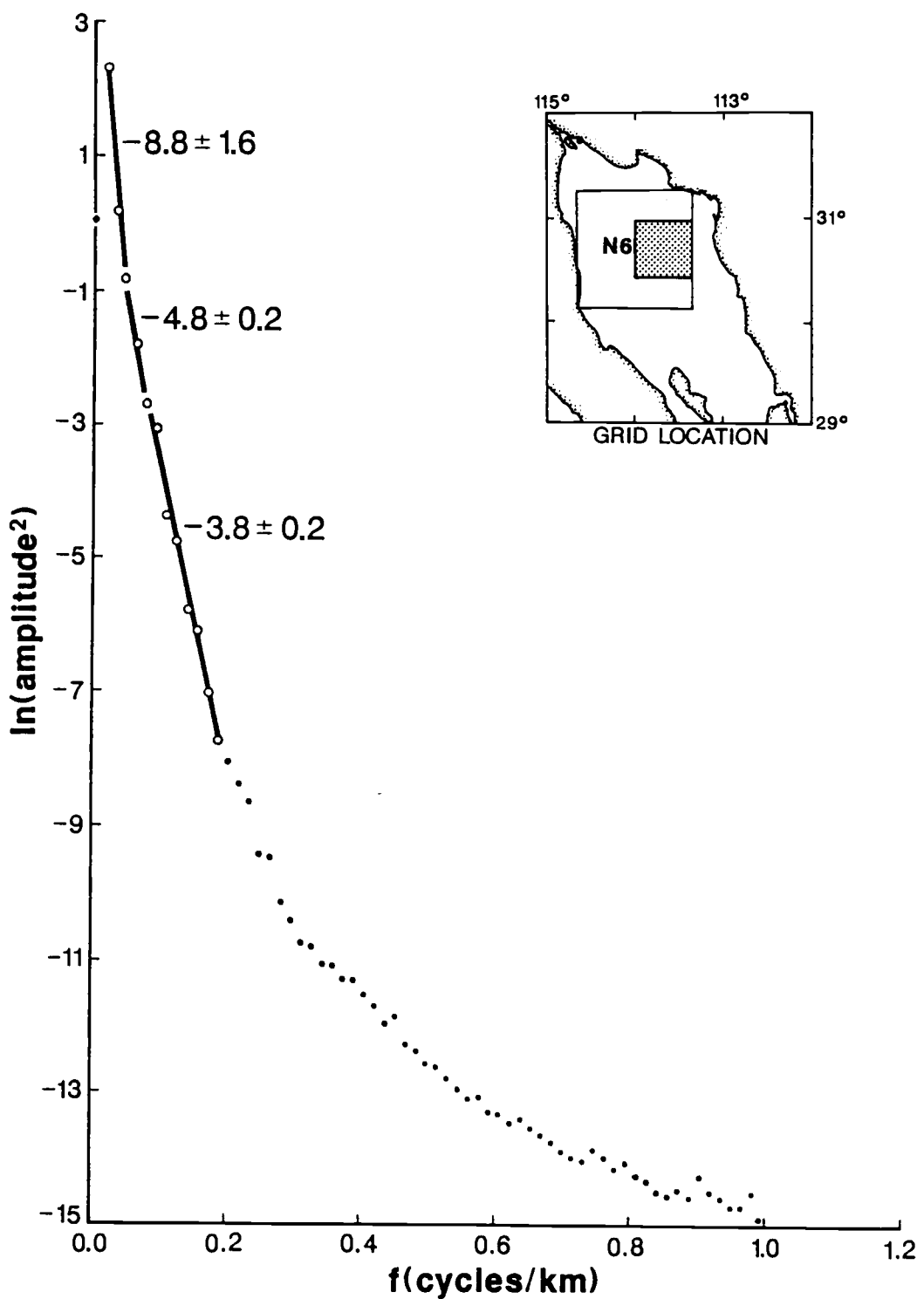


Figure A6. Radially averaged power spectrum of grid N6, using the 2DFFT. See explanation in figure 10.

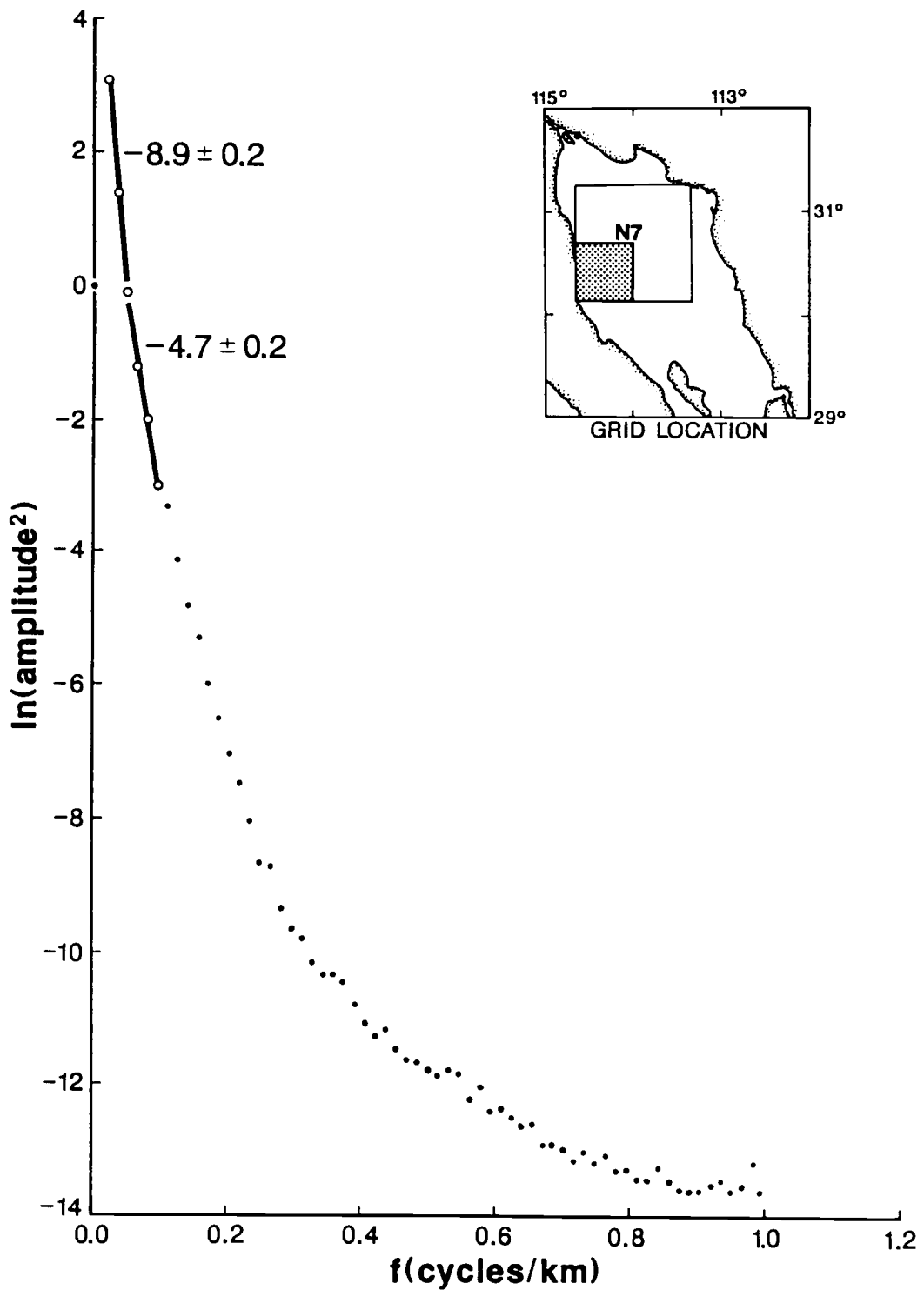


Figure A7. Radially averaged power spectrum of grid N7, using the 2DFFT. See explanation in figure 10.

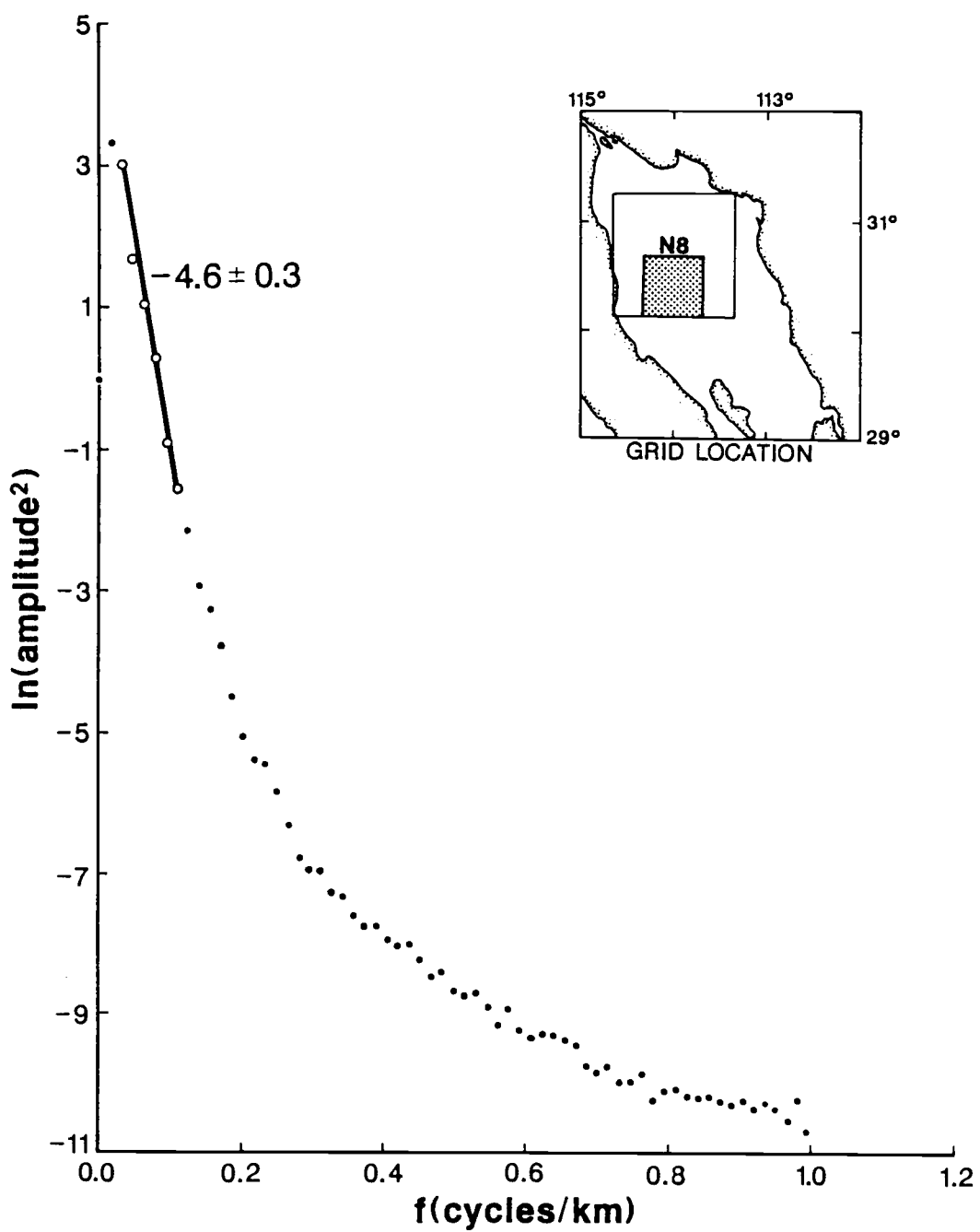


Figure A8. Radially averaged power spectrum of grid N8, using the 2DFFT. See explanation in figure 10.

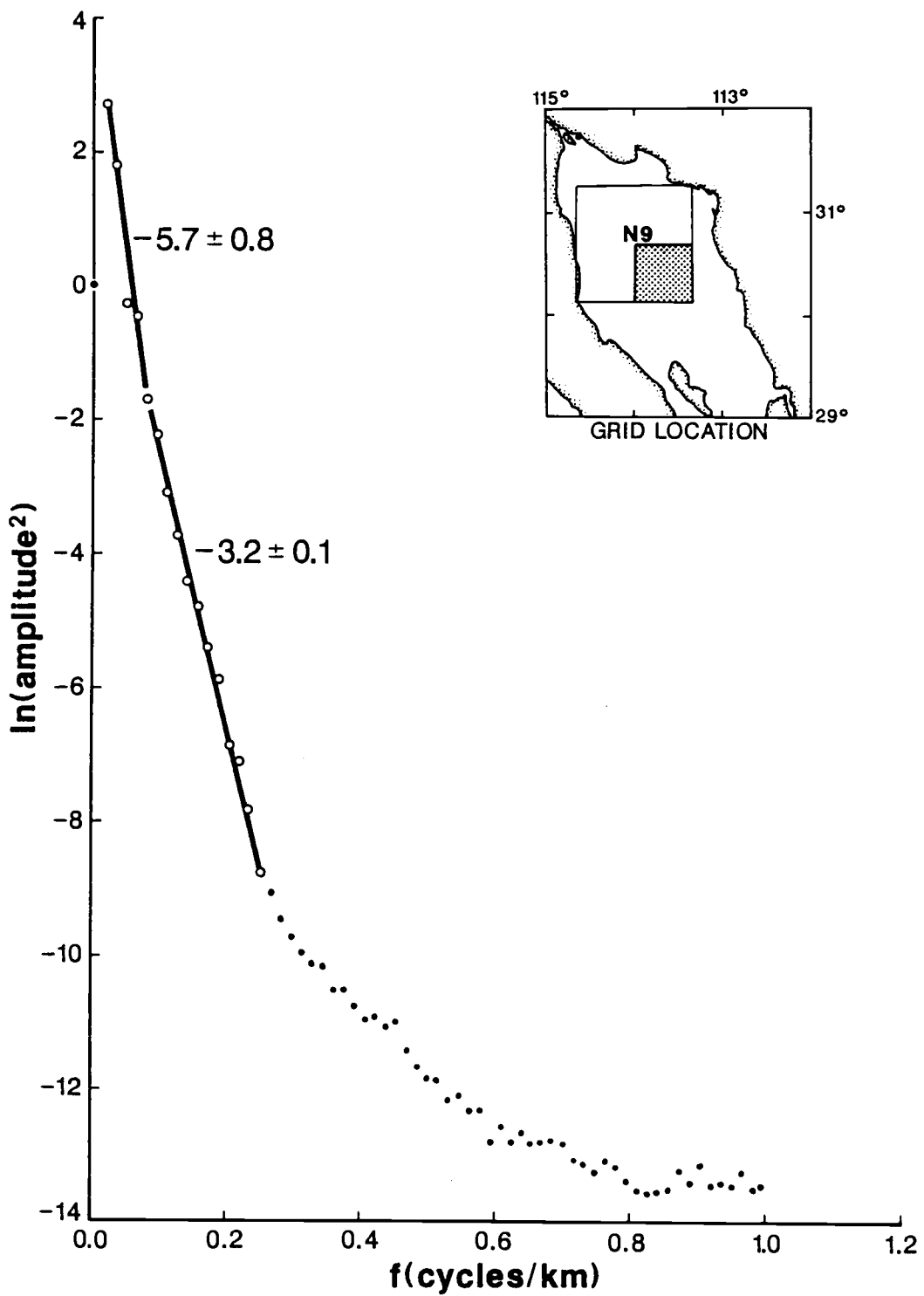


Figure A9. Radially averaged power spectrum of grid N9, using the 2DFFT. See explanation in figure 10.

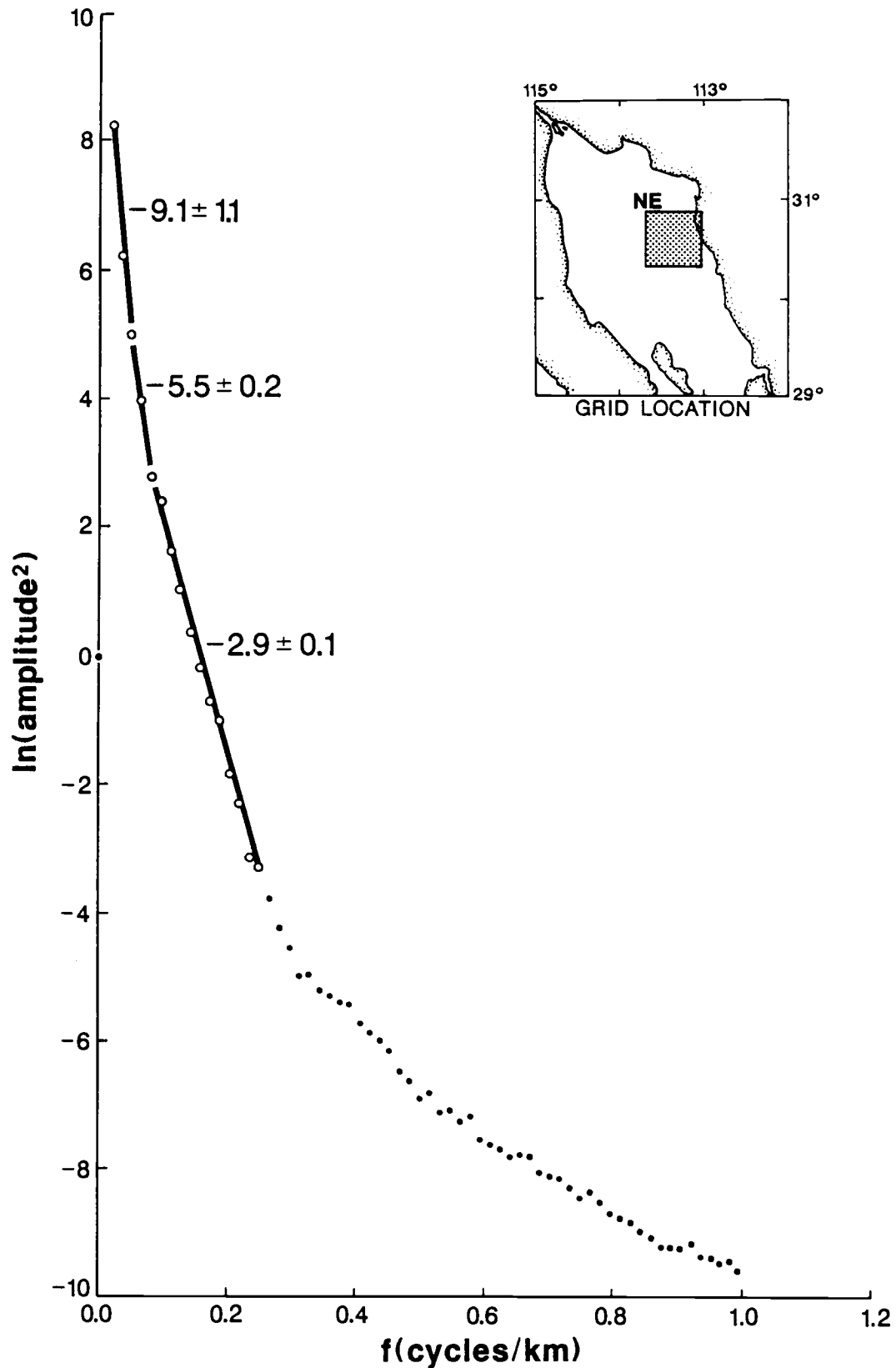


Figure A10. Radially averaged power spectrum of grid NE, using the 2DFFT. See explanation in figure 10.

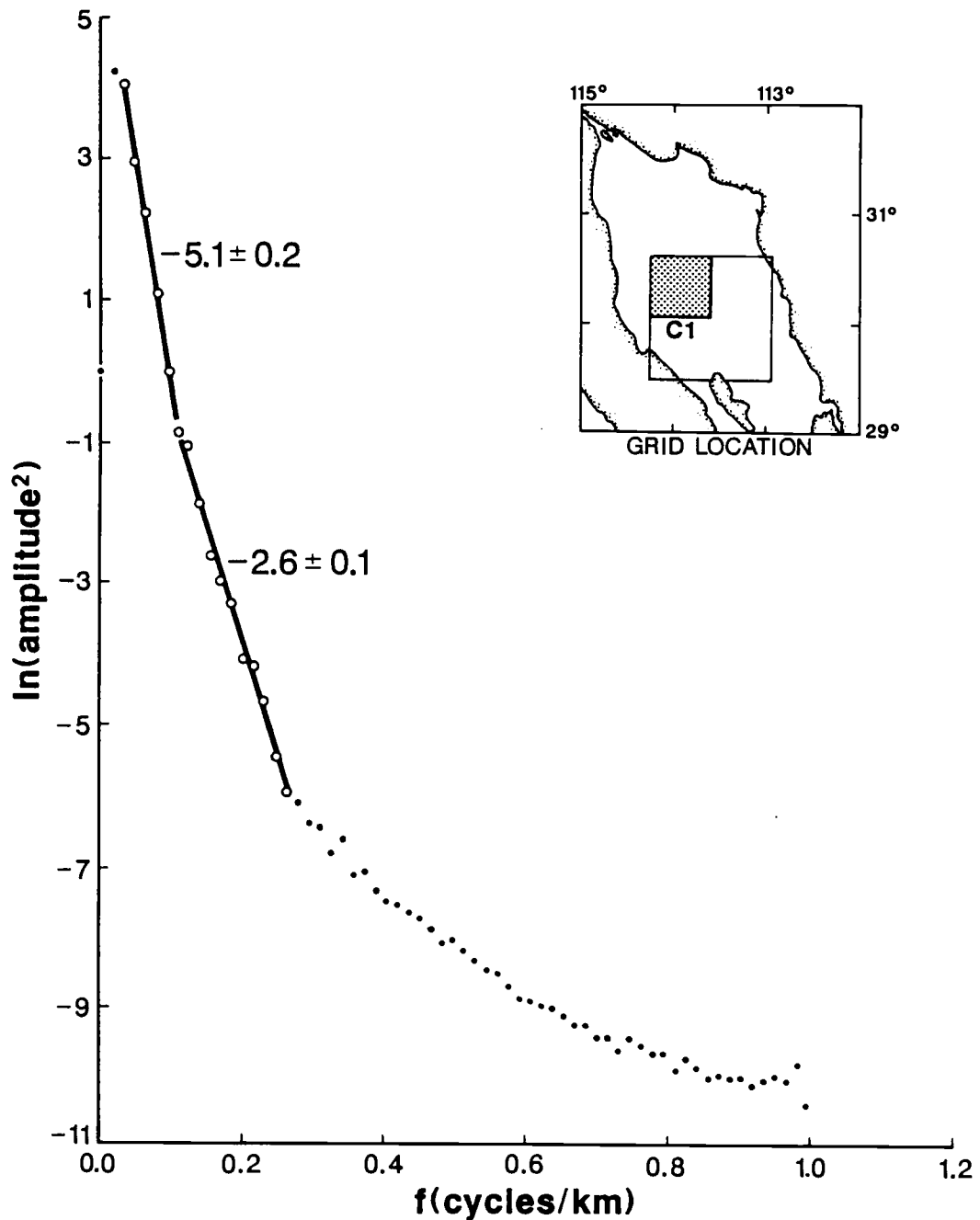


Figure A11. Radially averaged power spectrum of grid C1, using the 2DFFT. See explanation in figure 10.

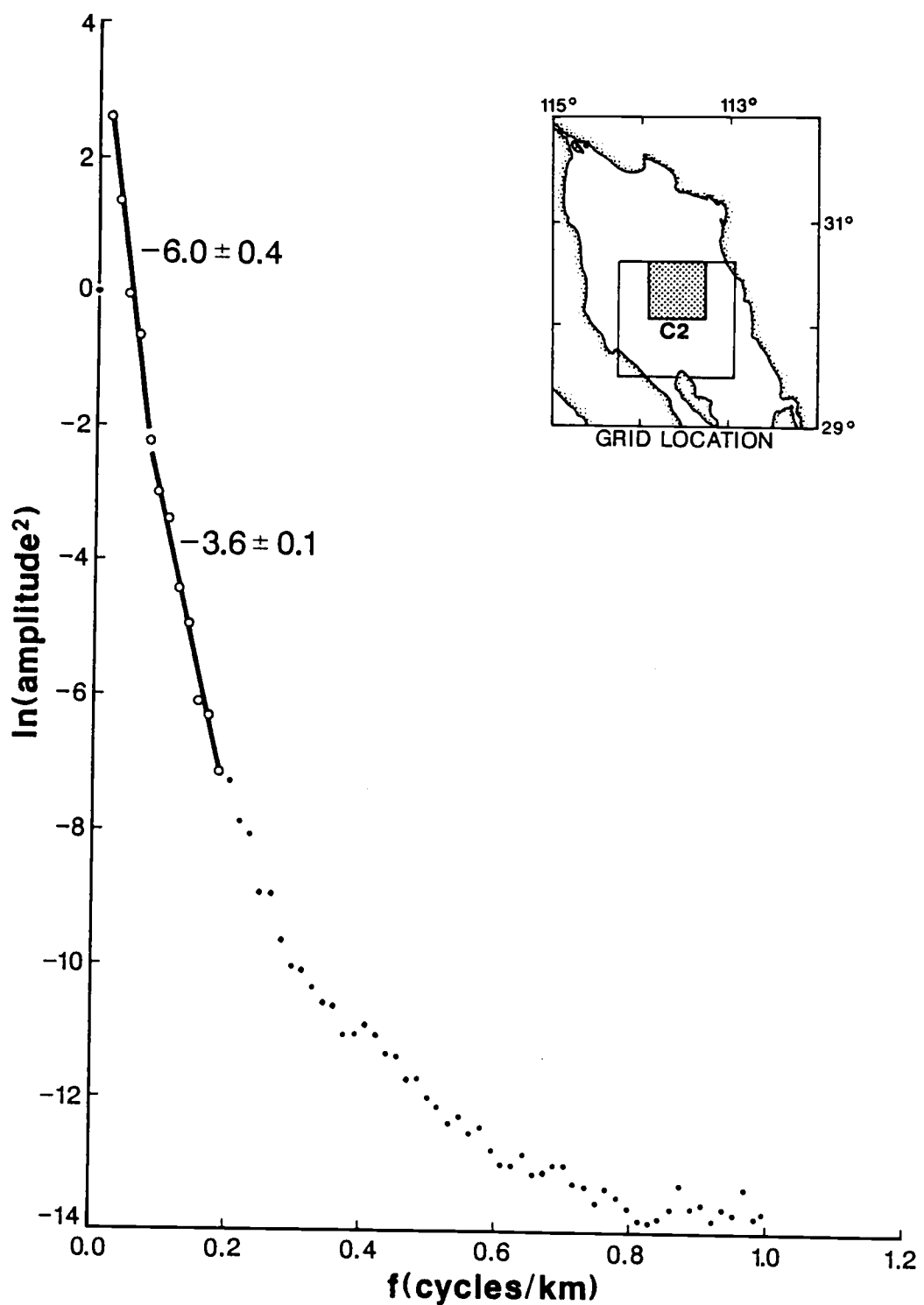


Figure A12. Radially averaged power spectrum of grid C2, using the 2DFFT. See explanation in figure 10.

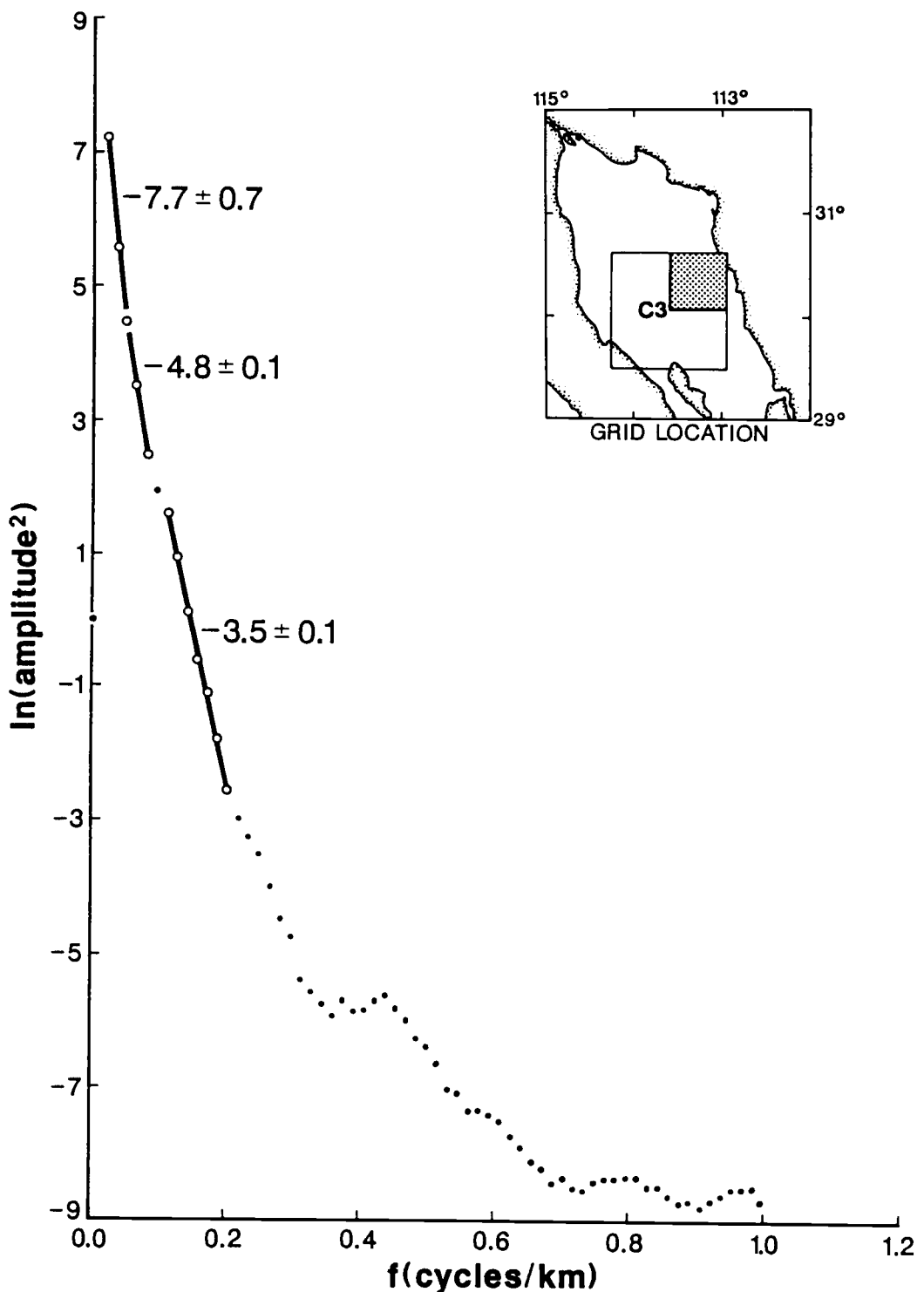


Figure A13. Radially averaged power spectrum of grid C3, using the 2DFFT. See explanation in figure 10.

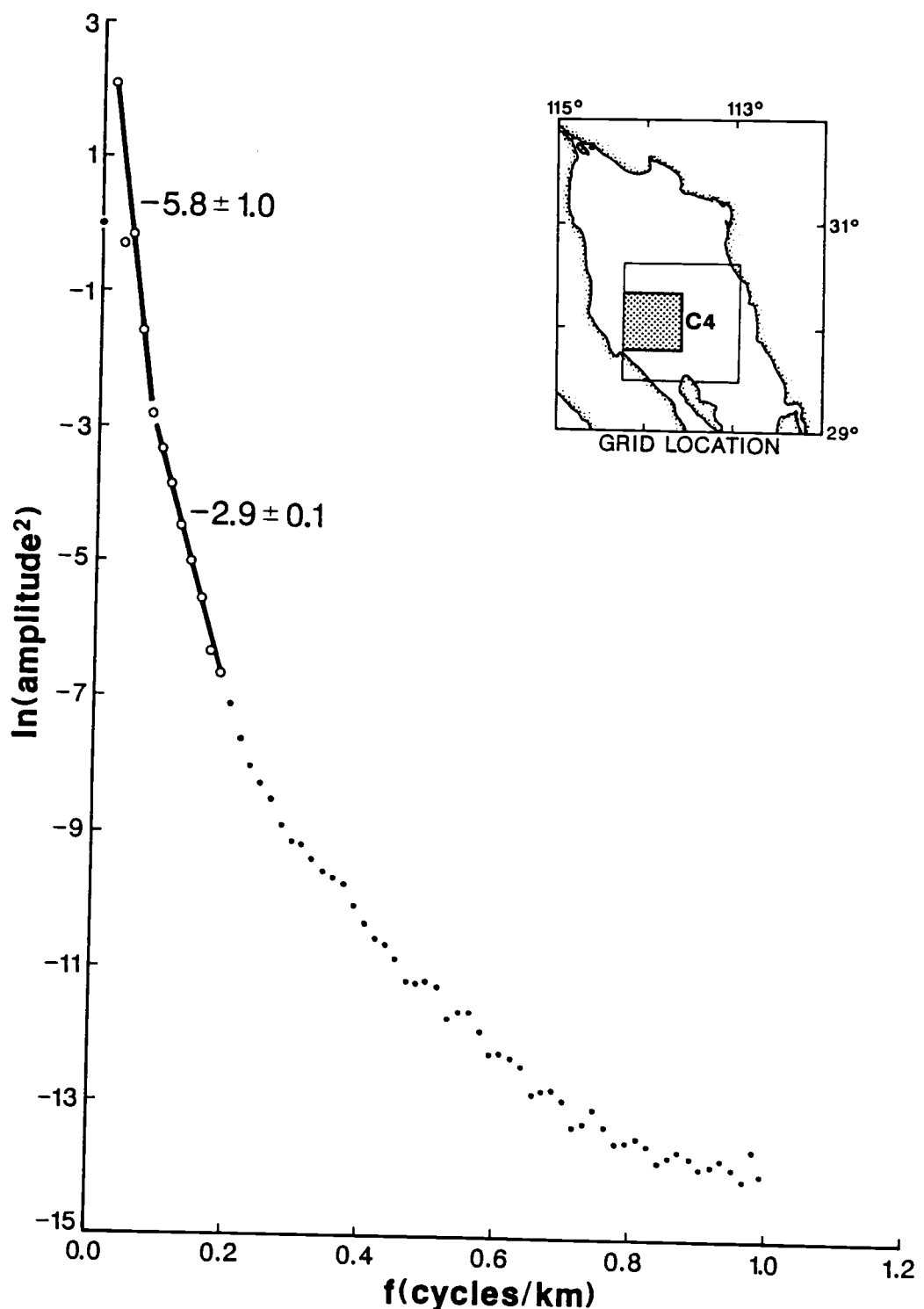


Figure A14. Radially averaged power spectrum of grid C4, using the 2DFFT. See explanation in figure 10.

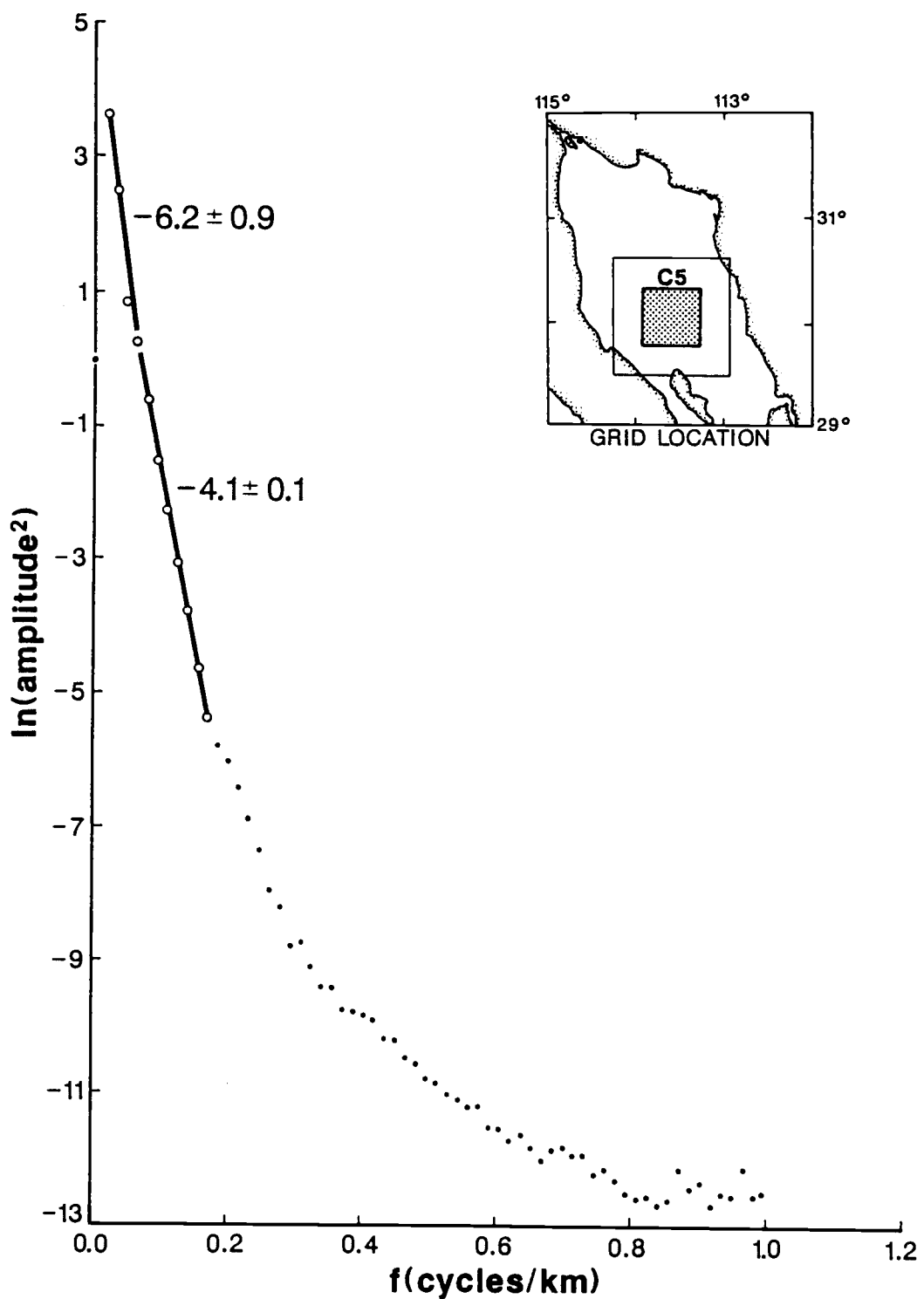


Figure A15. Radially averaged power spectrum of grid C5, using the 2DFFT. See explanation in figure 10.

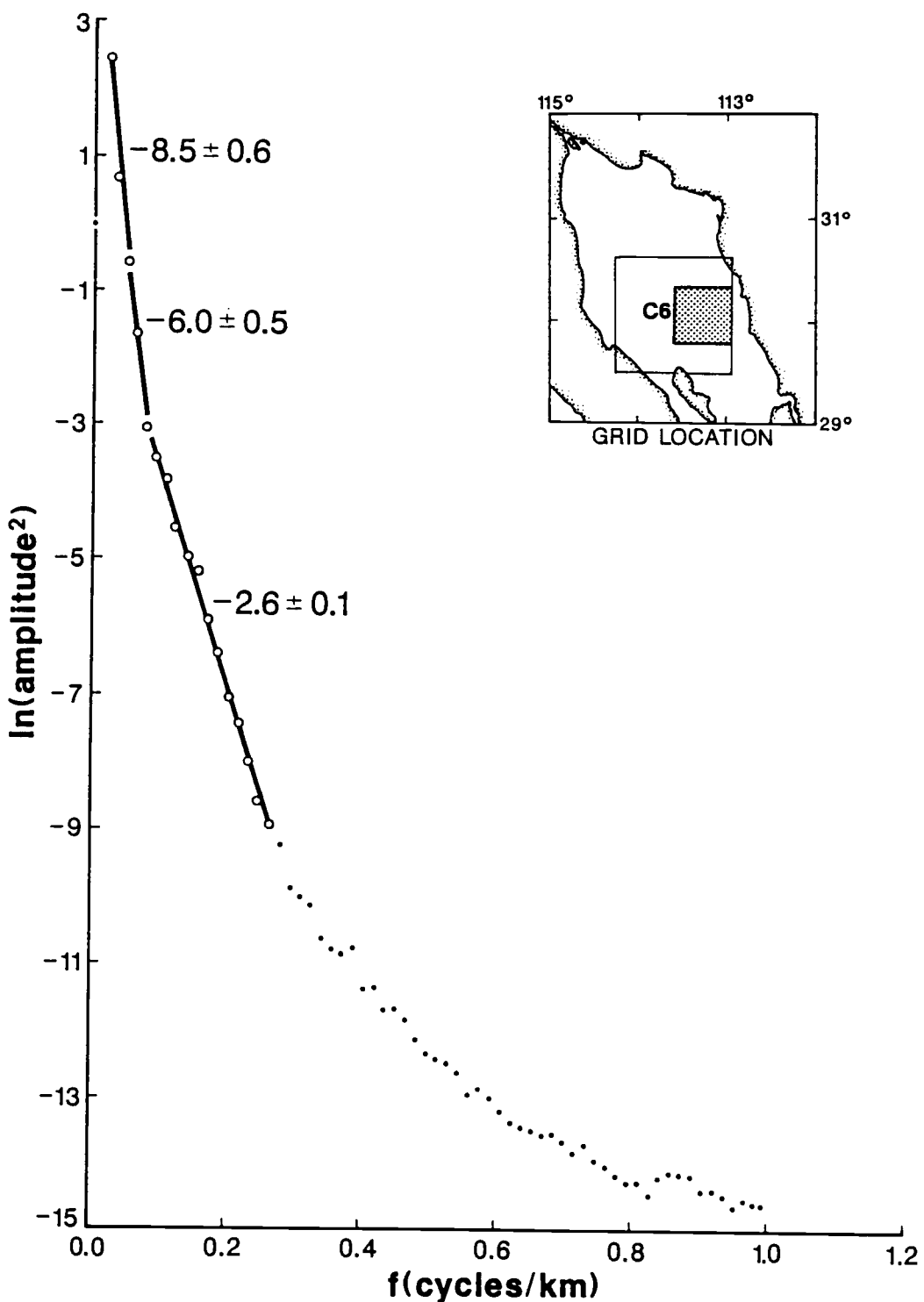


Figure A16. Radially averaged power spectrum of grid C6, using the 2DFFT. See explanation in figure 10.

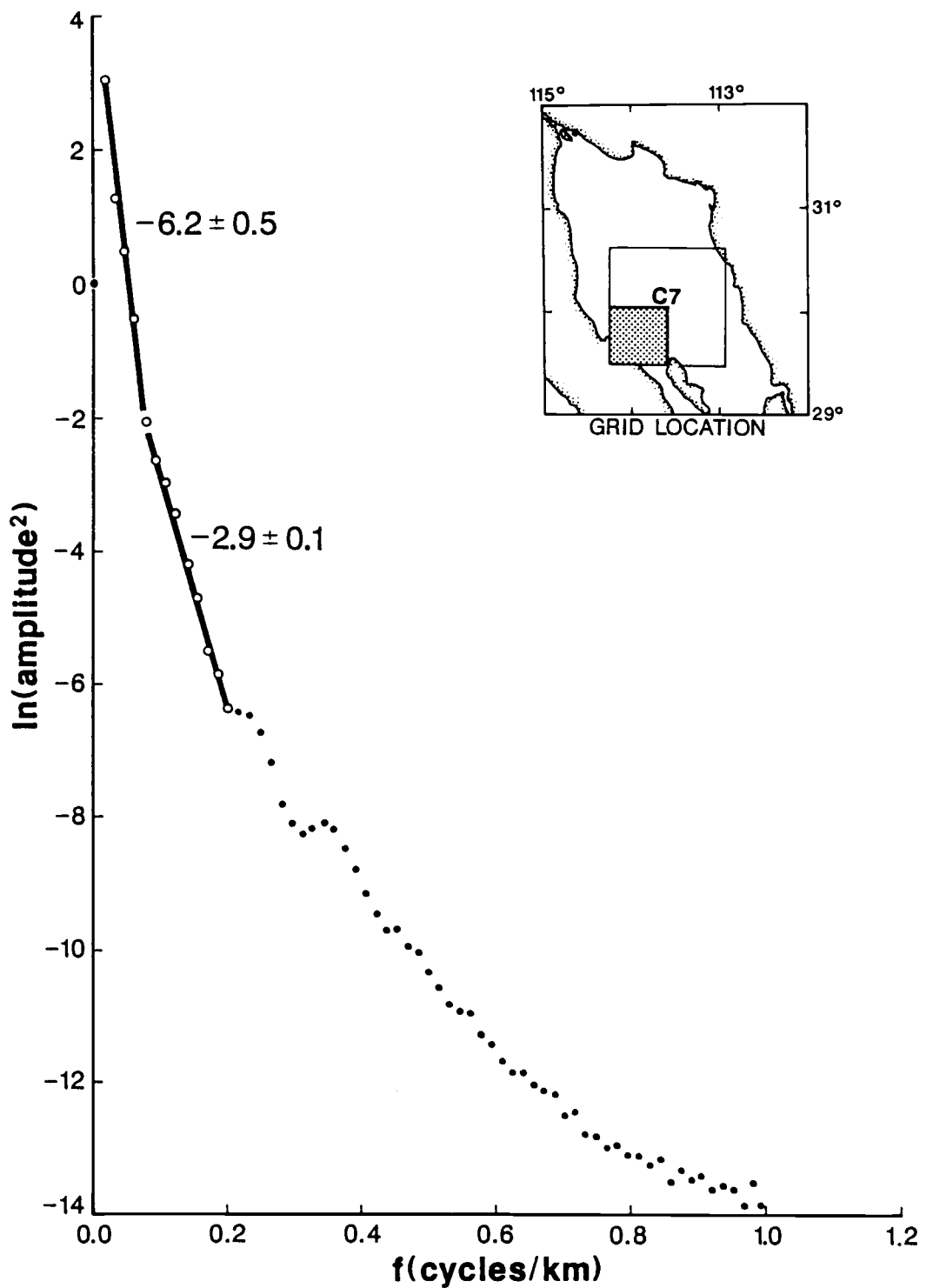


Figure A17. Radially averaged power spectrum of grid C7, using the 2DFFT. See explanation in figure 10.

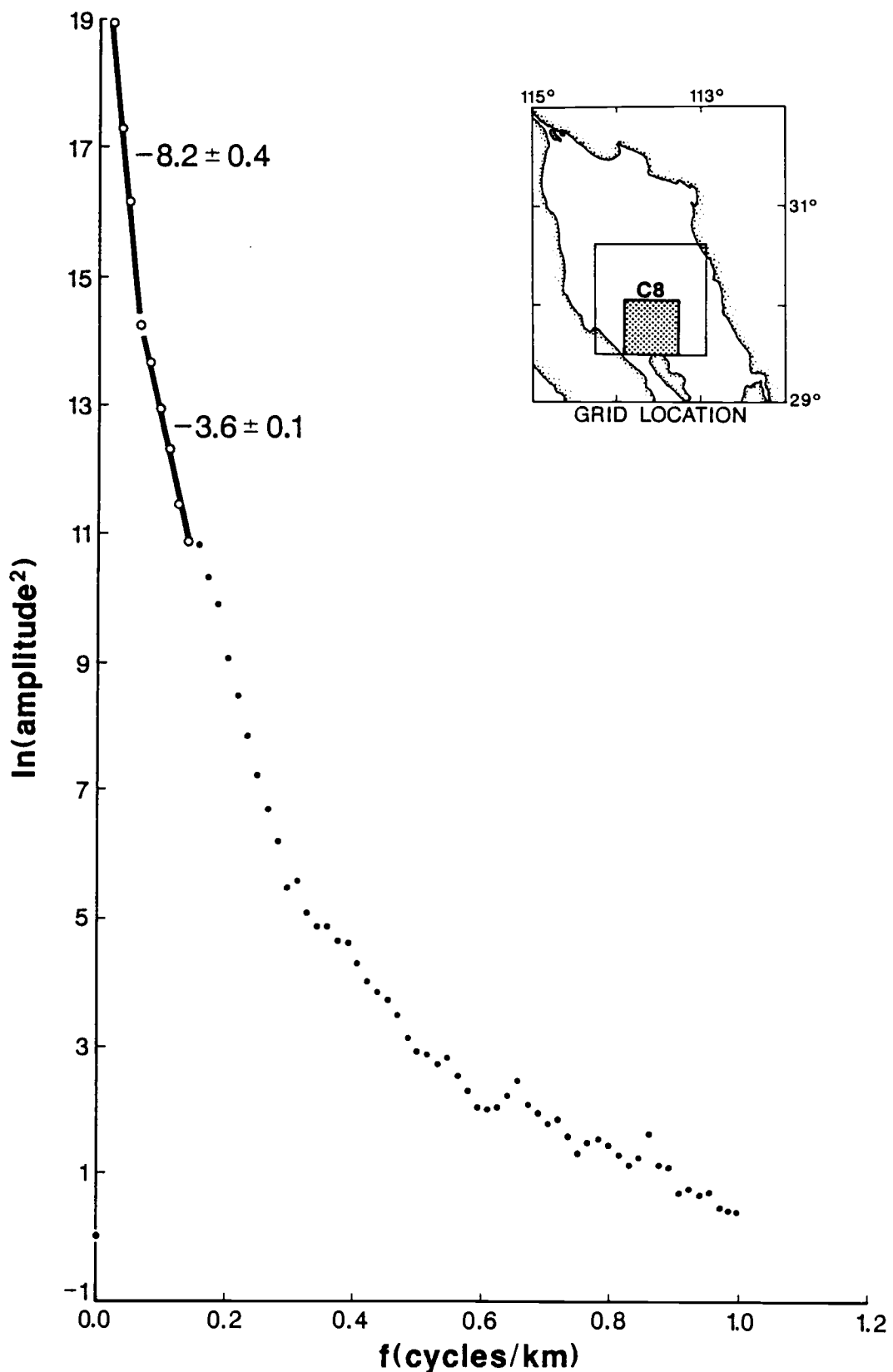


Figure A18. Radially averaged power spectrum of grid C8, using the 2DFFT. See explanation in figure 10.

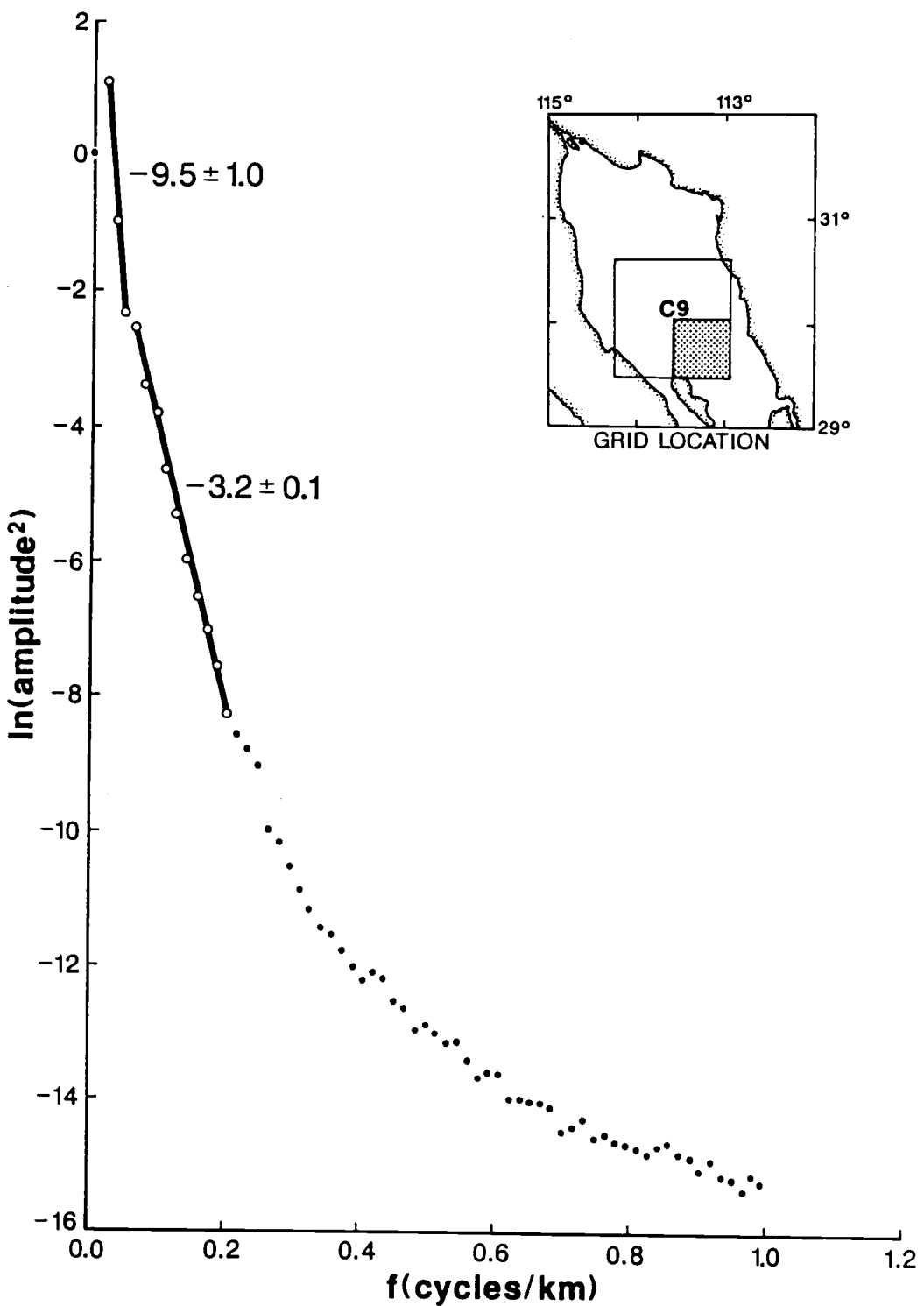


Figure A19. Radially averaged power spectrum of grid C9, using the 2DFFT. See explanation in figure 10.

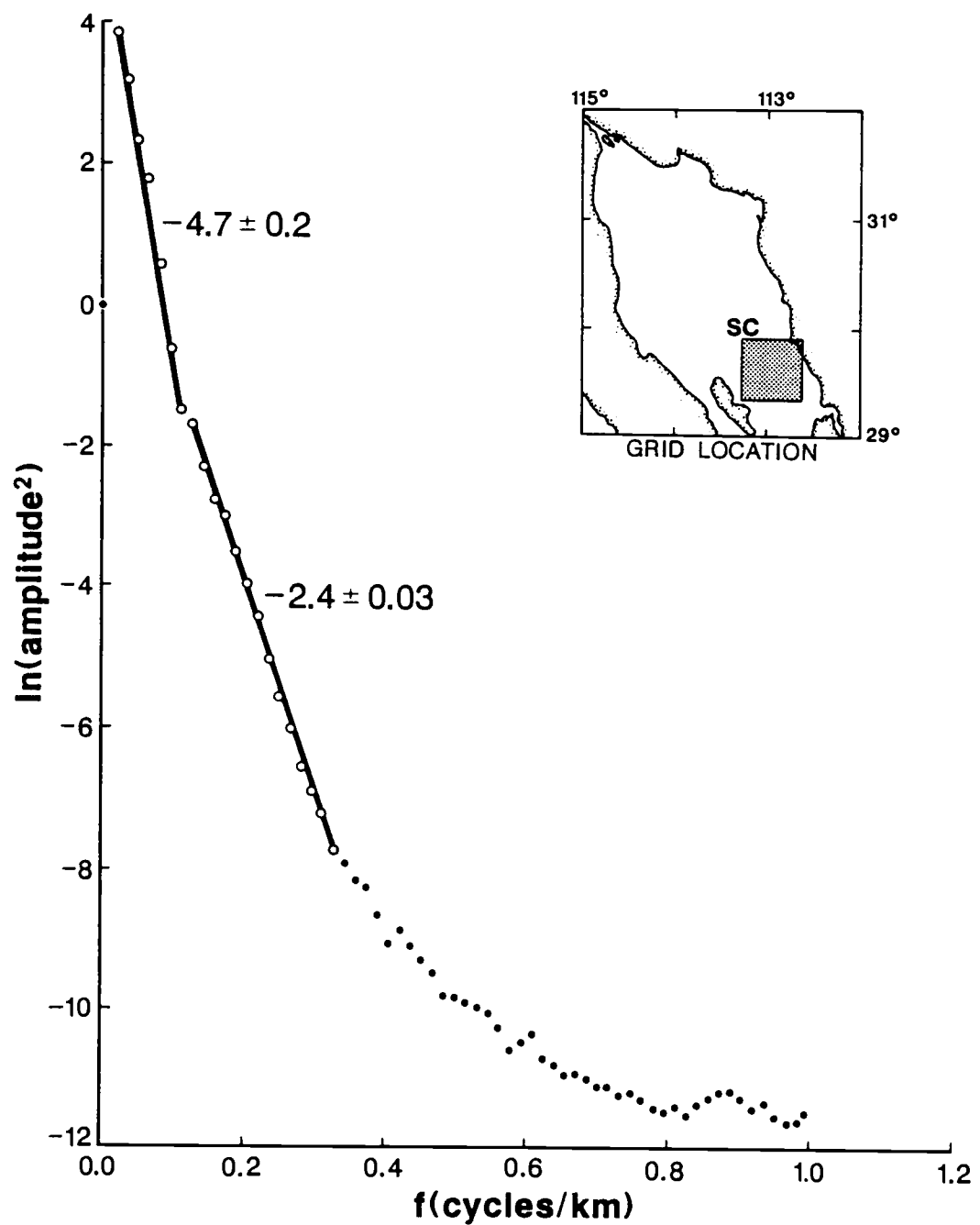


Figure A20. Radially averaged power spectrum of grid SC, using the 2DFFT. See explanation in figure 10.

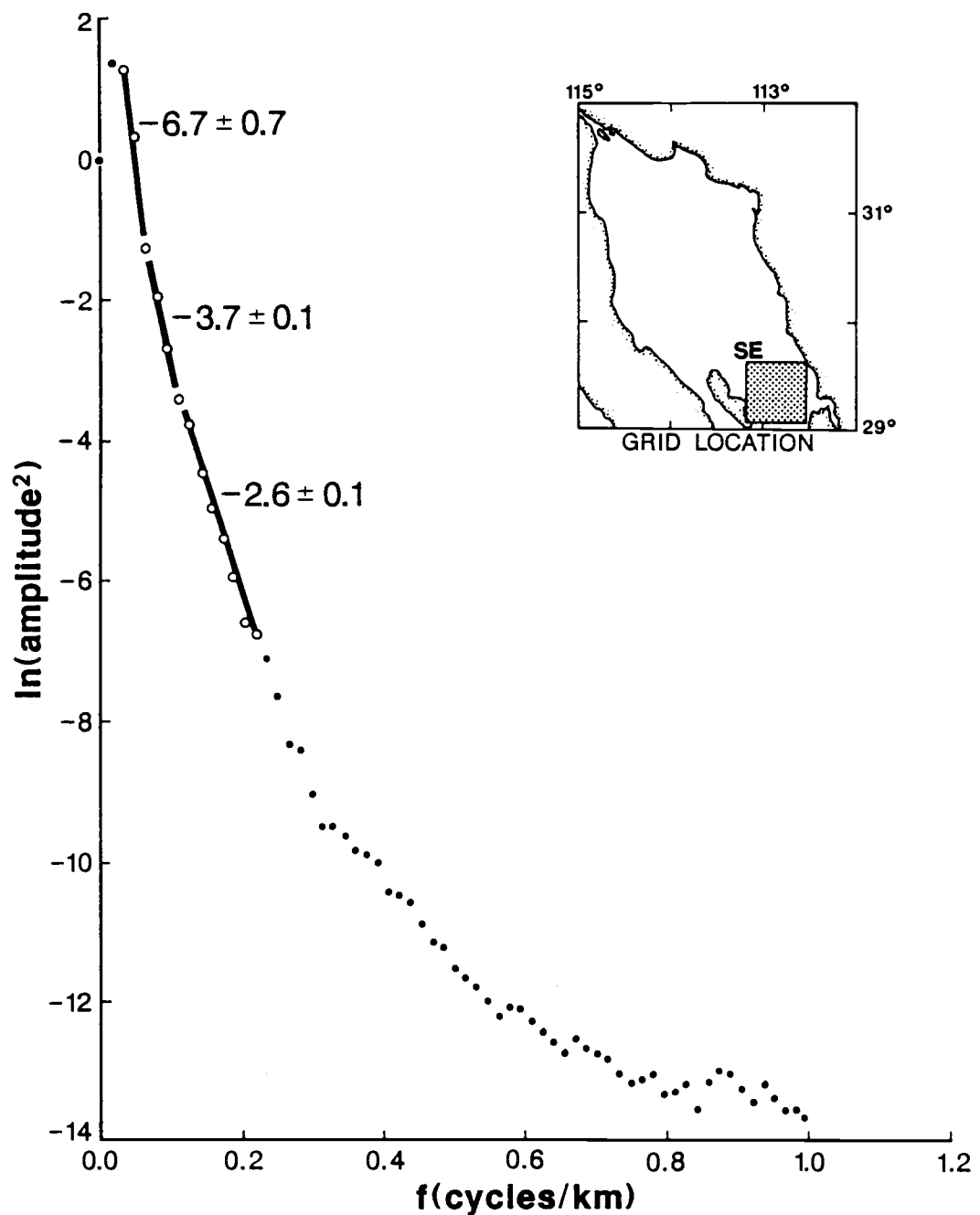
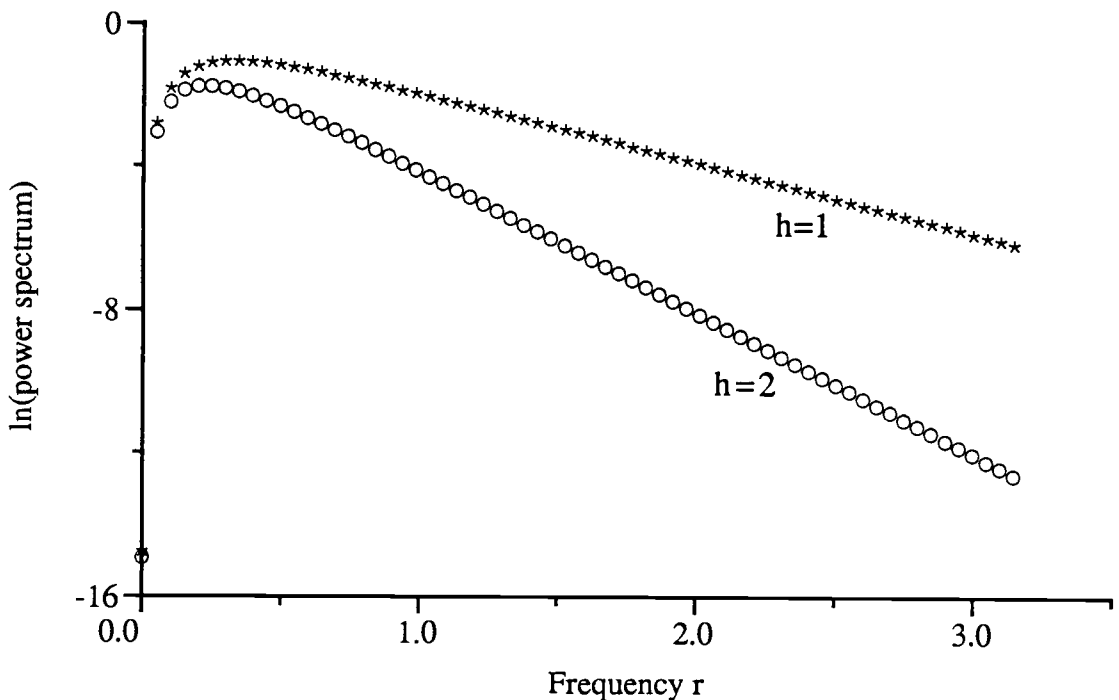
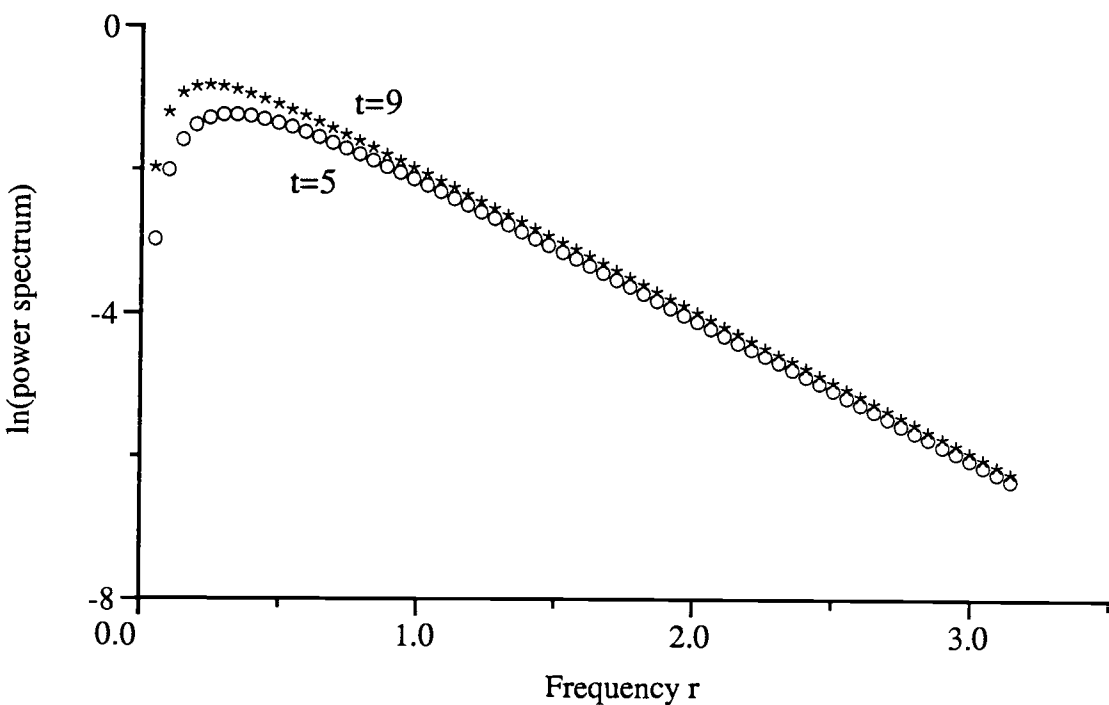


Figure A21. Radially averaged power spectrum of grid SE, using the 2DFFT. See explanation in figure 10.



A) Effect of different depths to the top, for $t=5$



B) Effect of different thicknesses, for $h=1$

Figure A22. Plots of the radially averaged theoretical power spectrum.

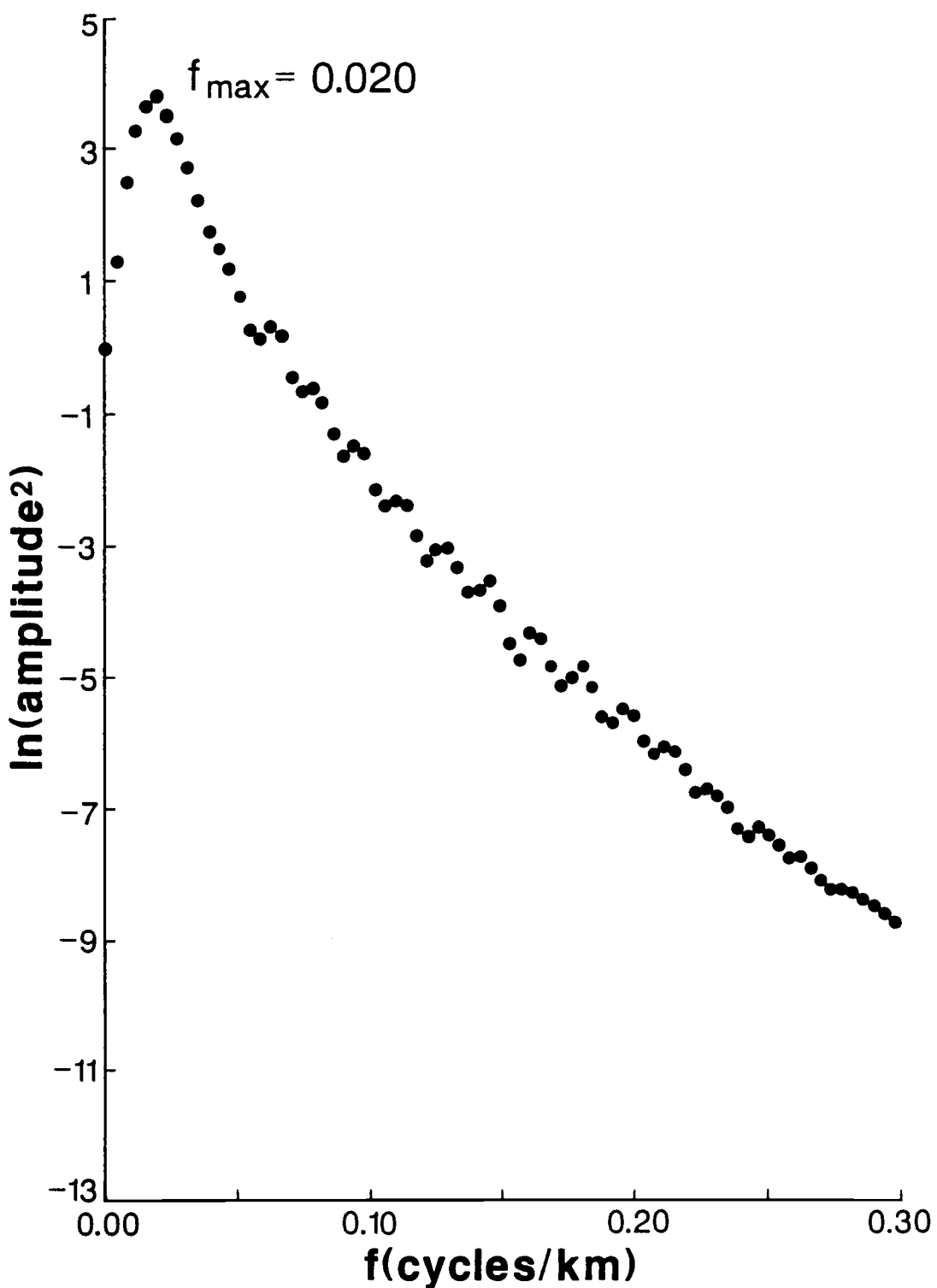


Figure A23. Plot of the radially averaged power spectrum for a grid appended with zeroes.

APPENDIX B

Radially Averaged Spectral Plots Using 2DMEM

The following is a simple development on how to obtain the power spectrum using maximum entropy, taken from Kanasewich (1981). The plots of the radially averaged power spectrum using 2DMEM for the 32 km by 32 km grids of the northern Gulf of California are shown at the end.

Maximum Entropy Method 1-D

From the operational point of view, the maximum entropy method of spectral estimation, consists of obtaining a Prediction Error Filter.

Start with the design of an $N + 1$ point prediction operator \mathbf{D}' . From the optimum filter theory of Wiener

$$\mathbf{A}\mathbf{D}' = \mathbf{C}$$

\mathbf{A} is the N by N autocovariance matrix and \mathbf{C} is a column vector formed with the cross covariance between the input signal, x , and the desired output. This can be written out as:

$$\begin{bmatrix} a_0 & a_1 & \dots & a_{N-1} \\ a_1 & a_2 & \dots & a_{N-2} \\ \vdots & \vdots & \ddots & \vdots \\ \vdots & \vdots & \ddots & \vdots \\ a_{N-1} & a_{N-2} & \dots & a_0 \end{bmatrix} \begin{bmatrix} d_1 \\ d_2 \\ \vdots \\ \vdots \\ d_N \end{bmatrix} = \begin{bmatrix} c_0 \\ c_1 \\ \vdots \\ \vdots \\ c_{N-1} \end{bmatrix}$$

The unnormalized cross covariance, apart from a factor of $1/N$, for a prediction error operator is given by

$$c_L = \sum_{t=0}^{N-1} x_t y_{t+L} = \sum_{t=0}^{N-1} x_t x_{t+T+L} = a_{T+L}$$

since the desired output is the input signal at some time $t + T$, which is related to the autocovariance function at lag $T + L$. Set the prediction distance T , at one unit of sampled time. The matrix then becomes

$$\begin{bmatrix} a_0 & a_1 & \dots & a_{N-1} \\ a_1 & a_2 & \dots & a_{N-2} \\ \vdots & \vdots & \ddots & \vdots \\ \vdots & \vdots & \ddots & \vdots \\ a_{N-1} & a_{N-2} & \dots & a_0 \end{bmatrix} \begin{bmatrix} d_1 \\ d_2 \\ \vdots \\ \vdots \\ d_N \end{bmatrix} = \begin{bmatrix} a_1 \\ a_2 \\ \vdots \\ \vdots \\ a_N \end{bmatrix}$$

This system of N equations may be written out and an autocovariance coefficient a_i , added and subtracted to each equation so that the right hand side vanishes. The matrix is then augmented by the addition of a new equation to regain symmetry

$$\begin{aligned}
 -a_0 + a_1 d_1 + a_2 d_2 + \dots + a_N d_N &= -P_m \\
 -a_1 + a_0 d_1 + a_1 d_2 + \dots + a_{N-1} d_N &= a_1 - a_1 \\
 -a_2 + a_1 d_1 + a_0 d_2 + \dots + a_{N-2} d_N &= a_2 - a_2 \\
 &\vdots \\
 &\vdots \\
 &\vdots \\
 -a_N + a_{N-1} d_1 + a_{N-2} d_2 + \dots + a_0 d_N &= a_N - a_N
 \end{aligned}$$

Multiplying by -1, and defining a new set of filter coefficients

$$\mathbf{D} = \begin{bmatrix} 1 \\ D_1 \\ \vdots \\ D_N \end{bmatrix} = \begin{bmatrix} 1 \\ -d_1 \\ \vdots \\ -d_N \end{bmatrix}$$

the matrix form becomes

$$\begin{bmatrix} a_0 & a_1 & \dots & a_N \\ a_1 & a_0 & \dots & a_{N-1} \\ \vdots & \vdots & \ddots & \vdots \\ a_N & a_{N-1} & \dots & a_0 \end{bmatrix} \begin{bmatrix} 1 \\ D_1 \\ \vdots \\ D_N \end{bmatrix} = \begin{bmatrix} P_m \\ 0 \\ \vdots \\ 0 \end{bmatrix}$$

This system of equations must be solved to obtain the filter coefficients and the factor P_m . This is Burg's (1967) equation for the prediction error filter at a distance of one time unit. In matrix notation

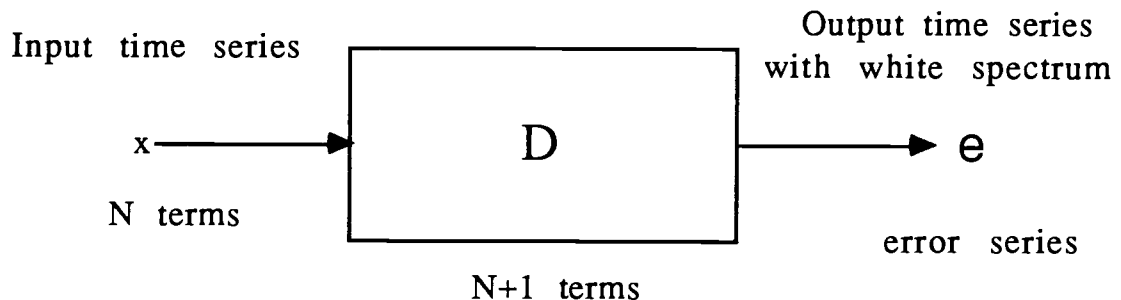
$$\mathbf{AD} = \mathbf{P}$$

Since the input wavelet contains N terms and the cross correlation contains only the non-zero term, this implies that the

prediction operator shortens the output wavelet to a spike in which P_m is the mean square error or the mean output power.

D may be considered a set of prediction filter weights which, when convolved with the input data, will generate a white noise series. The elements of the noise series will be uncorrelated with each other and the filter will have created the greatest destruction of entropy possible.

Whitening Filter



The input power spectrum may be obtained by correcting the output power for the response of the filter. In the frequency domain this is equivalent to

$$\text{Input power spectrum} = \frac{\text{Output power spectrum}}{\text{Power response of the filter}}$$

The input power spectrum of the time series is designated by Burg as the maximum entropy estimate of power, P_E .

$$P_E(f) = \frac{P_m/f_N}{2 \left| 1 + \sum_{n=1}^N D_n e^{-2\pi i f n \Delta t} \right|^2}$$

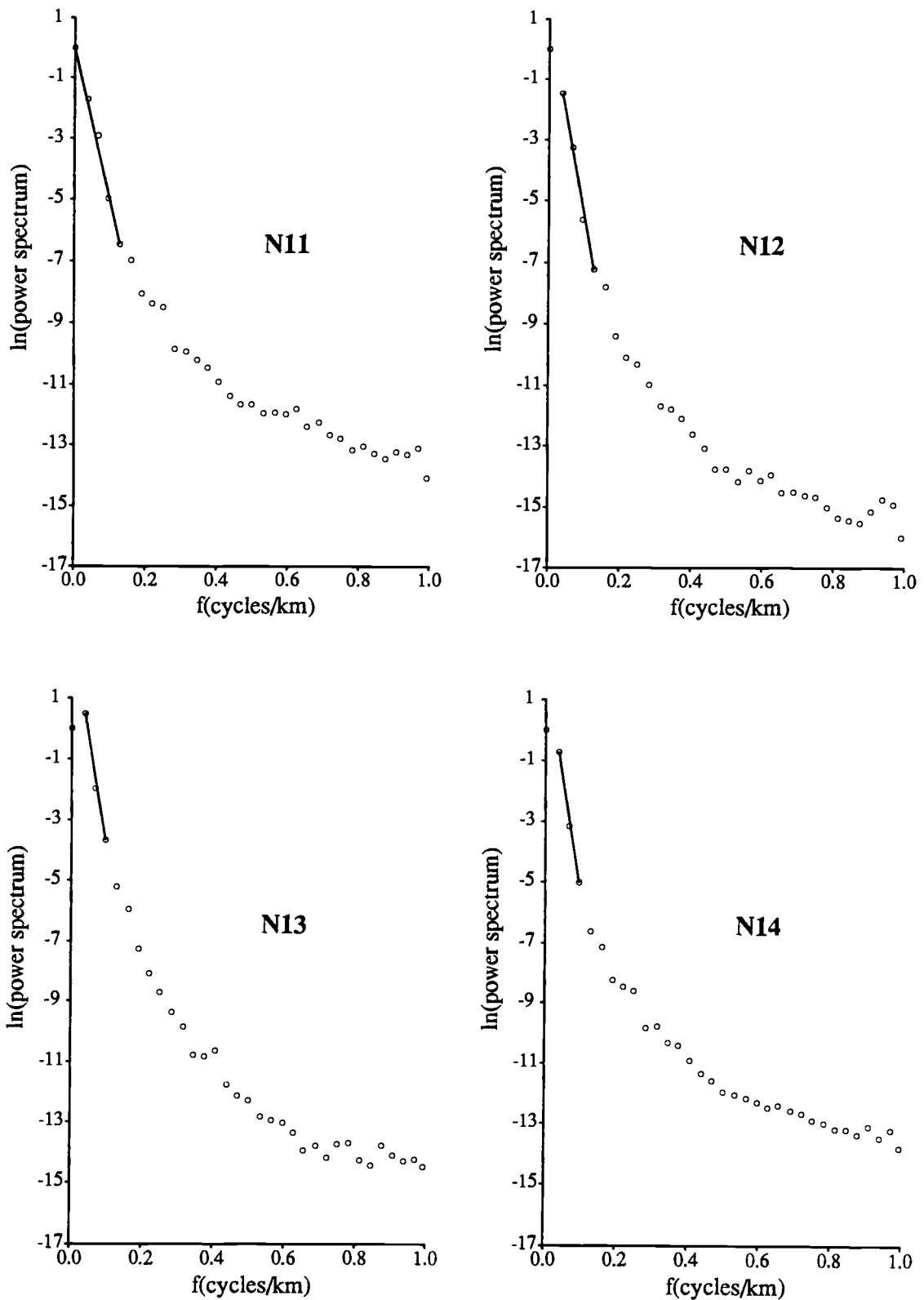


Figure B1. Maximum Entropy Radial Plots. Grids N11, N12, N13, and N14

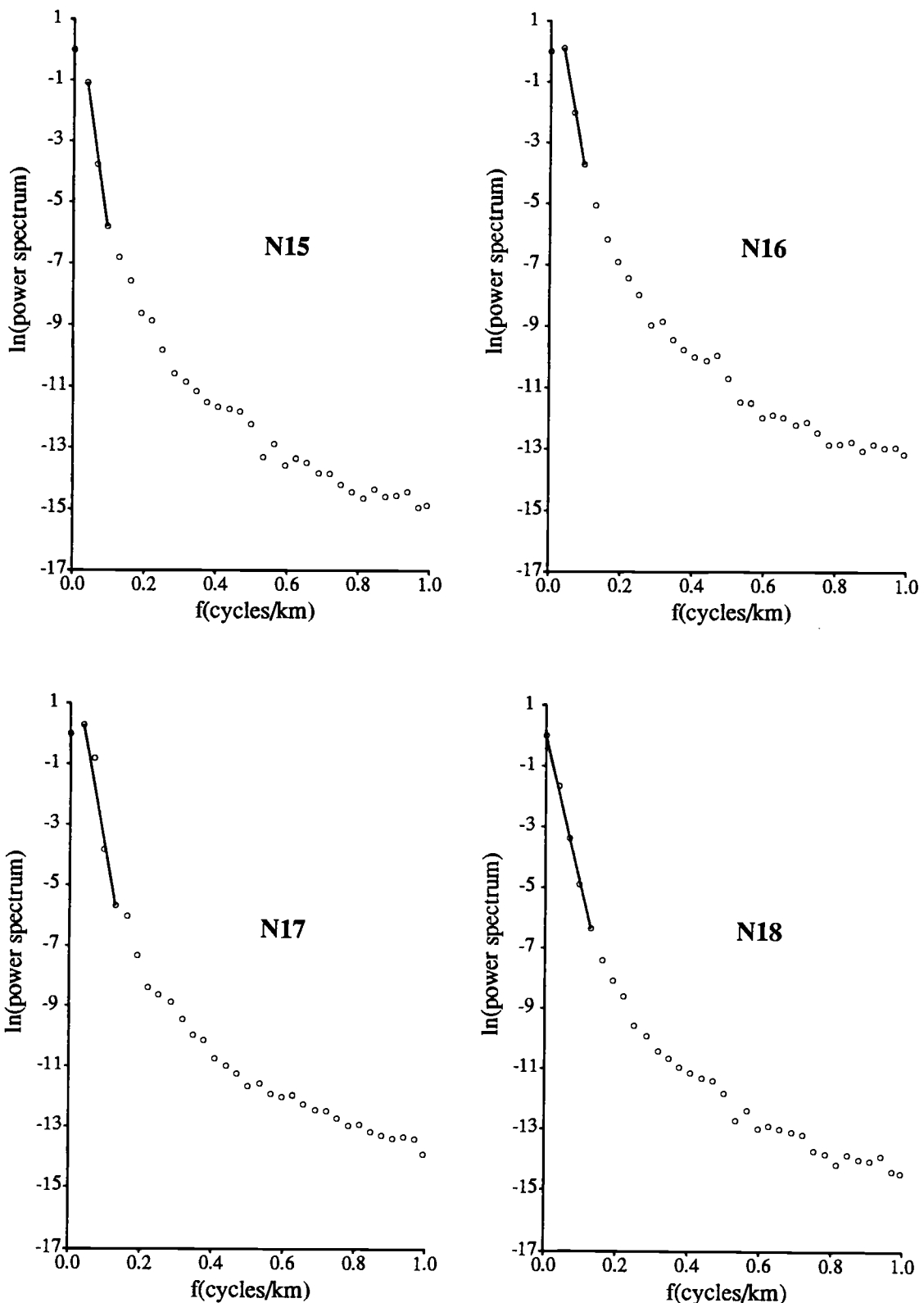


Figure B2. Maximum Entropy Radial Plots. Grids N15, N16, N17, and N18

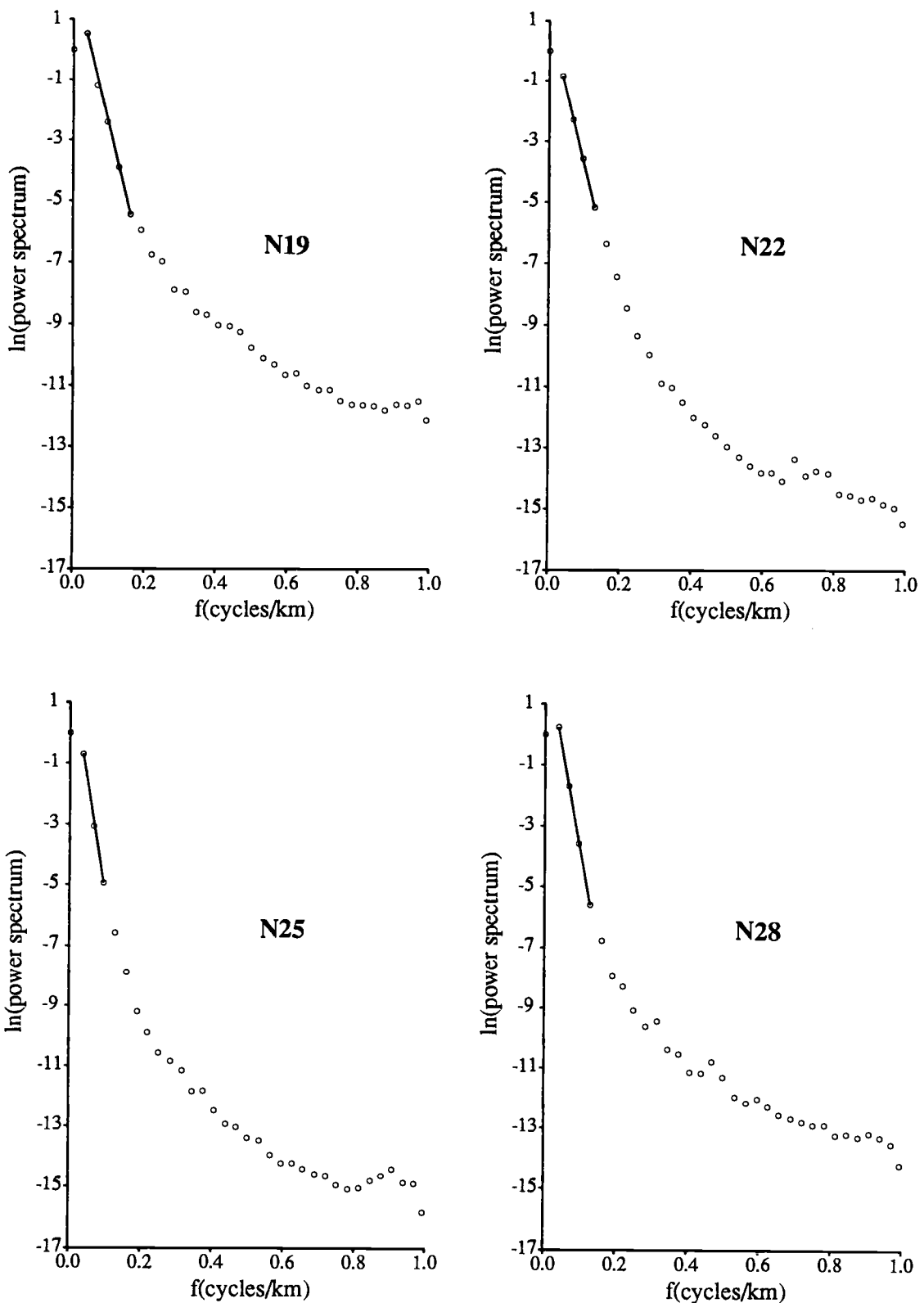


Figure B3. Maximum Entropy Radial Plots. Grids N19, N22, N25, and N28

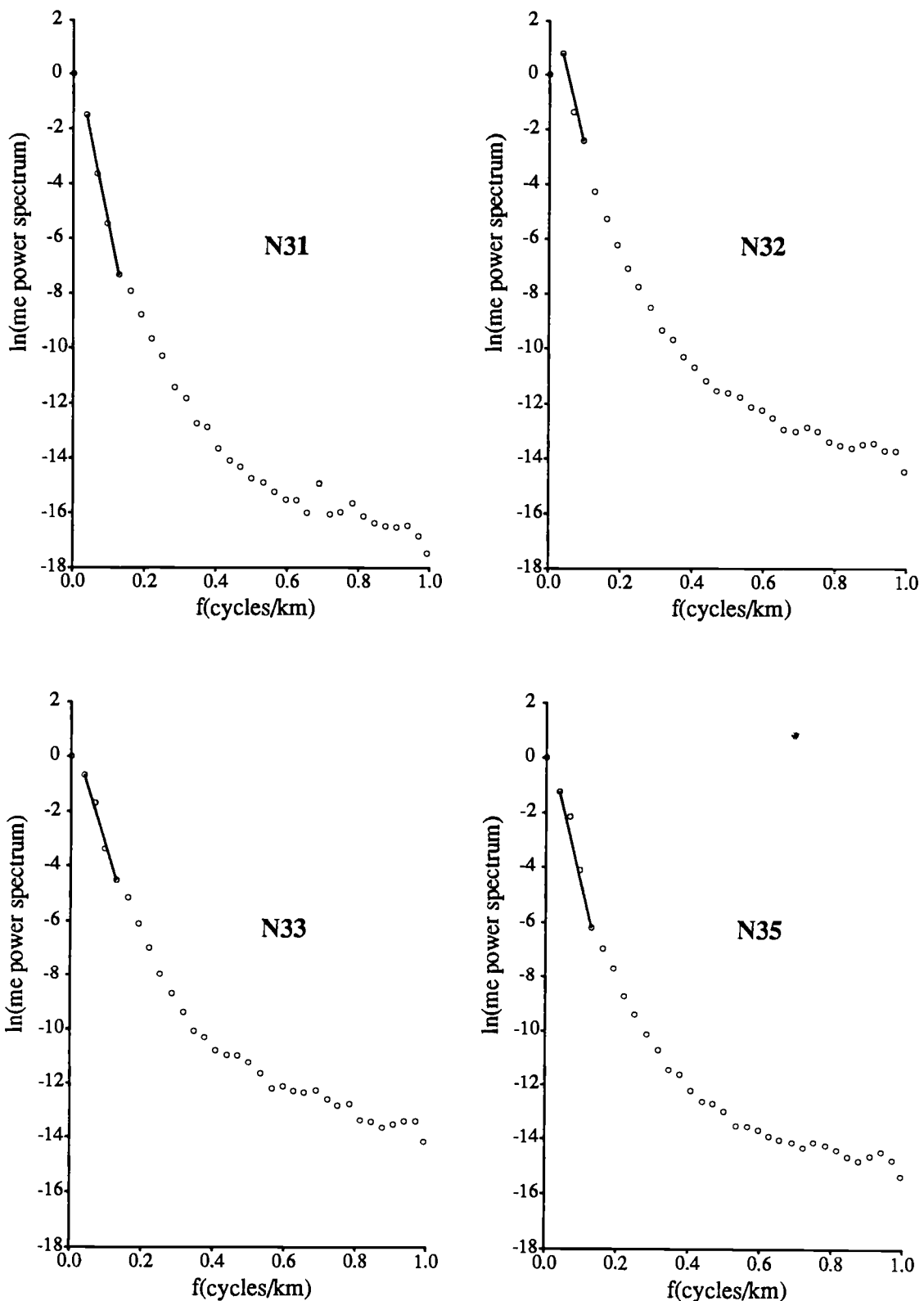


Figure B4. Maximum Entropy Radial Plots. Grids N31, N32, N33, and N35

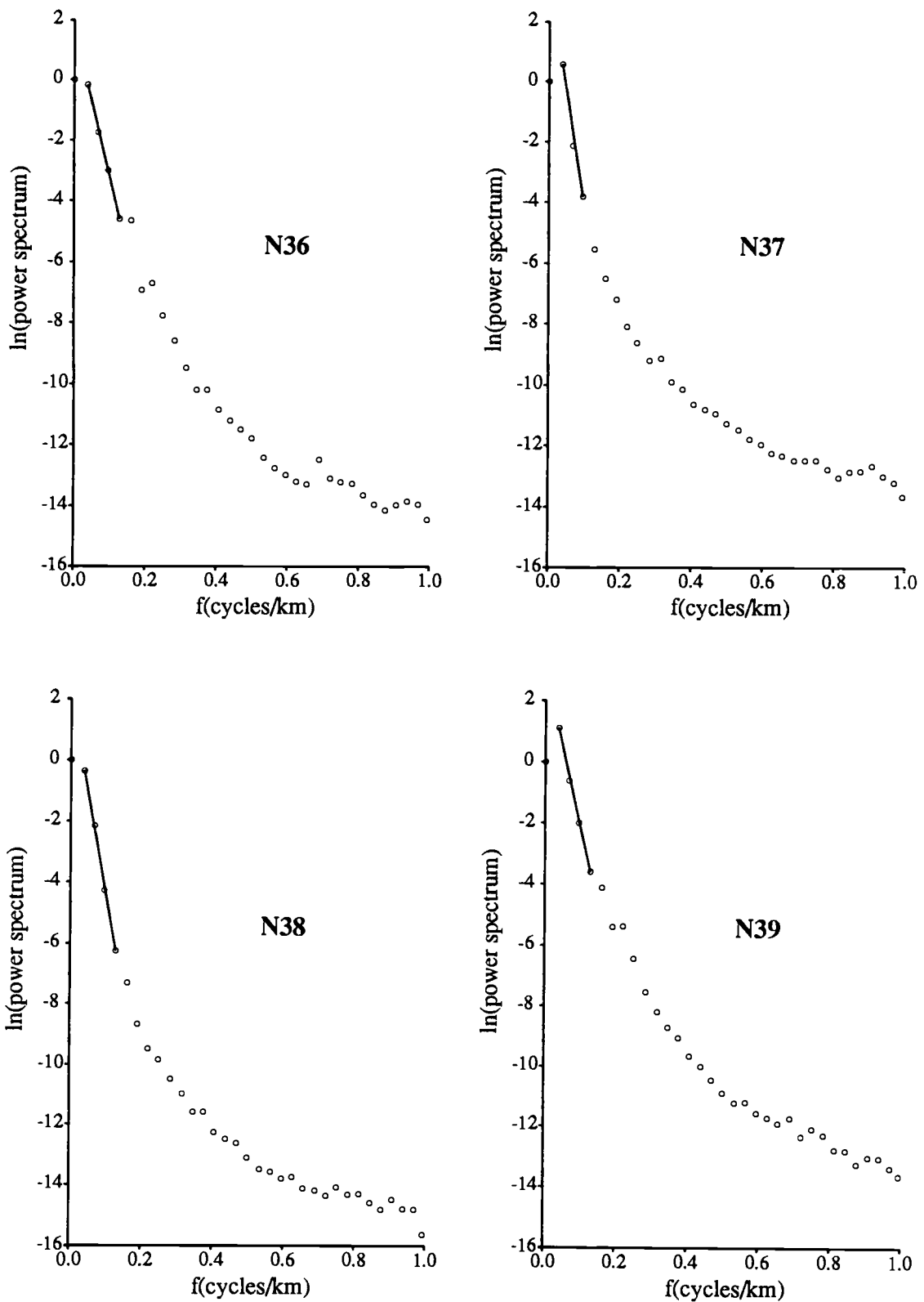


Figure B5. Maximum Entropy Radial Plots. Grids N36, N37, N38, and N39

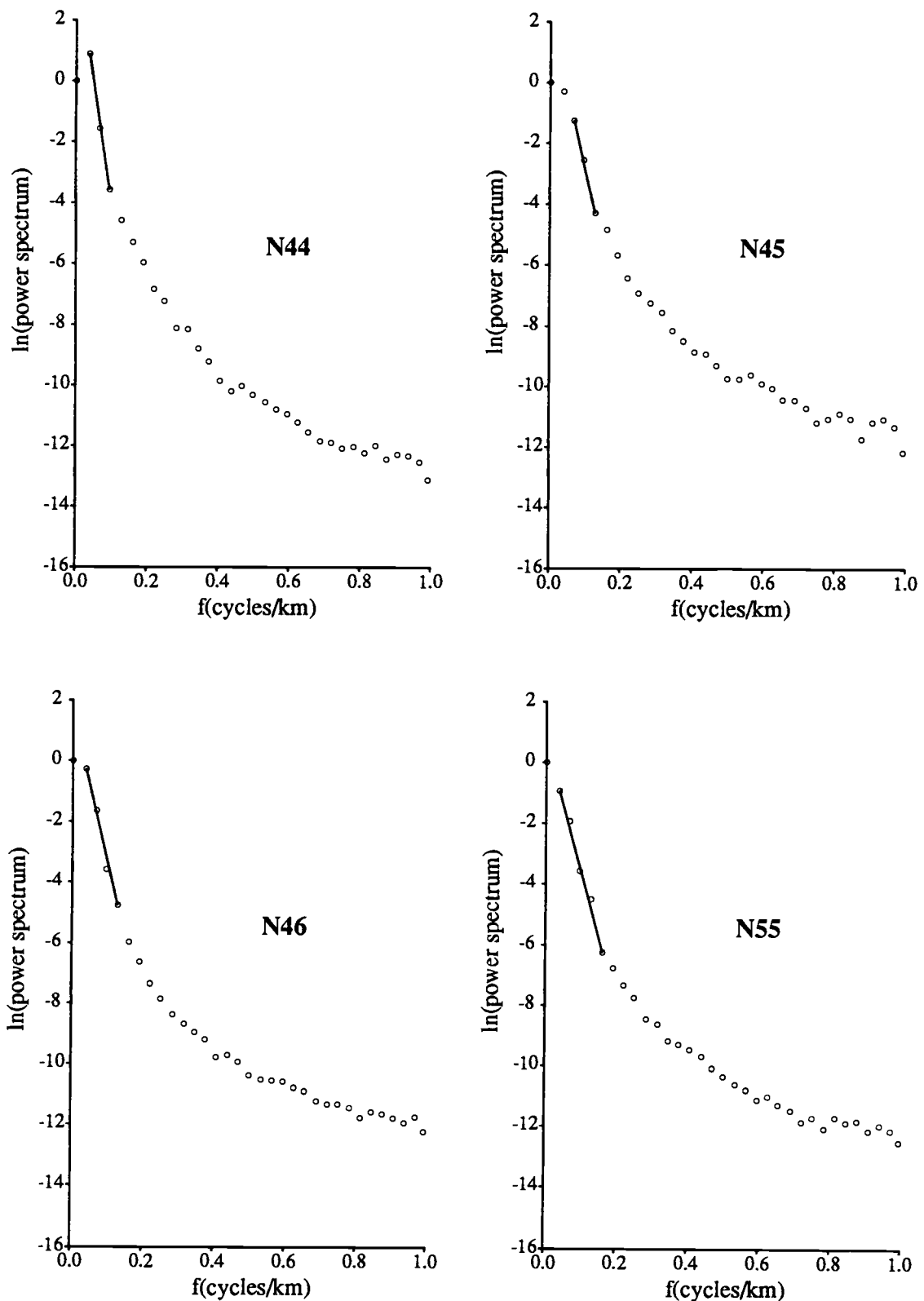


Figure B6. Maximum Entropy Radial Plots. Grids N44, N45, N46, and N55

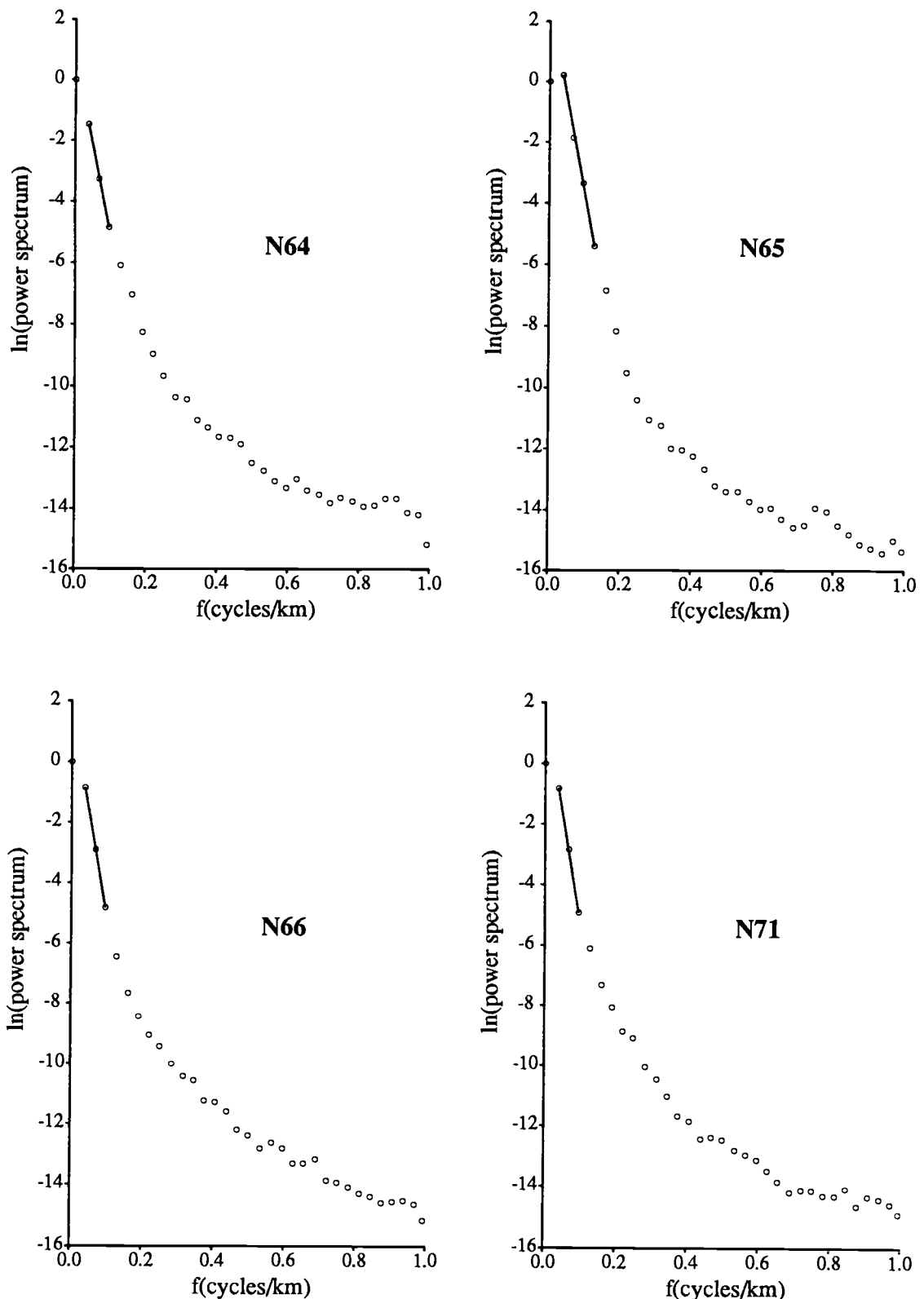


Figure B7. Maximum Entropy Radial Plots. Grids N64, N65, N66, and N71

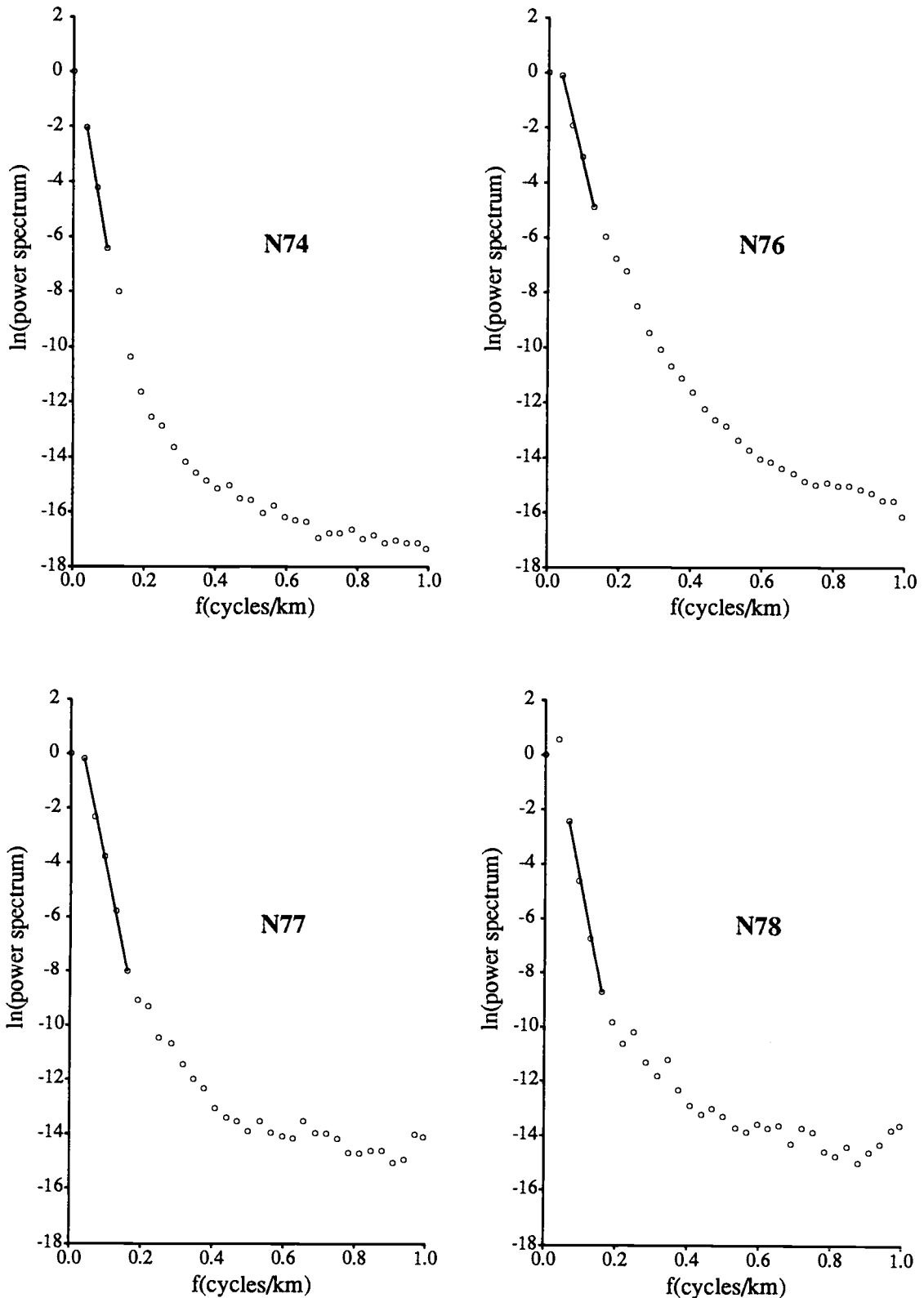


Figure B8. Maximum Entropy Radial Plots. Grids N74, N76, N77, and N78

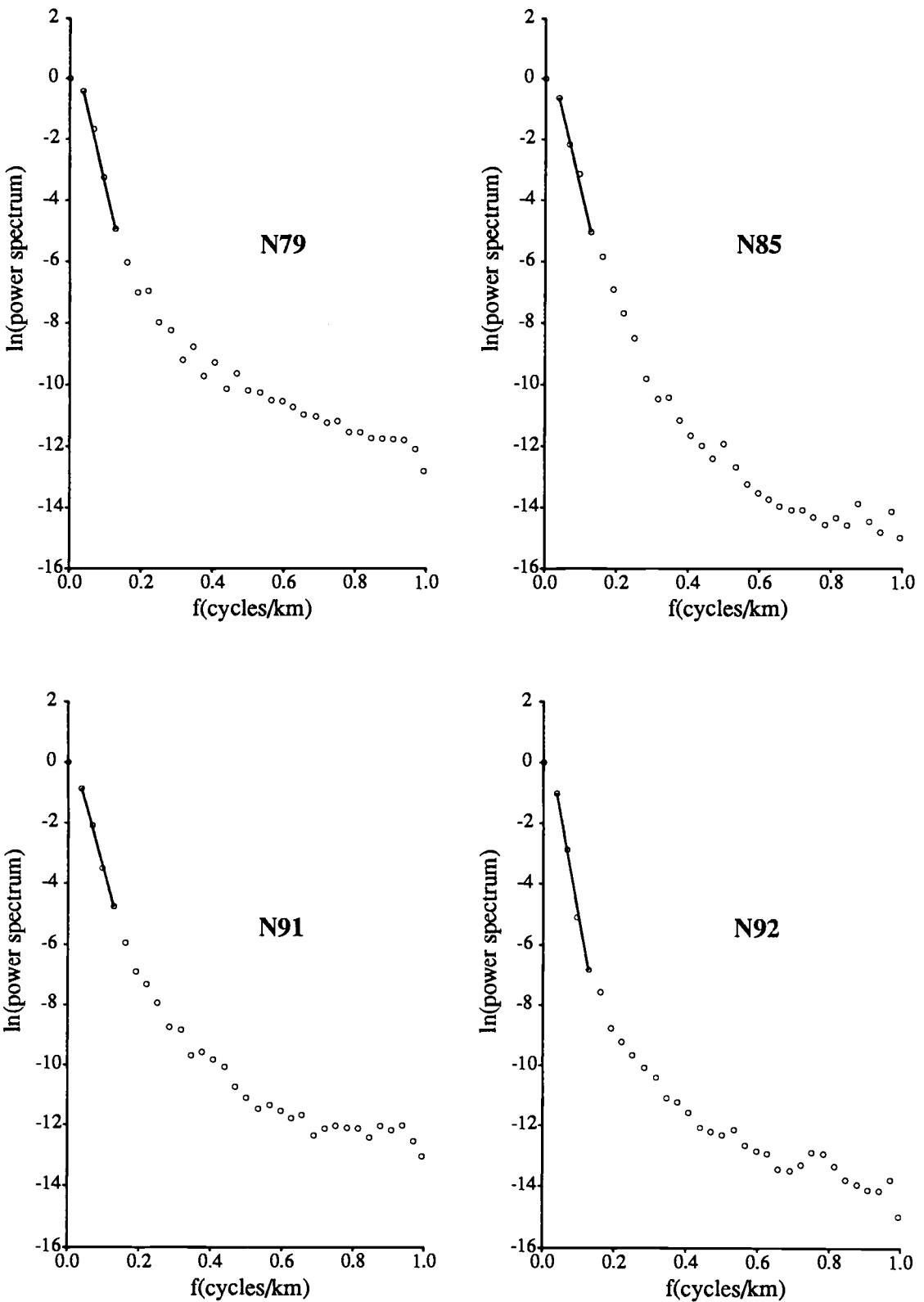


Figure B9. Maximum Entropy Radial Plots. Grids N79, N85, N91, and N92

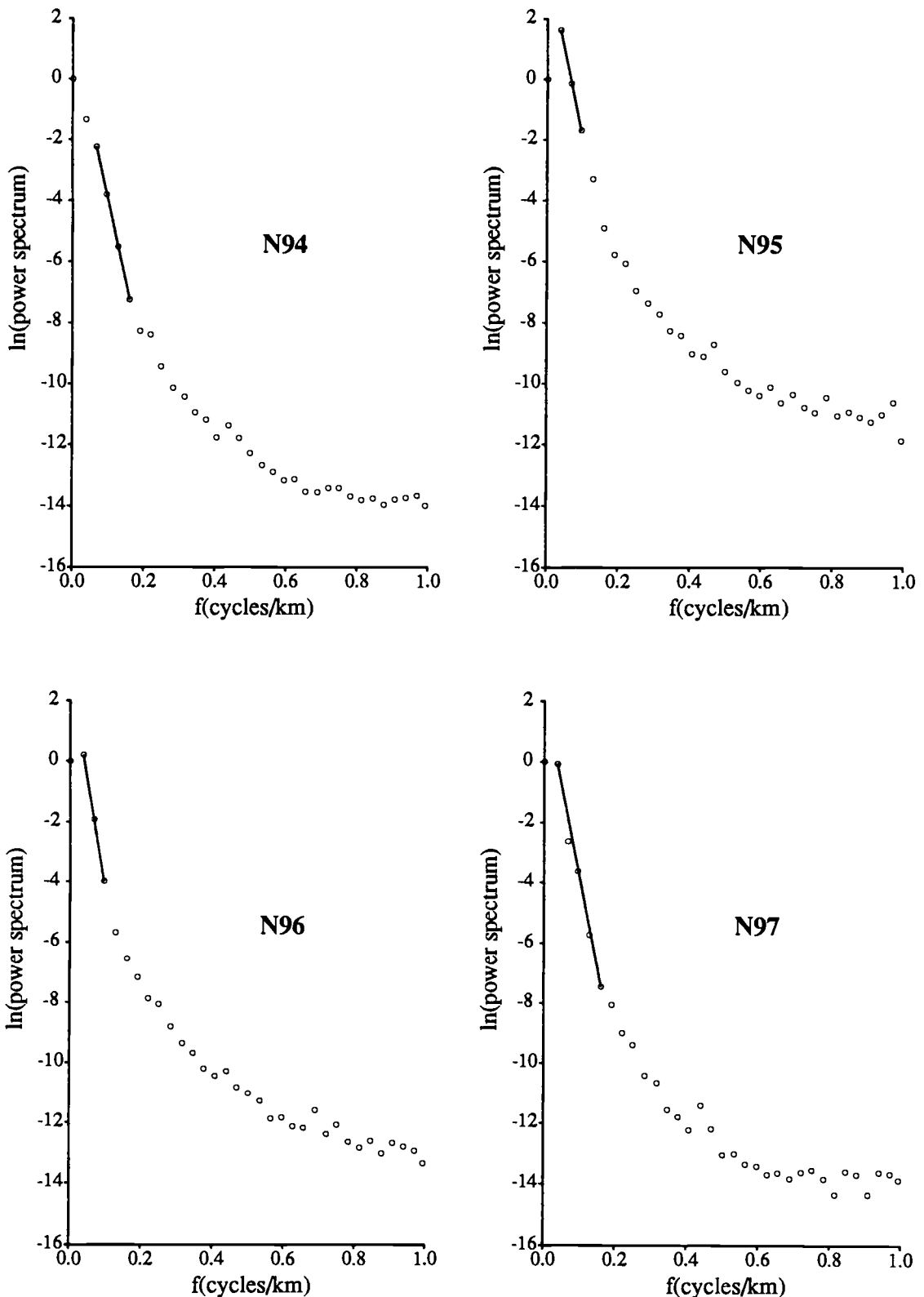


Figure B10. Maximum Entropy Radial Plots. Grids N94, N95, N96, and N97

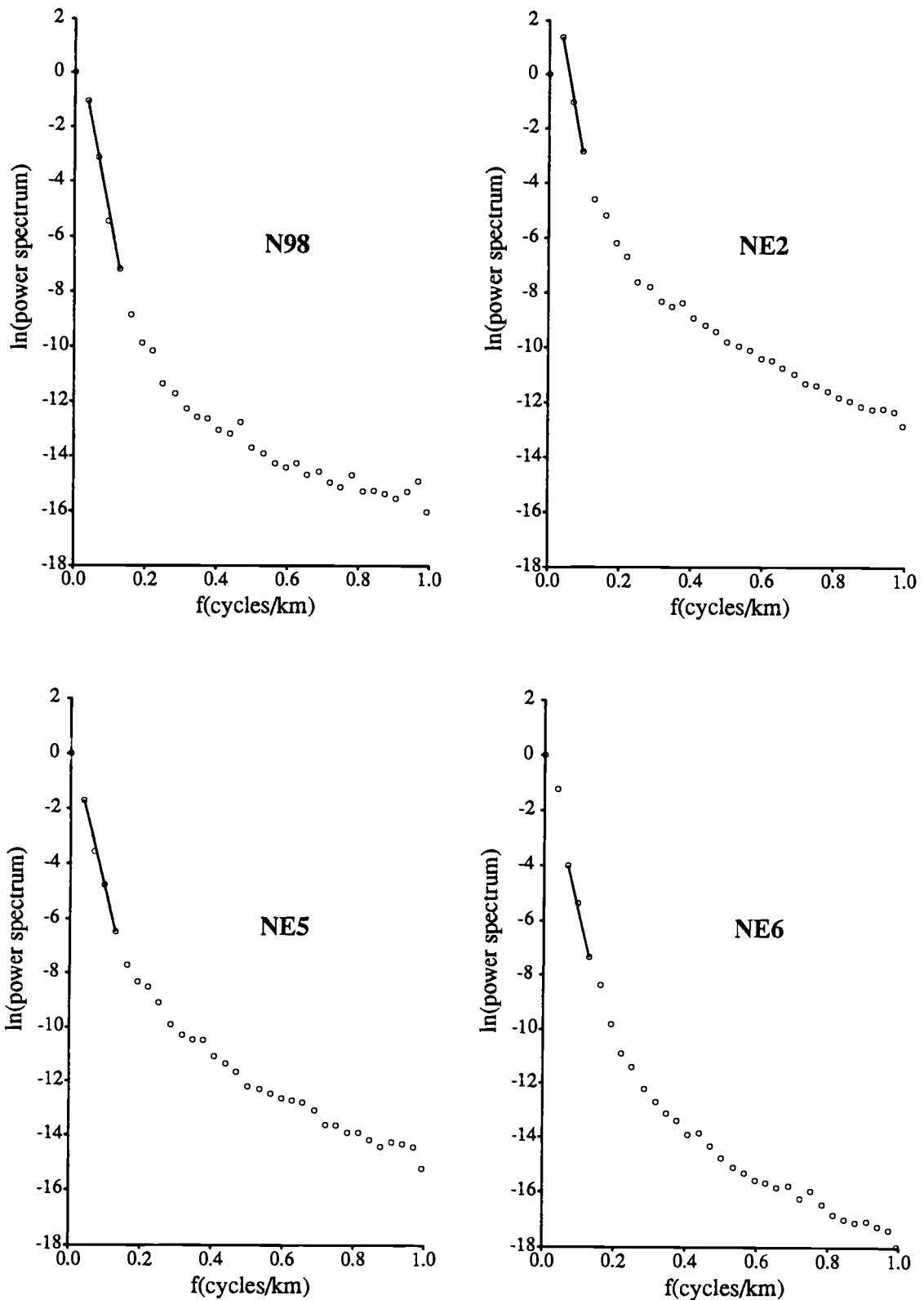


Figure B11. Maximum Entropy Radial Plots. Grids N98, NE2, NE5, and NE6

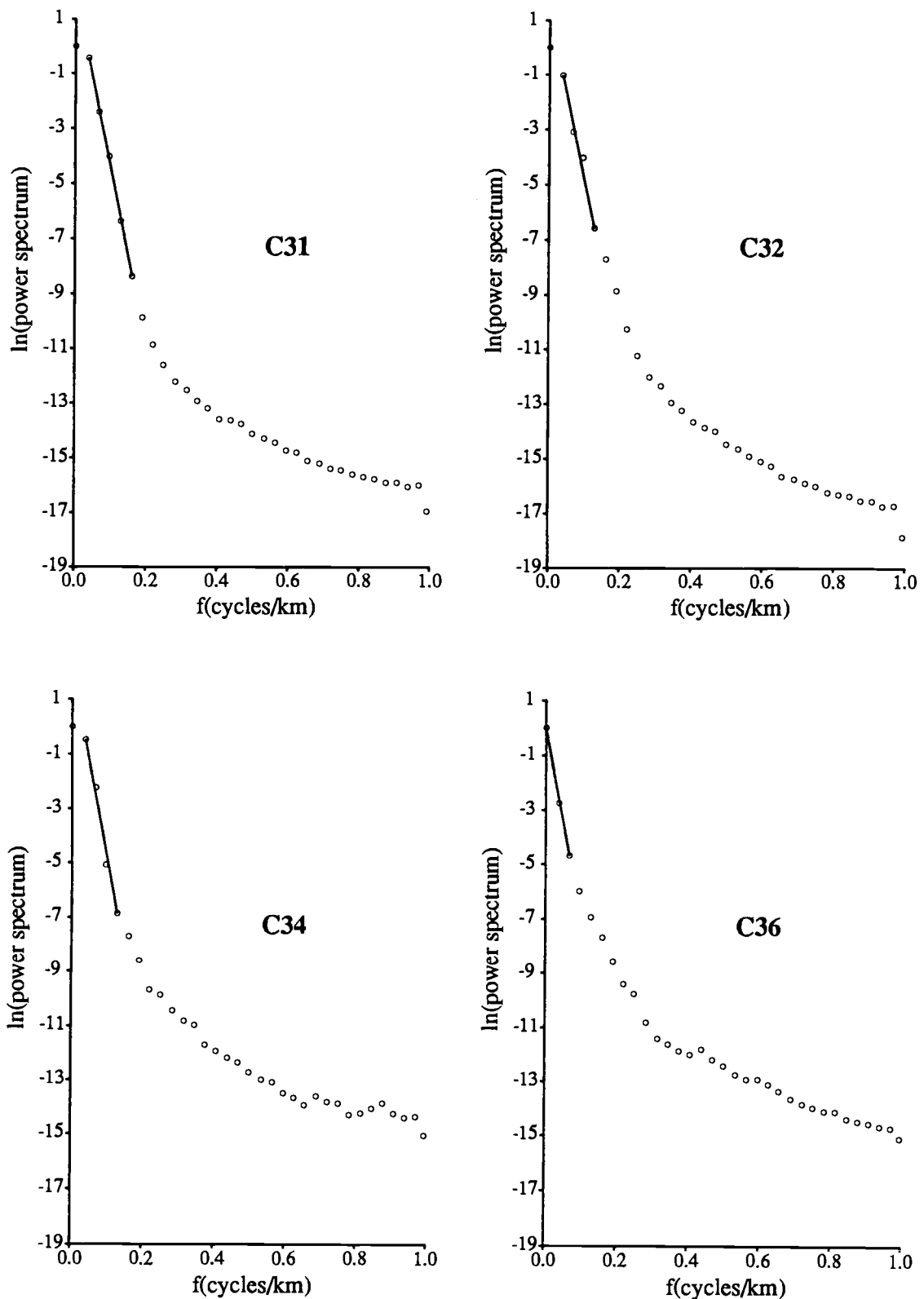


Figure B12. Maximum Entropy Radial Plots. Grids C31, C32, C34, and C36

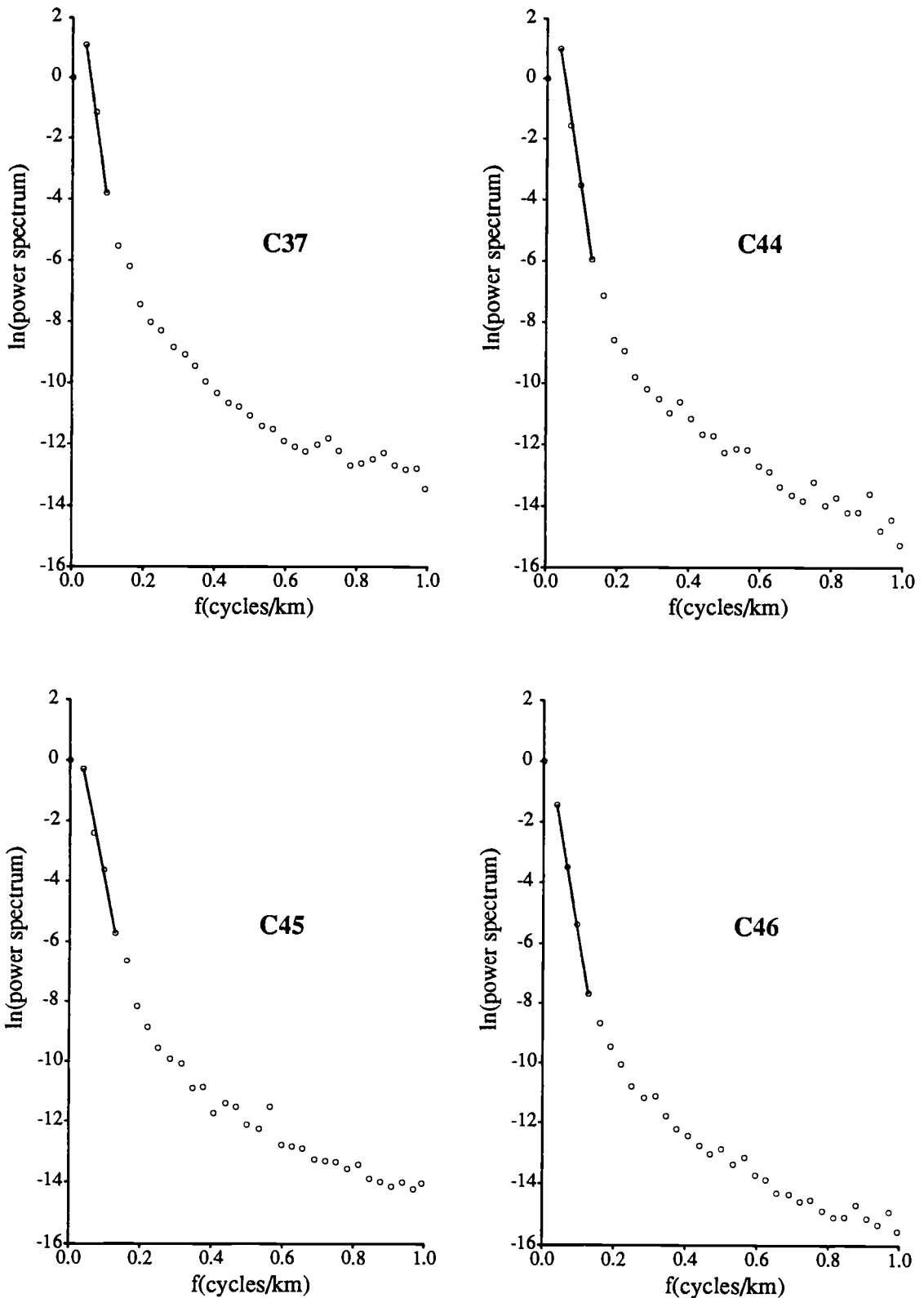


Figure B13. Maximum Entropy Radial Plots. Grids C37, C44, C45, and C46

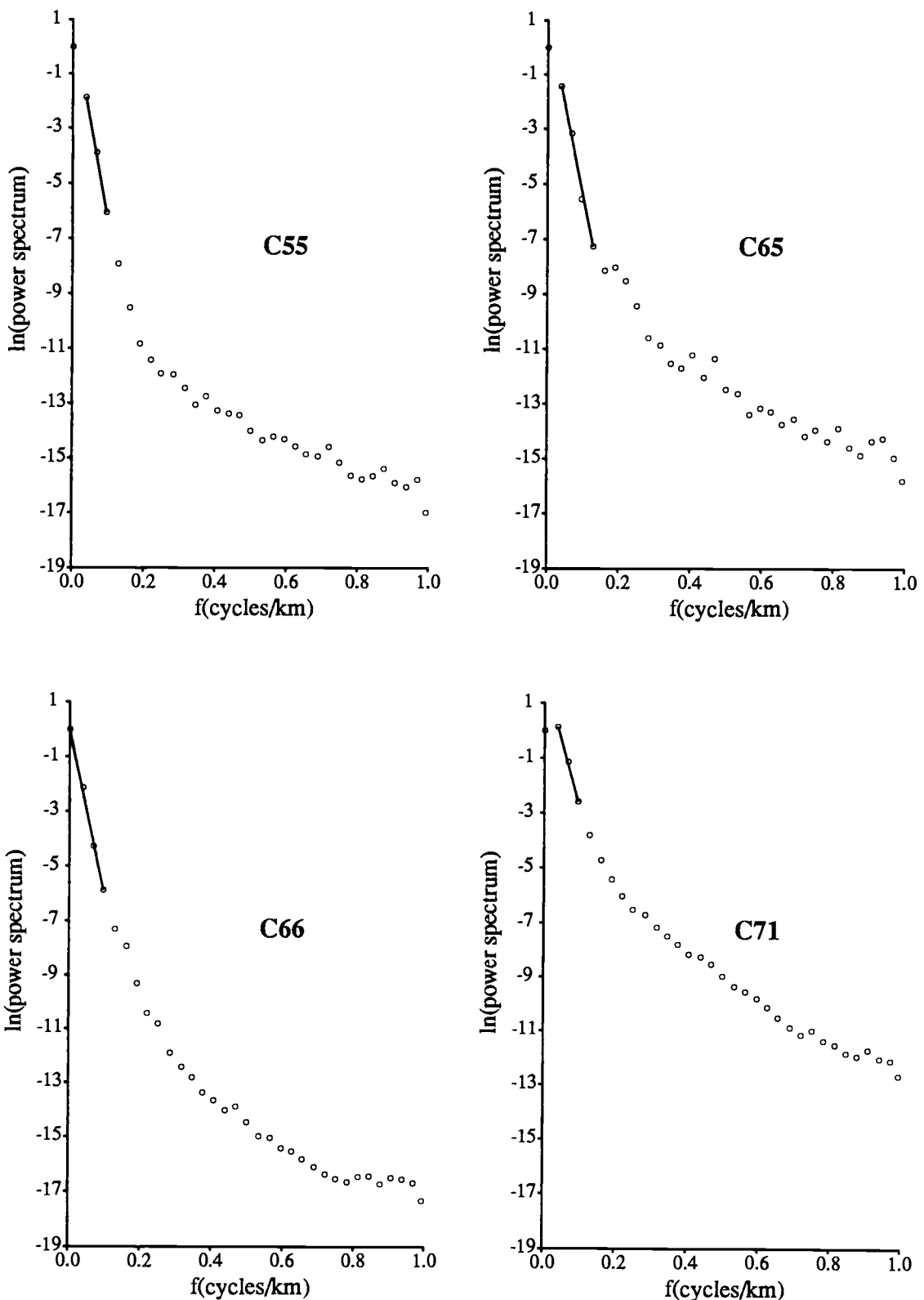


Figure B14. Maximum Entropy Radial Plots. Grids C55, C65, C66, and C71

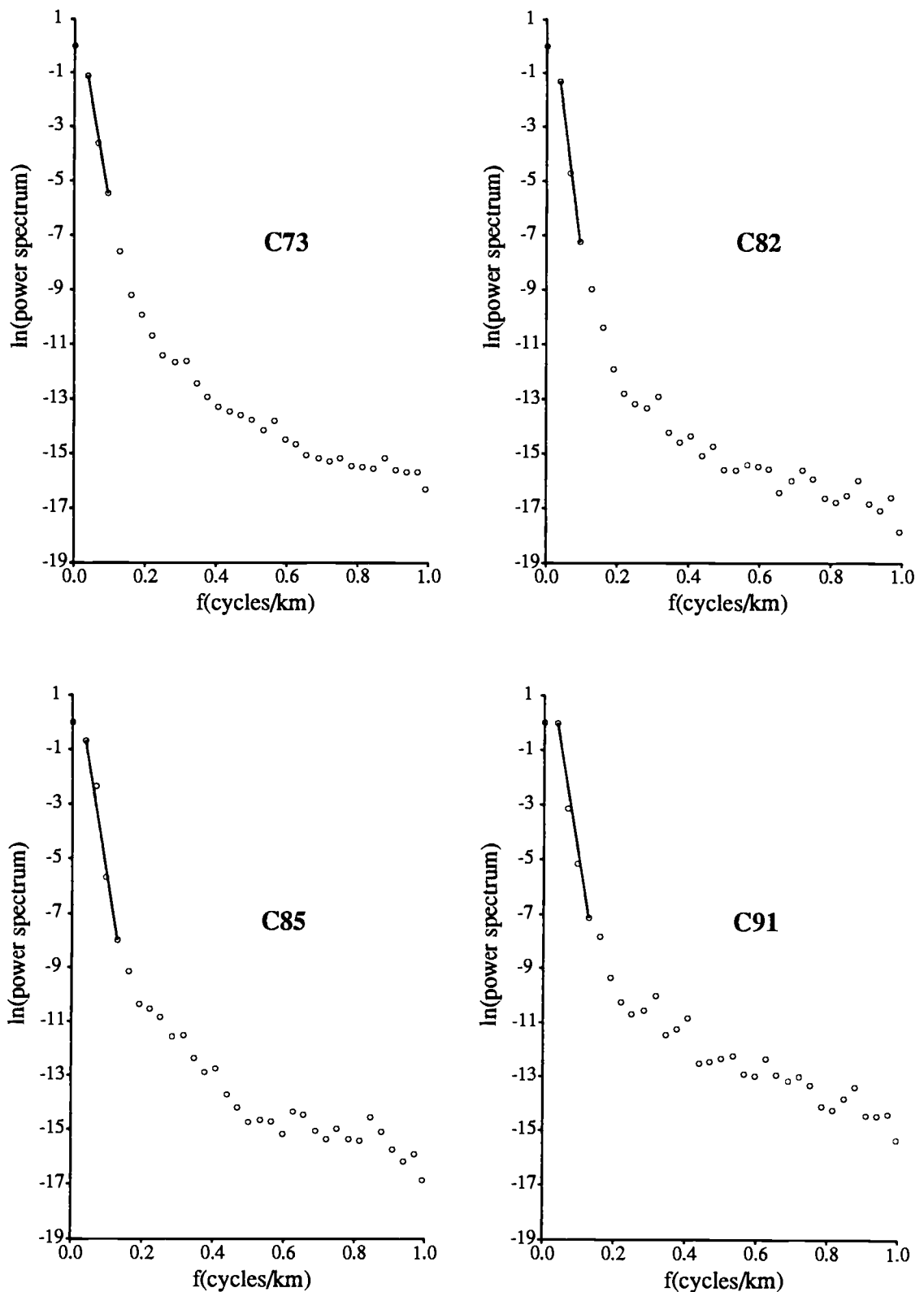


Figure B15. Maximum Entropy Radial Plots. Grids C73, C82, C85, and C91

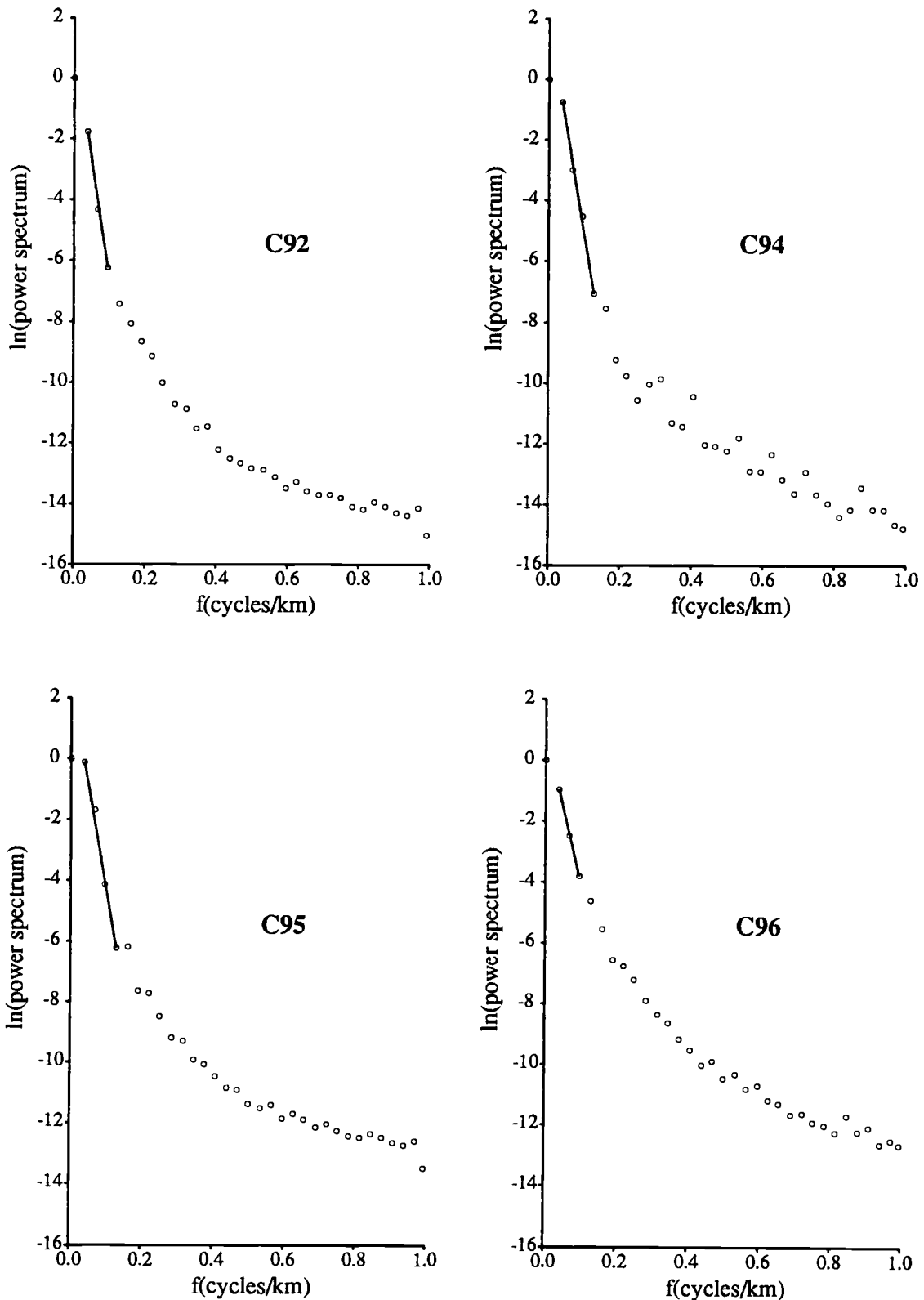


Figure B16. Maximum Entropy Radial Plots. Grids C92, C94, C95, and C96

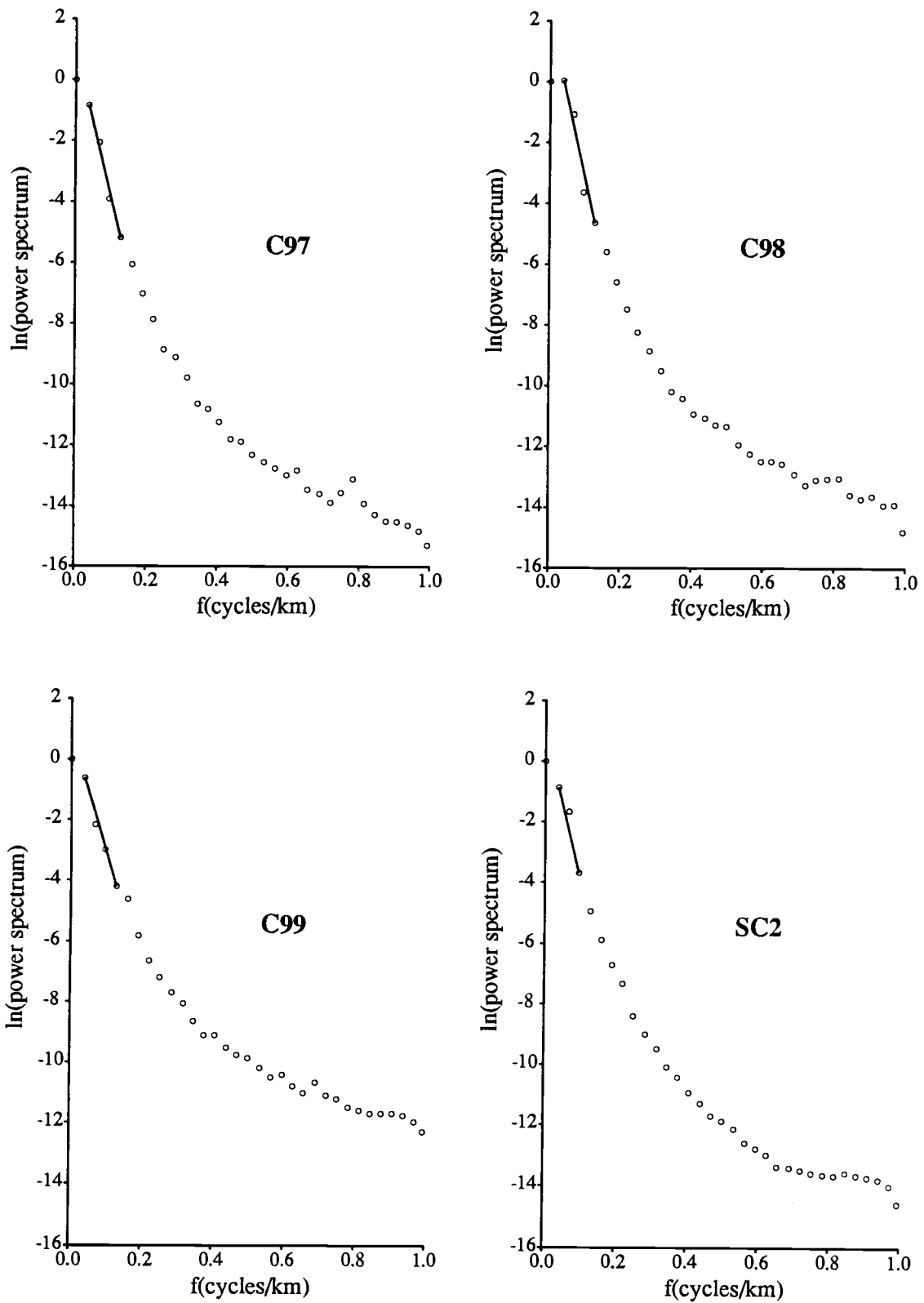


Figure B17. Maximum Entropy Radial Plots. Grids C97, C98, C99, and SC2

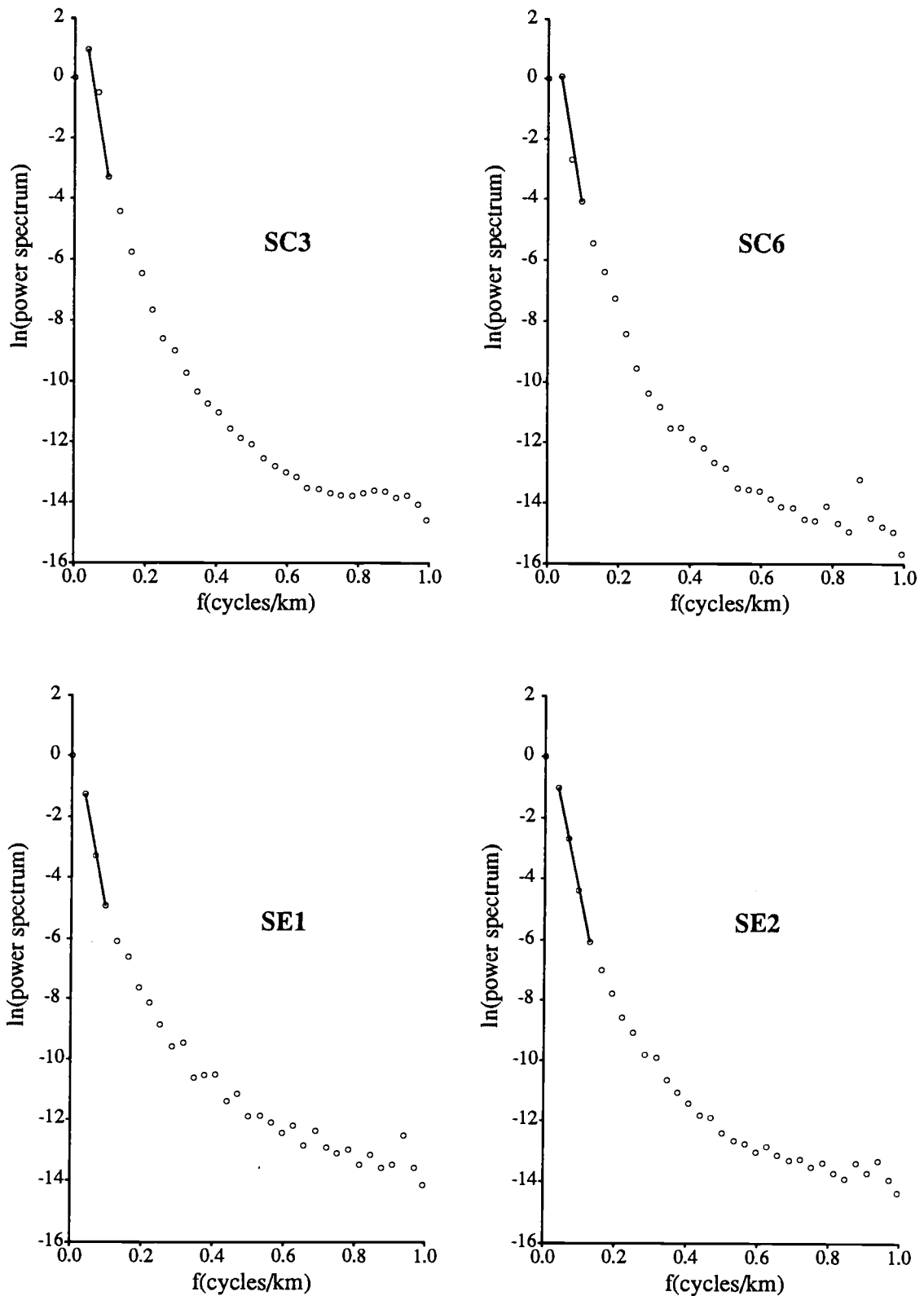


Figure B18. Maximum Entropy Radial Plots. Grids SC3, SC6, SE1, and SE2

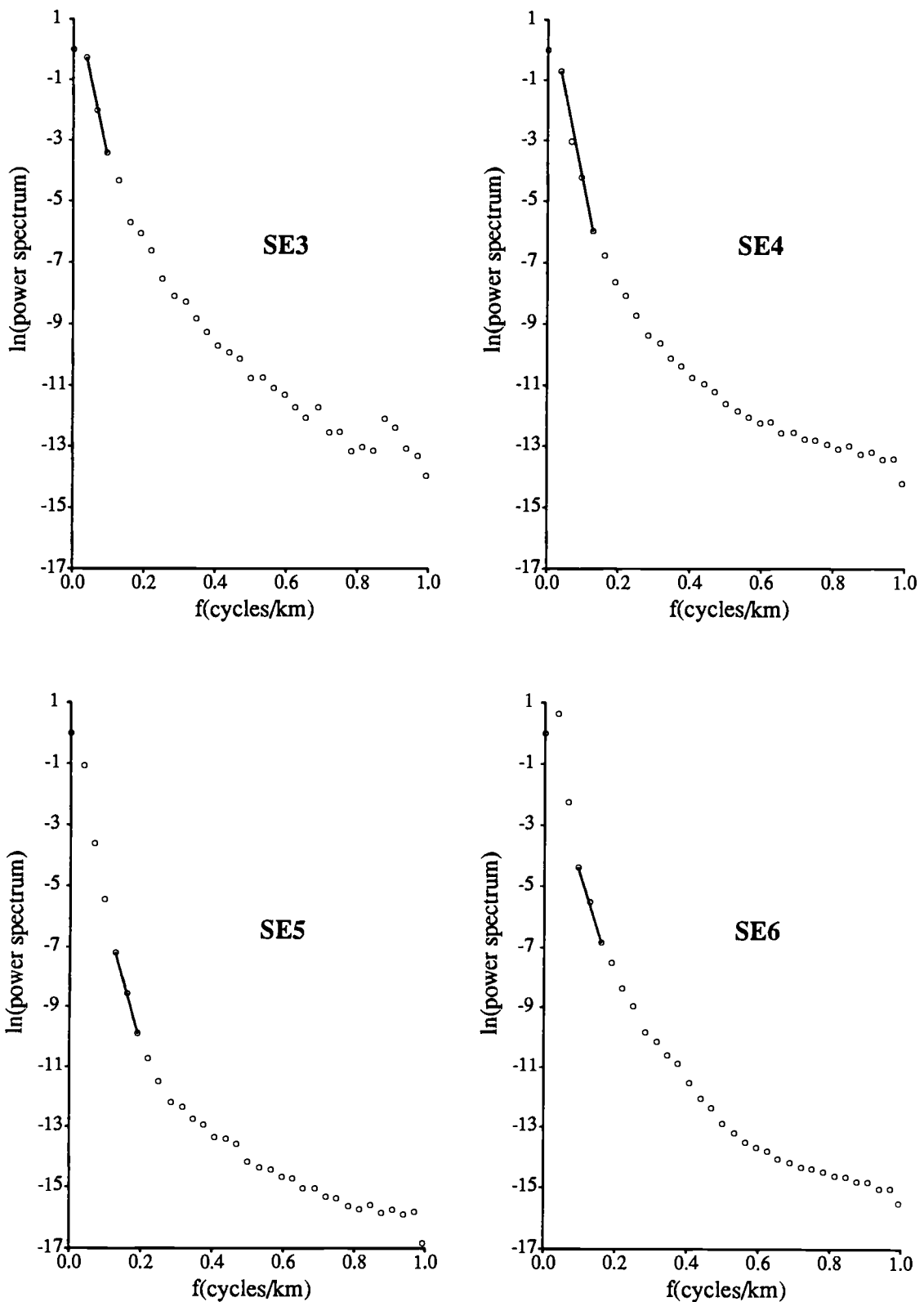


Figure B19. Maximum Entropy Radial Plots. Grids SE3, SE4, SE5, and SE6